The Dissertation Committee for Sukrith Umesh Dev
certifies that this is the approved version of the following dissertation:

Infrared Detection and Materials Characterization using Microwave Resonators

Committee:

Daniel Wasserman, Supervisor

Seth Bank

Emanuel Tutuc

Edward Yu

Jeffery Allen

Infrared Detection and Materials Characterization using Microwave Resonators

by

Sukrith Umesh Dev

DISSERTATION

Presented to the Faculty of the Graduate School of

The University of Texas at Austin

in Partial Fulfillment

of the Requirements

for the Degree of

DOCTOR OF PHILOSOPHY

THE UNIVERSITY OF TEXAS AT AUSTIN

December 2019

Acknowledgments

Even though this dissertation says "Sukrith Dev" on the front (or at least, it should), none of the work presented would have been possible without the contributions of the many people in my life who have helped me achieve my goals.

First and foremost, I thank my dear parents, Sreemathy and Umesh Dev, who have instilled in me both a passion for science, and the discipline required for engineering school. My mother's nonstop enthusiasm for math and physics spread to me from a very early age before I could tie my shoelaces (although to be fair, I still can't tie them on some days)...and then she became a Kumon instructor! *My* Kumon instructor. To all those in the Kumon program, just know that despite the hardships faced, it really is a beautiful program and was definitely worth it; to all alumni, well, we can talk after-hours! My father taught me that without values, fundamentals are meaningless; without creativity, practical thinking, discipline, and the passion to do everything to the best of our ability, we cannot achieve our goals. During the long nights in the lab, whenever I would want to go home without completing all the experiments, I would hear my father's words: "a stich in time saves nine." I can't sew a single blasted thing, but his words of wisdom greatly increased my productivity throughout grad school. Next, I thank my dear sister, Vidhya, for being an awesome sibling (despite being the second-best child) and for being the only one who always understands my strange, random references. Zvarri! I thank everyone in my extended family (my cousins, chithi, chithappa, athae, athimber, perima, peripa, mamas

and mamis, and thathas and pattis) for their constant encouragement and blessings. I especially thank my patti, Vijaya, whose nonstop love, blessings, and words of wisdom always put a smile on my face.

I thank Sri Ramani Guruji and Sri Shankerji for their eternal love, guidance and blessings.

I thank all my grade school teachers and professors at both Illinois and UT for the knowledge they have imparted.

I also thank the members of my dissertation committee, Prof. Dan Wasserman, Prof. Seth Bank, Prof. Emanuel Tutuc, Prof. Edward Yu, and Dr. Jeffery Allen, who have taken the time out of their busy schedules to read my dissertation and listen to me talk about my work.

Next, I would like to thank all my labmates in both the Wasserman group and in other groups, with whom I've shared the joys and challenges of graduate school. I would like to especially thank Lan Yu for his mentorship in the lab during my first year and Leland Nordin, my grad school comrade who has not only improved my level of thinking, but has also taught me a great deal of scientific vernacular and jargon such as: "rough-cut", "muck-muck", "schmutz", "good amongst friends", and "c'est la vie."

I thank all of the support staff at MRC for creating an environment in which we can achieve our research goals.

I acknowledge and thank all the funding agencies who have supported the work in this dissertation.

I thank all my collaborators and coauthors on papers, all of whom are named throughout the dissertation for their contributions. I would especially like to thank Drs. Jeffery and

Monica Allen for both their mentorship during my summers at Air Force Research Labs as well as the life-saving advice to not drink the tap water at the REEF!

Finally, I thank my dear advisor, Prof. Dan Wasserman, who has taught me pretty much everything I know about mid-infrared photonics and scientific thinking. I joined Prof. Wasserman's group as an undergrad in Illinois nearly six years ago and have since then been always grateful to Prof. Wasserman for his quick-thinking, endless patience, tolerance for my jokes and atrocious poetry, intolerance toward Rumplestiltskin making cameo appearances in professional talks, and above all, passion for the subject. Even though he's never seen or read Harry Potter (yeah, I know, this one is *definitely* a Hufflepuff), he has a wizard-like ability to always know *exactly* what I don't know. Finally, the most important thing I learned from Prof. Wasserman is that there is nothing in science that is difficult. Most things are, however, quite "tricky."

- Sukrith

Austin, TX

Infrared Detection and Materials Characterization using Microwave Resonators

Publication No. _____

Sukrith Umesh Dev, Ph.D.
The University of Texas at Austin, 2019

Supervisor: Daniel Wasserman

The radio frequency (RF) and microwave regions of the electromagnetic (EM) spectrum have seen incredible advances over the last few decades. RF components have become more compact, inexpensive, and accessible while still maintaining high performance. Applications such as communications or sensing that were originally intended for the military have now become commercial and used regularly by the majority of citizens. On the other hand, the mid-infrared (MIR) region of the EM spectrum, although gaining significant attention in recent years, does not have the same widespread material and device infrastructure associated with the RF. This dissertation seeks to exploit the maturity of the RF spectral range for infrared applications. Specifically, we utilize resonant microwave circuits, microwave split ring resonators (SRRs), as an effective means of mid-infrared detection and materials characterization.

The presented work is primarily divided into three research thrusts. Ultimately, because the goal of this dissertation is to employ microwave resonators to interact with

semiconductor materials, to determine the position of greatest field strength in our microwave circuits, the first technique introduced is the microwave mapping by optically induced conductance (MMOIC). In the MMOIC, a resonant microwave circuit is driven by a continuous wave (CW) RF source, while a laser simultaneously optically excites the semiconductor on which the circuit is fabricated. It is shown that the optically modulated signal is proportional to the square root of the RF power, suggesting that the response provides a measurement of relative electric field strength. It is demonstrated that when the circuit is driven on resonance, the spatial position of greatest field is located within the capacitive split-gap of the SRR. In the second presented technique, the micro-scale time-resolved microwave resonator response (μ-TRMRR), the SRR circuit is used to characterize the time-response of a micro-scale infrared pixel capacitively loaded in the split-gap. While driving the circuit on resonance, a pulsed laser excites electron-hole pairs (EHPs) in the pixel, modulating the amplitude of the transmitted carrier wave. By reading out the modulated carrier amplitude as a function of time via a Schottky diode RF detector, the minority carrier lifetime of the micro-scale material is effectively characterized. Results are compared with time-resolved photoluminescence (TRPL), and it is demonstrated that for this material system, the μ-TRMRR has a $> 10^5$ improvement in sensitivity relative to TRPL. Next, the coupled pixel-SRR architecture, dubbed as the resonant microwave photoconductor (RMPC), is evaluated as a candidate for room temperature MIR detection. A noise analysis is performed on the RMPC, and it is found that the resonator can shape and suppress Johnson noise generated from the reactively coupled pixel. When compared to a standard DC photoconductor (DCPC) utilizing similar infrared absorber material, the RMPC architecture demonstrates a factor of three improvement in the Johnson-limited spe-

cific detectivity (D*). Finally, the dissertation concludes by summarizing the results and suggesting future work in this branch of RF-photonics.

Table of Contents

Acknowledgments iv

Abstract vii

List of Figures xiv

Chapter 1. Introduction 1

1.1 RF/Microwave Photonics . . . 1

1.1.1 High-Speed Modulation of Optical Signals . . . 3

1.1.2 Dual-Comb Spectroscopy . . . 4

1.2 Applications of the Mid-Infrared . . . 5

1.2.1 Sensing . . . 5

1.2.2 Imaging & Defense . . . 6

1.2.3 Communications . . . 8

1.3 Survey of Traditional Infrared Detection Architectures . . . 9

1.3.1 Thermal Detectors . . . 9

1.3.2 Junction Devices . . . 10

1.3.3 The DC Photoconductor . . . 11

1.3.4 Reactively Coupled Detectors: An Introduction . . . 12

1.4 RF/Microwave Transmission Lines . . . 14

1.4.1 Telegrapher's Equations and the Terminated TLine . . . 14

1.4.2 Common On-Chip Transmission Lines . . . 18

Chapter 2. Modeling and Experimental Setups 20

2.1 Modeling Methods and Example Calculations . . . 20

2.1.1 Mismatched Transmission Lines: A General Case . . . 21

2.1.2 Finite Element Method . . . 25

2.1.3 Time Domain: Backwards Euler Method . . . 27

2.2 Microwave Characterization . . . 30
2.2.1 Scattering Parameters and 2-Port Z-Matrix Conversion . . . 30
2.2.2 Vector Network Analyzer and Calibration Techniques . . . 33
2.3 Optical Characterization . . . 36
2.3.1 Fourier Transform Infrared Spectroscopy . . . 37
2.3.2 Step Scan and Mid-Infrared Photoluminescence . . . 42
2.3.3 Time-Resolved Photoluminescence . . . 47

Chapter 3. Microwave Mapping by Optically Induced Conductance (MMOIC) 49
3.1 Traditional Field Mapping Techniques . . . 50
3.2 Overview of the MMOIC Technique . . . 54
3.2.1 Setup and Operating Principles . . . 54
3.2.2 Fabrication of Split Ring Resonators . . . 56
3.3 Modeling . . . 58
3.3.1 HFSS Simulations . . . 59
3.3.2 Lumped Element Modeling . . . 60
3.4 Results and Experimental Data . . . 64
3.5 Suggested Future Work and Summary of Technique . . . 69

Chapter 4. The Micro-Scale Time-Resolved Microwave Resonator Response (μ-TRMRR) Technique 72
4.1 Background . . . 73
4.1.1 Common Lifetime Measurement Techniques . . . 74
4.2 Optical Characterization of InAsSb Pixels . . . 77
4.2.1 Fabrication of InAsSb Pixels . . . 78
4.2.2 Photoluminescence and Time-Resolved Photoluminescence . . . 78
4.3 Single Pixel Transfer into a Microwave Resonator . . . 82
4.3.1 SRR Fabrication and Dimensions . . . 82
4.3.2 Pixel Transfer General Procedure . . . 83
4.3.3 hBN and Lumped Element Modeling . . . 85
4.4 Overview of μ-TRMRR Technique . . . 88
4.4.1 Schematic and Working Principles . . . 88
4.4.2 Linearity of Response . . . 89

4.4.3 Temperature Dependent Minority Carrier Lifetimes of a Single InAsSb Pixel . . . 93
4.5 Comparison of Lifetime Techniques . . . 95
4.6 Application of Technique to Other Material Systems . . . 97
4.6.1 Monolayer WS_2 . . . 97
4.6.2 Pushing to High-Speed Materials . . . 99
4.7 Summary of Technique . . . 101

Chapter 5. Resonant Microwave Photoconductive Detectors 103
5.1 Background . . . 104
5.1.1 Motivation for Contact-Free Detector Architectures . . . 104
5.1.2 Microwave Resonators: From Sensors to Detectors Overview . . . 107
5.1.3 Overview of Direct Current Photoconductors and Resonant Microwave Photoconductive Architectures . . . 108
5.1.4 Specific Detectivity . . . 111
5.2 Comparison of Responsivities . . . 114
5.2.1 Bias Dependent Setup . . . 114
5.2.2 Spectral Response Setup . . . 121
5.3 Noise . . . 122
5.3.1 Theory and the Johnson Limit . . . 123
5.3.2 Time Domain Modeling of Noise Sources Within Resonators . . . 126
5.3.3 Johnson Noise of the Coupled Pixel-Resonator System . . . 128
5.3.4 Noise Measurement Setup . . . 133
5.4 Discussion of Architecture Performance . . . 135

Chapter 6. Conclusion 138
6.1 Future Work . . . 138
6.1.1 Loaded PCB Resonators . . . 138
6.1.2 Photodoped ENZ Ultra-Thin Microstrip Waveguides . . . 139
6.2 Summary . . . 144

Appendices 147

Appendix A. An Experimentalist's Handbook **148**
A.1 Photoluminescence 148
A.2 Time-Resolved Photoluminescence 150
A.3 Responsivity Measurements 153

Appendix B. Fabrication Recipe Notes **154**
B.1 SRRs on Semi-Insulating Gallium Arsenide (SI GaAs) 154
B.2 SRRs on 99.6 % Aluminum Oxide 155
B.3 PCB Resonators 155
B.4 Epsilon-Near-Zero (ENZ) Ultra-Thin Microstrips 156

Appendix C. List of Publications and Conference Talks **158**
C.1 Journal Publications 158
C.2 Conference Presentations and Publications 159

Bibliography **161**

List of Figures

1.1 Electromagnetic spectrum, with the infrared (IR) split into the: near-infrared (NIR), mid-infrared (MIR), and far-infrared (FIR). The MIR is further split into useful bands: the short-wave infrared (SWIR), mid-wave infrared (MWIR), and long-wave infrared (LWIR). The microwave bands are split into the ultra high frequency (UHF), super high frequency (SHF), and extremely high frequency (EHF), with the SHF classified even further. The MWIR and Ku band are circled as they are used in this dissertation . . . 2

1.2 (a) Diagram of a Mach-Zehnder EO modulator; (b) commercial EO modulator (ThorLabs LN82S-FC) . . . 4

1.3 Diagram of dual-comb spectroscopy basic working principles. Two combs with slightly different frequency spacing are interfered on a detector; the difference frequencies between the combs allows for optical spectral features to be mapped to the RF. Taken and adapted from Ian Coddington's dual-comb spectroscopy review [1] . . . 5

1.4 Infrared absorption spectra for many common molecules; taken and adapted from [2] . . . 6

1.5 Infrared thermography (IRT) applied toward material damage diagnostics: (a) damage in the material can manifest as thermal cracks which can be observed using IRT; (b) setup for active IRT which uses an external IR source to illuminate the material and an IR detector/camera to observe externally induced changes in the thermal signature. Taken and adapted from [3] . . . 7

1.6 (a) Atmospheric transparency across the infrared; (b) schematic of a proposed communication system in which both RF and optical links are utilized. Images taken and adapted from [4] and [5], respectively . . . 8

1.7 (a) Cross-sectional view of a standard bolometer; (b) basic detection circuit containing the bolometer; taken and adapted from [6] . . . 10

1.8 Representative band diagram of (a) pn junction based device and (b) nBn device under operation. Images taken and adapted from [6] and [7], respectively . . . 10

1.9 Schematic of a basic photoconductive circuit . . . 12

1.10 Generalized block diagram of a microwave-based infrared detector utilizing reactively coupled absorbers . . . 13

1.11 Lumped element model for a section of transmission line of length Δz. Image taken and adapted from Pozar's textbook [8] 15

1.12 Schematic of (a) microstrip waveguide with made with a dielectric constant, ϵ_d, loss tangent $tan\delta$, dielectric thickness, H, and strip width, W; (b) grounded coplanar waveguide with dielectric constant, ϵ_d, loss tangent $tan\delta$, dielectric thickness, H, strip width, W, and slot width, S 18

2.1 Overhead view of of an example port. The gold regions represent metal (typically gold in this dissertation) and the gray represents an insulator. A ground-signal-ground (GSG) probe makes contact to the coplanar probe pad (red dashed lines), which has a length, effective permittivity, and characteristic impedance. This pad can then lead into a microstrip, which has its own set of parameters describing propagation 21

2.2 Transmission line model representation of Figure 2.1 with a source and source impedance, Z_S, and load termination of Z_L. The coplanar pad (red) and microstrip transmission line (blue) each have their own lengths, propagation constants, and characteristic impedances. Input impedances and reflection coefficients are defined at each node or potential mismatch. . 22

2.3 First transmission line reduction. Once Z_{in1} is computed, the problem in Figure 2.2 can be reduced to simply the coplanar pad line terminated by Z_{in1}, which now serves as the effective load 23

2.4 Final circuit reduction. Once Z_{in2} is computed, Figure 2.3 can be reduced to this diagram. The voltage dropped over Z_{in2}, which is equivalent to $V(d_{Pad})$, is obtained through simple voltage division 24

2.5 (a) Sample arbitrary function, f, as a function of x. The function is split at the blue lines into n pieces, with a denser set of pieces in regions of rapidly changing function or large gradients; (b) example of a mesh pattern in a simple microstrip FEM simulation 27

2.6 Example of a linear companion model for a capacitor; taken and adapted from [9] 29

2.7 N-port network diagram. Each port has a signal, in this case a voltage, which enters (labeled with a "+" superscript and exits (labeled with a "-" superscript) the port 31

2.8 Diagram for the methodology of vector network analysis performed on a device under test (DUT) 33

2.9 S_{21} spectra of both an uncalibrated (dark gray) and calibrated (red) matched coplanar waveguide. The calibrated curve accounts for the cables and probes and produces an ideal S_{21} across all frequencies 34

2.10 Schematic of the CS-5 calibration (left) substrate sold by GGB Industries for probe calibration; the calibration standards used are circled and expanded for clarity on the right 35

2.11 Sample diagram of a commercial monochromator from Horiba 37
2.12 Schematic of an example FTIR spectrometer. This particular configuration shows an experimental setup for transmission through a sample; however, other setups maintain similar interferometry principles. To characterize a source, an entrance port couples external light, instead of the internal globar, into the interferometer. Conversely, for typical detector characterization, broadband light from the globar is sent out of the FTIR from an exit port and is incident upon the detector to be characterized. The signal from the detector is then measured as a function of mirror position to obtain the interferogram. 39
2.13 Interferograms (IFGs) of both (a) coherent and (b) incoherent sources. After applying a Fourier transform, the IFGs give the spectra shown for the (c) coherent and (d) incoherent sources 41
2.14 Electronic spectrum of detector output in a modulation experiment. The red line denotes the signal at the modulation frequency, f_{mod}, and the blue line denotes the output noise spectra of the detector, with 1/f corner frequency, $f_{1/f}$, and the cutoff frequency, f_{cut}, labeled. The green dashed line represents an ideal filter which can isolate the signal from the noise . . 43
2.15 Schematic of the temperature dependent photoluminescence (PL) setup in the Wasserman lab built for the work in this dissertation. Both the regular PL (normal collection) and 45 degree/edge emission setups (activated with flip mirror) are shown 46
2.16 Schematic of the temperature dependent time-resolved photoluminescence (TRPL) setup in the Wasserman lab built for the work in this dissertation . . 48

3.1 Schematic of the microwave tip based on scanning tunneling microscopy (STM), used for mapping evanescent microwave fields with a high spatial resolution, typically on the order of microns. Taken and adapted from [10] . 51
3.2 Schematic of the electro-optic (EO) field mapping technique utilizing an external crystal. Taken and adapted from [11] 53
3.3 Overview of the microwave mapping by optically induced conductance (MMOIC) technique; (a) schematic and operation; (b) overhead view of the device under test (DUT) consisting of split-ring resonators (SRRs) coupled to a microstrip; (c) beam spot size measurement; (d) S_{21} of both a dark and illuminated SRR; (e) schematic of beam spot size measurement method; partially adapted from [12] 55
3.4 Fabrication process for split-ring resonator circuits, with further details/specifics provided in Appendix B. Note that the coplanar "horseshoe" probe contact pad seen in Figure 3.3(b) is not shown in the diagram of step 4) for simplicity 57
3.5 Overhead view of the HFSS simulation drawing 58

3.6 Lumped element model for our split-ring resonator (SRR) capacitively coupled to a microstrip busline 60
3.7 First circuit reduction; the terminated mismatched lines from Figure 3.6 on the right hand side is reduced to Z_{in1} 61
3.8 Second circuit reduction; the impedance of the SRR is computed in parallel with the Z_{in1} from Figure 3.7 63
3.9 Comparison of S_{21} spectra taken with a VNA (red), modeled analytically (Mathematica) via lumped elements and transmission lines (blue), and simulated using HFSS (green) 65
3.10 HFSS simulated (a, b) normalized electric fields and experimental (c, d) MMOIC contour plots for a square SRR resonator driven (b, d) off and (a, c) on resonance. Simulations performed at (a) f_{on} = 15.24 GHz and (b) f_{off} = 10 GHz. Experimental data taken at (c) f_{on} = 15.2 GHz and (d) f_{off} = 10 GHz 66
3.11 Modeled (solid) and experimental (scatter) change in transmitted power as a function of frequency for light incident on busline (green), coupling gap (blue), and SRR gap (red); inset demonstrates linearity of our measured signal with respect to $\sqrt{RFPower}$, suggesting we are measuring a relative electric field 68
3.12 Experimental MMOIC plots for different resonator structures (a) 20 μm SRR gap (b) 70 μm SRR gap and (c) circular SRR with 40 μm gap. Top row shows on-resonance scans ((a) f_{on} = 15.76 GHz, (b) f_{on} = 15.4 GHz,(c) f_{on} = 17.9 GHz) while bottom row shows off-resonance data (f_{off} = 10 GHz) 69

4.1 Schematic of a basic photoconductive decay (PCD) setup 75
4.2 Two popular contact-free carrier lifetime measurement techniques: (a) time-resolved photoluminescence (TRPL) as described in chapter two; (b) example of a time-resolved microwave reflectance (TMR) setup 76
4.3 Fabrication process for InAsSb pixels made from bulk material grown on top of a sacrificial etch release 79
4.4 Photoluminescence spectra of the (a) bulk, as-grown InAsSb structure in Figure 4.3 step 1) and (b) fabricated cluster of pixels shown in Figure 4.3 step 4); time-resolved photoluminescence of (c) bulk, as-grown structure and (d) pixel cluster 80
4.5 Dimensions of the fabricated SRR used in this chapter; the microstrip busline length is 2 mm, SRR side length 1 mm, busline width 50 μm, SRR to busline coupling gap 30 μm, and SRR split-gap 10 μm 83
4.6 Overview of pixel transfer technique 84
4.7 Effects of loading the pixel into the resonator; S_{21} spectra of the bare, unloaded resonator (black), pixel loaded resonator (red), and pixel loaded on top of a thin hBN layer (blue) 85

4.8 (a) Measured (solid lines) and modeled (dashed lines) $|S_{21}|$ parameter for the bare SRR (black), loaded SRR (red), and illuminated SRR (blue); (b) transmission line model used in (a) 86

4.9 Schematic of of the μ-TRMRR technique for measuring carrier lifetimes in micro-scale volumes. A micrograph of the pixel and hBN transfered to the split-gap of the resonator is shown in the top right, with a scale bar of 20 μm 89

4.10 Linearity of the presented technique. (a) Measured ΔS_{21} (the change in the S_{21} parameter when light is incident upon the pixel) for varying CW laser excitation at room temperature, (b) modeled ΔS_{21} as a function of pixel conductance, and (c) measured room temperature μ-TRMRR signal as a function of energy incident upon the pixel. (d) $|\Delta S_{21}|$ on resonance from CW response shown in (a), (red squares), and peak $|\mu$-TRMRR| signal shown in (c) (red circles) as a function of excess carrier concentration and modeled $|\Delta S_{21}|$ (black, solid) as a function of conductance, from (b) 90

4.11 Transient decay curves. (a) Temperature-dependent μ-TRMRR signal from InAsSb pixel using 35.5 pJ pulse energy on pixel and with 2,000 averages on oscilloscope. Extracted lifetimes are shown above each curve. (b) time-resolved photoluminescence (TRPL) response of pixel array with 68 nJ laser pulse energy (equivalent to 16.6 nJ incident on pixels) and (c) μ-TRMRR data for a single pixel with 68 pJ total laser pulse energy (equivalent to 35.5 fJ incident on pixel). Both experiments in (b) and (c) are performed at 300 K, with 2,000 averages on the oscilloscope 94

4.12 Comparison of lifetime measurement techniques. Extracted carrier lifetimes as a function of temperature for time-resolved microwave reflectance (TMR) on as-grown InAsSb (orange), time-resolved photoluminescence (TRPL) on as-grown InAsSb using InSb (cyan) and mercury cadmium telluride (MCT) (light blue) detectors, TRPL from pixel array using MCT detector (blue) and single-pixel μ-TRMRR (red) techniques. TRPL (InSb), TMR, and μ-TRMRR agree well, but as shown, when using a less sensitive detector (such as MCT), the TRPL signal falls beneath the noise floor before the low-injection condition is satisfied, preventing an accurate lifetime extraction 95

4.13 μ-TRMRR technique performed on monolayer WS_2: (a) temperature dependence performed using an injected carrier concentration of approximately $8 \times 10^{12} cm^{-2}$; power dependence performed at both 11 K (b) and 300 K (c) 98

4.14 (a) An optical modulation (red square wave) rides on top of the carrier (blue sinusoid) and enters a Schottky diode, which "de-mixes" and produces the modulation as the intermediate frequency (IF); (b) the mixed optical modulation and carrier go straight to an oscilloscope without a Schottky diode; note that the oscilloscope would require a bandwidth greater than $f_{carrier} + f_{mod}$ instead of needing to be simply greater than f_{mod}, which is the case in (a) 100

4.15 μ-TRMRR response of a high-speed indium antimonide (InSb) pixel without the use of a Schottky diode; note that the time resolution is much better than in 4.11(c), with a rise time significantly less than a nanosecond 101

5.1 Comparison of signal to noise ratio (SNR) between two different area semiconductor absorbers; (a) shows a square absorber of length l, and (b) shows that absorber of length $l/10$ can still collect the same incident radiation as (a) with the help of focusing, despite having a significantly smaller area . . 105

5.2 Work done by Carlo Sirtori's group demonstrating the increase in detector operating temperature by reducing thermal fluctuations via miniaturization of active area; figure taken and adapted from their published work in [13] . 106

5.3 (a) Coupling of photoconductive absorber to a transmission line; (b) reflection cavity-based photoconductive detector. Figures taken and adapted from [14] 108

5.4 (a) DC photoconductor and (b) resonant microwave photoconductor; (i) detection circuit diagrams, (ii) micrograph of the overall device with (iii) an expanded view; (iv) dark and illuminated (100 μW of power at λ = 3.39 μm) current-voltage (DC photoconductor) and $|S_{21}|$ curve (resonant microwave photoconductor) plots. 109

5.5 Spectral specific detectivities (D*) of several commonly used detectors. Taken and adapted from [4] 111

5.6 Example noise spectra of (a) white noise and (b) frequency dependent spectra 113

5.7 (a) Diagram of the responsivity setup employed in this chapter; (b) shows the method of beam spot calculation 115

5.8 Magnitude of RF transmission (S_{21}) for the cable and probe arms (black curve) and cables only (red curve). The difference in dB yields the total loss in both probe arms 119

5.9 Bias dependent responsivity obtained at $\lambda = 3.6\mu$m 120

5.10 Spectral response setup; light from the spectrometer is chopped and redirected into the probe station. The output from the detector is sent to a lock-in amplifier (LIA) referencing the chopper modulation. The output is then sent back to the FTIR for digitization 122

5.11 Noise sources intrinsic to photoconductors; (a) shows 1/f noise (green), generation-recombination (GR) noise (blue), and Johnson noise (red); (b) scenario in which the instrument's bandwidth exceeds the detector bandwidth, resulting in a predominantly Johnson-limited case 124

5.12 (a) Circuit schematic for Johnson noise (modeled as a Thevenin white noise source placed in series with the detector). (b) Output voltage spectra for source voltage amplitudes of 0.1 V (red), 1 V (green) and 10V (blue) given a fixed thermal noise spectrum (black). (c) Circuit schematic for G-R noise [modeled as a white noise function (r_n) added to pixel resistance (R)]. (d) Voltage output spectra plotted for fixed amplitude r_n and source amplitudes of 0.1 V (red), 1 V (green) and 10V (blue), as well as the voltage spectrum from the source itself. In both models the circuits are driven on resonance, with the spectra normalized to the resonant frequency, f_0 127

5.13 Effective input impedance of the circuit; blue dashed lines represent the T-model used to model a symmetric, reciprocal two-port network, and the red dashed lines refer to the terminating load, Z_L (which we assume to be 50 Ω representative of the Schottky diode impedance). With the right side terminated, the effective input impedance, Z_{in}, can be computed 129

5.14 Johnson noise of bare SRR (black curve) and pixel-loaded SRR (blue curve) computed using Equation 5.13 and DC pixel (red dashed lines) using 4kTR, where R = 300 Ω from Figure 5.4(a-iv) 130

5.15 Bias dependent Johnson noise (dashed lines) and D* at $\lambda \approx 3.6\mu m$ (solid lines) for both the RMPC (blue) and DCPC (red) 133

5.16 Schematic of the noise measurement setup; (a) output of the detector enters a low noise preamplifier (LNP) which is then sent to the noise sweeper tool. To subtract the noise from the LNP, (b) a noise spectrum is taken with the input of the LNP shorted 134

5.17 Noise measurements with approximately 250 mV bias performed on: the RMPC system (blue curve), RF source and Schottky diode only (black curve), DCPC system (red curve), and DCPC system driven with a battery (gray cure) 135

5.18 Room temperature Johnson-limited spectral D* for both DCPC (red curve) and RMPC (blue curve) detector architectures at a 100 mV bias; the room temperature photoluminescence is also plotted (black curve) for reference . 136

6.1 Proposed PCB resonator platform used for contact-free characterization and detection using larger-area patterns of active material 139

6.2 (a) Diagram of simulated microstrip waveguide with an ultra-thin (2 μm thick) dielectric layer; (b) simulated S_{21} parameter plotted with different permittivities 140

6.3 (a) Cross-sectional diagram of the layers in the simulated structure; (b) cross-sectionnal view of the simulated electric field magnitude 141

6.4 Fabrication steps for structure given in Figure 6.2(a). Steps within the blue dashed lines have been completed thus far 144

Chapter 1

Introduction

This chapter aims to provide a motivation for studying and developing both the mid-infrared (MIR) region of the electromagnetic spectrum as well as the field of radio frequency (RF)/microwave (used interchangeably throughout this dissertation) photonics. The section begins with a discussion of two popular RF-photonic applications: high speed (GHz) modulation of optical signals and dual-comb spectroscopy. However, these fields have typically matured at shorter wavelengths ($< 2\ \mu m$), so the next subsection describes some growing applications in the MIR to motivate further study in this region. To realize most of these applications, high-performance, inexpensive detector systems are necessary; thus, a very brief survey on common detector systems is provided, and the concept of reactively coupling semiconductors to RF structures is introduced. Since transmission lines are fundamental to RF structures and the work presented, the chapter concludes by providing a background on transmission line theory and introduces some common on-chip microwave transmission lines employed in this dissertation.

1.1 RF/Microwave Photonics

The field of RF-Photonics has seen tremendous growth in recent years with a wide range of applications now used everyday by civilians outside science and technology fields.

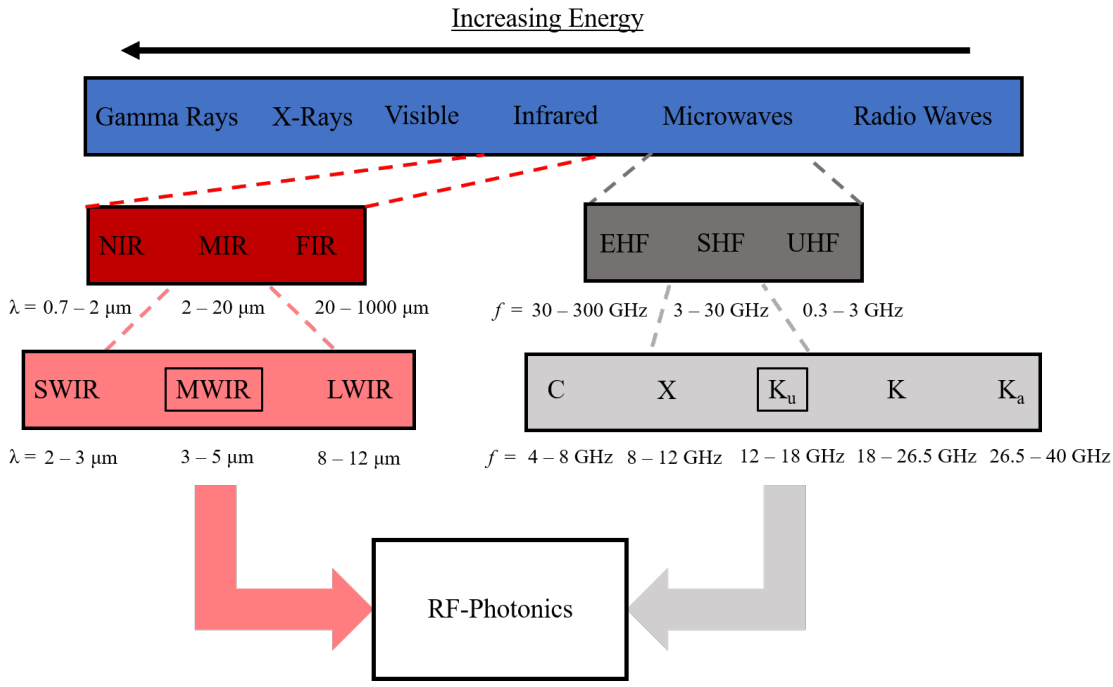

Figure 1.1: Electromagnetic spectrum, with the infrared (IR) split into the: near-infrared (NIR), mid-infrared (MIR), and far-infrared (FIR). The MIR is further split into useful bands: the short-wave infrared (SWIR), mid-wave infrared (MWIR), and long-wave infrared (LWIR). The microwave bands are split into the ultra high frequency (UHF), super high frequency (SHF), and extremely high frequency (EHF), with the SHF classified even further. The MWIR and Ku band are circled as they are used in this dissertation

While technically, there are many advantages to incorporating these two separate regions of the electromagnetic (EM) spectrum (as shown in Figure 1.1), the practical advantages can be attributed to the maturity of RF technology. Over the past few decades, several practical barriers to entry such as cost and compactness of RF devices have been reduced by the free market and the vast growth of the field. Hence, RF components are attractive practical additions to enhance and innovate optical technologies. In most cases, an RF signal modulates an optical component, as is the case for high-speed optical communications.

Conversely, there has been a growing interest in the opposite scheme in which an optical signal modulates an RF component; the methodologies and devices in this dissertation follow the latter approach.

1.1.1 High-Speed Modulation of Optical Signals

High speed fiber-to-the-home using fiber optic communication is now commercially available to civilians in many major cities such as Austin, TX. Any form of communication requires a source, guiding medium, method of modulation, and receiver. As a means of high speed modulation, a Mach-Zehnder electro-optic (EO) modulator, as shown in Figure 1.2, is often used. In the modulator, an optical signal that enters a waveguide splits into two arms. In one of the arms, the signal experiences a phase shift due to an electro-optic (EO) effect [15]; in the EO effect, an applied bias effectively modulates the refractive index, which in turn modulates the phase accumulated by an optical signal traveling through that arm of the modulator. For a given crystal and length, the voltage needed to shift the phase by π is typically referred to as V_π. This half of the optical signal recombines with the other half (which has not been phase shifted) and destructively interferes. Therefore, by oscillating the voltage applied to the EO crystal, the optical signal can be rapidly turned on and off, often in the GHz range. In this situation, an RF signal applied to the EO crystal in the modulator is used to effectively modulate the optical signal. Hence, high-speed EO modulators fall under the category of RF-photonic devices, as they simultaneously interact with RF and optical signals. The field of fiber optic communication has seen extensive academic research and commercial development, with a wealth of literature and books [16] on the subject readily available for further reading.

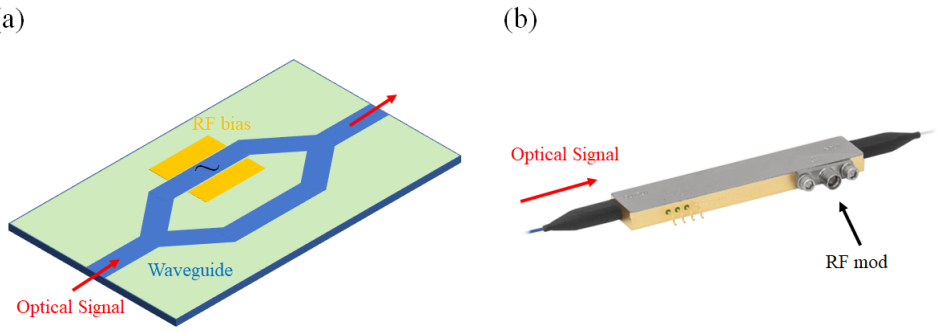

Figure 1.2: (a) Diagram of a Mach-Zehnder EO modulator; (b) commercial EO modulator (ThorLabs LN82S-FC)

1.1.2 Dual-Comb Spectroscopy

Dual-comb spectroscopy (DCS) is a very rapidly emerging platform in the infrared which also incorporates RF components. The overall schematic of the methodology is given in Figure 1.3. Typically, two different optical frequency comb sources (which could consist of mode-locked lasers, or the recently popular Kerr soliton combs [17][18]) are required. One of the combs passes through the sample and is absorbed; hence, this comb carries the absorption spectral information of the sample. The comb is then interfered with a second comb, which has a slightly different comb spacing. Because of this, difference beatnotes show up on the electronic spectrum of the detector; the frequency of these beatnotes are related to the difference in comb spacing between the two combs and is typically on the order of RF frequencies. Hence, instead of needing an expensive and potentially cumbersome optical spectrum analyzer (OSA), the optical absorption phenomena can be analyzed at RF frequencies using a more accessible RF spectrum analyzer. A more thorough discourse on DCS can be found in Ian Coddington's review [1].

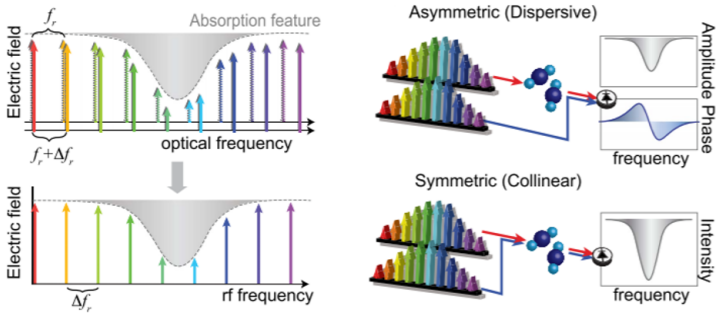

Figure 1.3: Diagram of dual-comb spectroscopy basic working principles. Two combs with slightly different frequency spacing are interfered on a detector; the difference frequencies between the combs allows for optical spectral features to be mapped to the RF. Taken and adapted from Ian Coddington's dual-comb spectroscopy review [1]

1.2 Applications of the Mid-Infrared

In Section 1.1, two prominent applications which incorporate RF components into optics were described. While there are clear technical advantages to combining these two spectral regions (and fewer practical drawbacks due to the modern advancement of RF components), the applications described above have typically matured at shorter wavelengths ($< 2\ \mu m$), although there has been a significant push to demonstrate the effectiveness of these concepts further into the MIR [19][20][21][22]. In this section, a clear motivation is provided for studying and further developing the mid-infrared (MIR), defined here to be between 2 - 20 μm.

1.2.1 Sensing

Figure 1.4 shows the absorption spectra of a representative few molecules of the many that strongly absorb MIR light due to vibrational resonances, which makes this spectral range well-suited for molecular sensing applications such as environmental monitoring

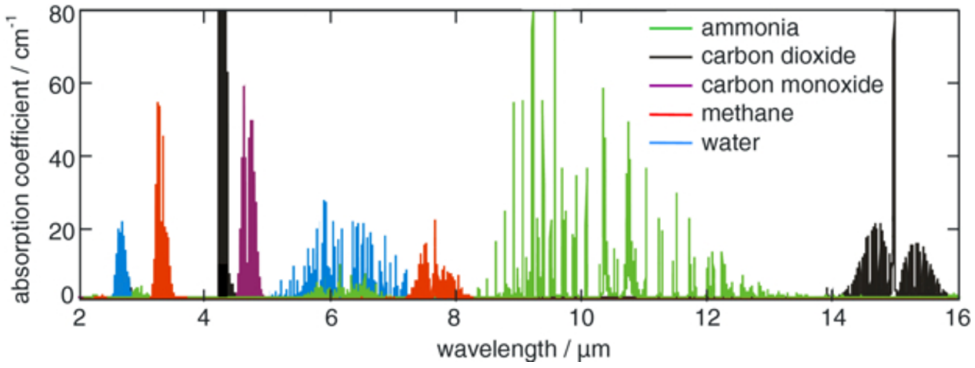

Figure 1.4: Infrared absorption spectra for many common molecules; taken and adapted from [2]

[23], breath analysis [24], or threat detection [25]. While there are several methods that can be used for sensing, typically, three components are required: a source, sample containing molecules or gas, and a detector. Although Fourier-transform infrared (FTIR) spectroscopy (described in detail in Chapter 2 Subsection 2.3.1) is commonly employed in laboratory settings, the FTIR spectrometers are significantly bulky and can be quite costly. Thus, methods which avoid the use of an interferometer are attractive for several practical applications. These alternative methods typically use a tunable source, such as a quantum cascade laser (QCL) [26], or employ frequency comb sources as in the case of dual-comb spectroscopy (mentioned earlier in Subsection 1.1.2). Because of increased compactness due to the use of semiconductor sources, and thus practical utility, these methods have already found applications, such as the use of tunable QCLs for mycotoxin detection [27].

1.2.2 Imaging & Defense

Thermal signatures of both hot objects and people typically fall within the MIR spectrum, which makes the region well-suited for both defense and imaging applications.

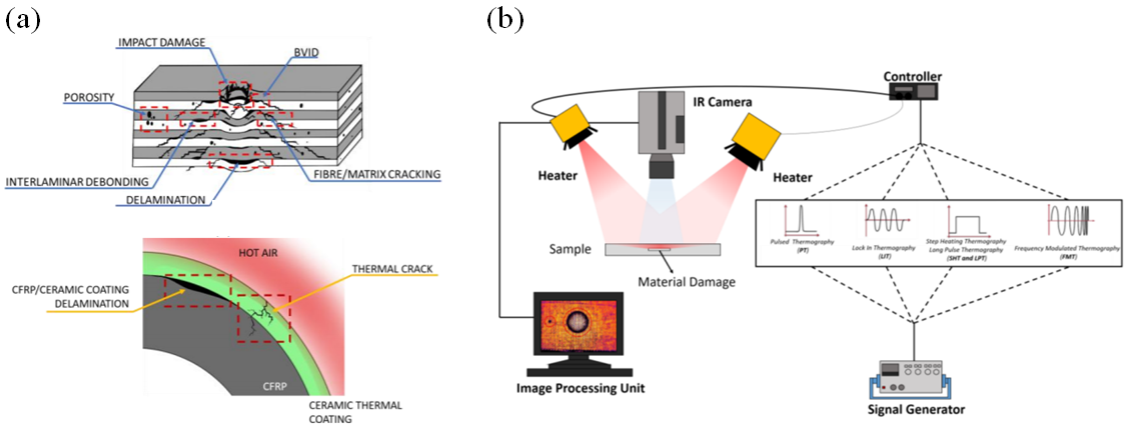

Figure 1.5: Infrared thermography (IRT) applied toward material damage diagnostics: (a) damage in the material can manifest as thermal cracks which can be observed using IRT; (b) setup for active IRT which uses an external IR source to illuminate the material and an IR detector/camera to observe externally induced changes in the thermal signature. Taken and adapted from [3]

Night vision [28][29][30] and the ability to track heat signatures of both aircraft and people are of significance for security and and national defense applications. Furthermore, imaging of aircraft, structures, and materials can also be used for diagnostic purposes. For example, in the aerospace industry [3], civil engineering applications [31], and material science [32][33], the field of infrared thermography (IRT) can be applied toward damage assessment of aircraft and materials, as seen in Figure 1.5. In active IRT, an external IR source illuminates the material or object under test, and the externally induced changes can be imaged and extracted from any background to aid in the diagnosis of material damage. For further reading, Michele Meo's group at the University of Bath has published a recent review article on the topic of active IRT [3].

1.2.3 Communications

In Subsection 1.1.1, the subject of fiber optic communications operating in the NIR (nominally 1.55 μm) was briefly discussed. While the NIR is well-suited for high-speed communications using fibers, the MIR has garnered significant interest in free-space optical (FSO) communication links. In Figure 1.6(a), the transparency window of the atmosphere across the infrared spectra is plotted [4]. It's clear that although the NIR does possess reasonable transparency (approximately 70%), the mid-wave IR band (defined in Section 1.1 to be between 3-5 μm in wavelength), has at least 15% more atmospheric transparency. Furthermore, scattering and the effects of bad weather conditions such as fog are reduced as the wavelength is increased, thus motivating the use of MIR FSO communication links [34].

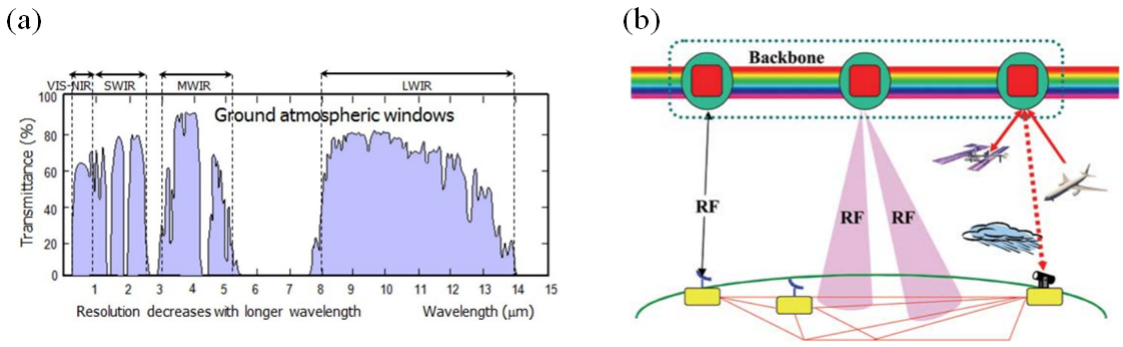

Figure 1.6: (a) Atmospheric transparency across the infrared; (b) schematic of a proposed communication system in which both RF and optical links are utilized. Images taken and adapted from [4] and [5], respectively

With the development of MIR sources and detectors, lower cost FSO communications links could be developed to provide an integrated satellite-terrestrial global network as seen in Figure 1.6(b). Ideally, such a network could allow for improved communication

services in remote areas or geographical regions which cannot support typical terrestrial networks well. Further information on the topic of FSO communication links can be found in two of Vincent Chan's invited papers [5][35].

1.3 Survey of Traditional Infrared Detection Architectures

Infrared detectors are absolutely vital to all of the MIR applications mentioned above in Section 1.2. In this section, we very briefly describe the working principles of several commonly used detectors to provide context for fundamental differences between standard detectors and the proposed microwave-based infrared architectures. Note that the aim is to merely provide background; for further in-depth reading on the well-known architectures, both Rogalski's [6] and Dereniak/Boreman's [36] textbooks are recommended.

1.3.1 Thermal Detectors

Several flavors of thermal detectors exist such as bolometers [37][38], pyroelectrics [39], thermopiles [40], and Golay cells. Despite differences between thermal detector types, the common detection mechanism is in the use of optically induced temperature changes. To illustrate this, consider a structure and circuit for a bolometer in Figure 1.7(a) and (b), respectively.

Light incident upon the bolometer's active element is absorbed. Typically, the active element is chosen to have small thermal capacities and large temperature resistance coefficients; thus, with less optical power, a greater change in temperature is produced, which in turn will manifest as a significant change in the active element's resistance. If the bolometer's active element is connected to a very simple circuit as shown in Figure 1.7(b),

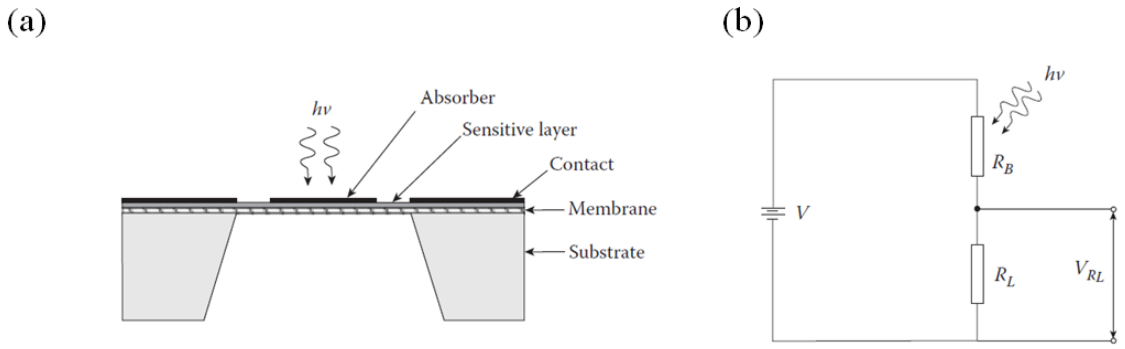

Figure 1.7: (a) Cross-sectional view of a standard bolometer; (b) basic detection circuit containing the bolometer; taken and adapted from [6]

a change in resistance of the active element due to optical absorption effectively modulates the voltage divided over a load. Although bolometers and thermal detectors in general can detect over the majority of the IR spectra, they are typically slower and potentially less sensitive than semiconductor-based photon detectors.

1.3.2 Junction Devices

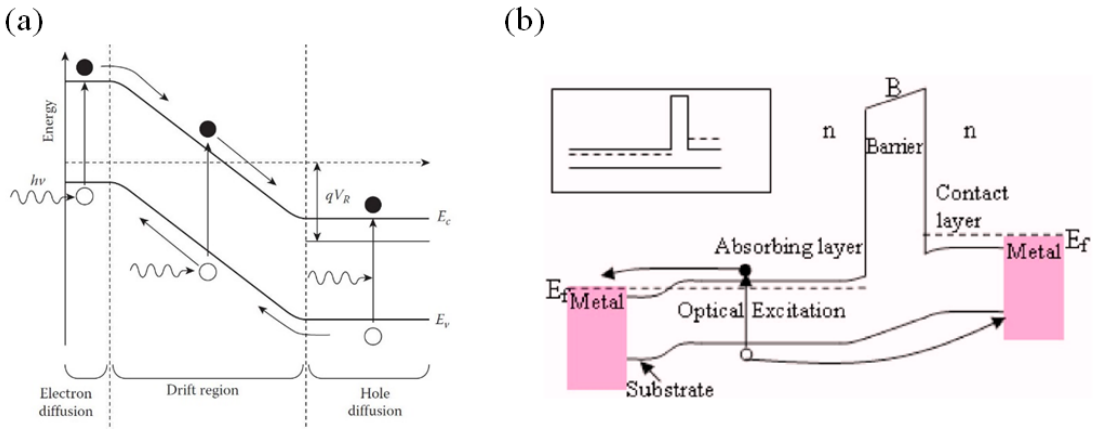

Figure 1.8: Representative band diagram of (a) pn junction based device and (b) nBn device under operation. Images taken and adapted from [6] and [7], respectively

Unlike thermal detectors which utilize temperature changes from incident radiation, photon-based detectors absorb incident light and generate electron-hole pairs (EHPs), which are typically collected or modulate an output voltage in a basic circuit. Junction-based photon detectors [41][42][43], for instance, have continuously seen incredible advances, especially in the mid-infrared. Traditionally, pn or pin junctions are used, as seen in Figure 1.8(a). Photons incident upon the detector are absorbed and generate EHPs. In a photovoltaic mode of operation, the device is operated at zero bias, so no external biasing circuit is required. The optically generated EHPs are separated by the intrinsic field in the junction, generating a potential from the absorbed light. In addition to not requiring a biasing circuit, photovoltaic operation is advantageous as it nominally possesses less dark current. Alternatively, in the so-called photoconductive mode, an external reverse bias is applied to the device which sweeps out generated EHPs as a photocurrent. Hence, with the applied bias, junction-based photodetectors can have incredibly fast response times and large bandwidths well into the GHz [44]. Although the biased detectors can have larger dark currents, identification of dark current mechanisms has allowed for advancements made in detector architectures. As an example, the popular nBn detector [7] shown in Figure 1.8(b) is a relatively recent junction-based architecture which has demonstrated low dark currents and high operating temperatures for both the mid- and long-wave infrared spectral regions [45][46].

1.3.3 The DC Photoconductor

The DC photoconductor, unlike the junction devices, requires no doping or complicated growth schemes and is therefore arguably the simplest of photon detectors. A

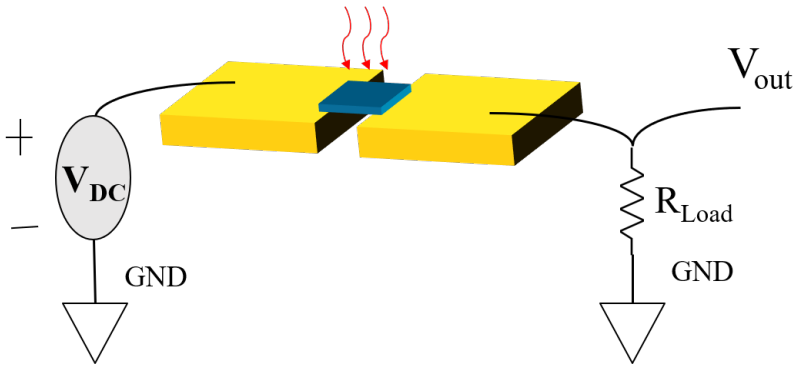

Figure 1.9: Schematic of a basic photoconductive circuit

schematic of the most basic photoconductive circuit is shown in Figure 1.9. Non-blocking ohmic contacts are formed to the optically active photoconductive element. A DC voltage bias is applied across the series combination of the photoconductive element and a second resistor, resulting in a voltage division between the two components. When light is incident upon and absorbed in the active material, electron-hole pairs (EHPs) are generated, which modulates the resistance and therefore the voltage divided over the output. This standard DC photoconductor will be discussed in detail in Chapter 5.

1.3.4 Reactively Coupled Detectors: An Introduction

Both junction devices and the above photoconductive device are direct current (DC) based systems which require a combination of ohmic contacts to the material and current/carrier collection. To alleviate this requirement, the work in this dissertation seeks to couple/load MIR optoelectronic materials to Ku band microwave resonant structures for both material characterization (Chapter 4) and light detection (Chapter 5) applications; note that the motivation and benefits of using contact-free architectures for each application are described in detail within the respective chapter.

Figure 1.10: Generalized block diagram of a microwave-based infrared detector utilizing reactively coupled absorbers

Instead of measuring any photocurrent or DC voltages, in the proposed structures, an RF transmission, or S_{21} parameter, is measured. Ideally, the microwave fields are concentrated and thus strongly interact with the material, and when optical illumination generates electron-hole pairs (EHPs) in the material, the amount of microwave signal transmitted accordingly changes. To implement such an architecture, five components are required: an optically active material, a microwave source and receiver, a microwave concentrator, and of course, a microwave feed/transmission line. Figure 1.10 shows a block diagram of the detection concept. The microwave concentrator is used to improve interaction between any loaded optoelectronic material and the relatively large free-space microwave. In the majority of this dissertation, the concentrator consists of a split ring resonator (SRR), which will be discussed in detail in Chapter 3. The absorber material is a semiconductor, either gallium arsenide (Chapters 3 and 6) or indium arsenide antimonide (Chapters 4 and 5). Finally, the transmission lines are either microstrips or coplanar waveguides, described in detail next in Section 1.4.

1.4 RF/Microwave Transmission Lines

In Subsection 1.3.4, it was mentioned that transmission lines are one of the basic components to reactively coupled microwave infrared detection architectures. Because microwaves are waves and no longer DC, they require signal feeding structures, or effectively, waveguides. In this subsection, a brief revision of the Telegrapher's equations and the general transmission line is given, followed by a description of the two primary on-chip transmission lines employed in this dissertation. In this section, we follow derivations and terminologies from David Pozar's textbook [8]. Only derivations relevant to the work are provided; thus, for further details and reading, the reader is referred to Pozar's textbook.

1.4.1 Telegrapher's Equations and the Terminated TLine

In this dissertation, both lumped and distributed elements will be used simultaneously. Lumped elements are essentially common circuit components (including reactive components such as inductors or capacitors) which can be used to describe structures in which the wavelength is sufficiently large relative to the component. However, in situations where a wave propagates through a structure of sufficient length, distributed elements must be used to consider the effects the structure has on the propagation characteristics of the wave. Transmission line waveguides are examples of structures in which propagation of the signal wave must be considered. In Figure 1.11, a very common model for an infinitesimal section of transmission line is given.

In Figure 1.11, G and R represent conductive and resistive losses in the line per unit length, respectively. Additionally, the inherent capacitance and inductance of the line per unit length are given as C and L, respectively. As Δz is decreased, with the application of

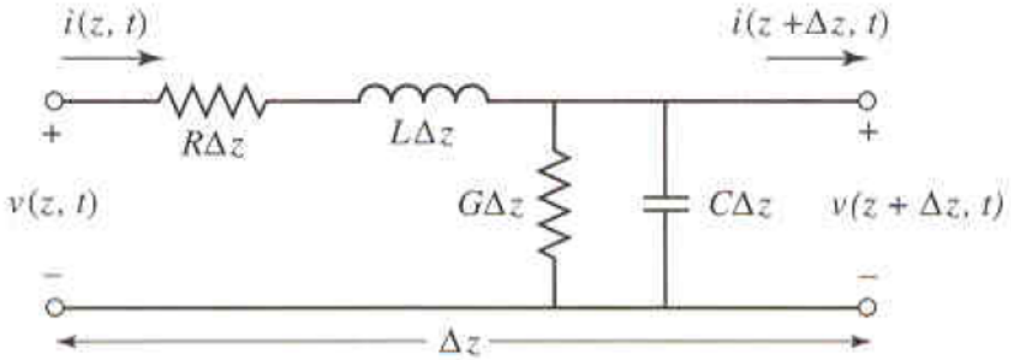

Figure 1.11: Lumped element model for a section of transmission line of length Δz. Image taken and adapted from Pozar's textbook [8]

Kirchoff's voltage and current laws, the output of transmission line can be expressed as:

$$\frac{\partial v(z,t)}{\partial z} = -Ri(z,t) - L\frac{\partial i(z,t)}{\partial t} \tag{1.1}$$

$$\frac{\partial i(z,t)}{\partial z} = -Gv(z,t) - C\frac{\partial v(z,t)}{\partial t} \tag{1.2}$$

Equations 1.1 and 1.2 are commonly referred to as the Telegrapher's equations, which is used to derive wave propagation along a transmission line. In the phasor domain (single sinusoidal harmonics), time derivatives can be replaced with $j\omega$:

$$\frac{dV(z)}{dz} = -(R + j\omega L)I(z) \tag{1.3}$$

$$\frac{dI(z)}{dz} = -(G + j\omega C)V(z) \tag{1.4}$$

By taking a second spatial derivative of Equation 1.3 and plugging it into Equation 1.4 for the spatial current derivative, the following is obtained:

$$\frac{d^2V(z)}{dz^2} = (R + j\omega L)(G + j\omega C)V(z) \tag{1.5}$$

$$\frac{d^2I(z)}{dz^2} = (R + j\omega L)(G + j\omega C)I(z) \tag{1.6}$$

To keep expressions and terminology consistent with textbooks and coursework, a propagation constant, γ, can be defined as:

$$\gamma = \sqrt{(R + j\omega L)(G + j\omega C)} = \alpha + j\beta \tag{1.7}$$

where α is a loss term (which is oftentimes neglected for simplicity) and β is typically referred to as the propagation constant. Combining the definition in Equation 1.7 with an exponential solution to Equation 1.5, the voltage signal at any given point on a full transmission line composed of a sum of lumped line pieces (as shown in Figure 1.11) can be conveniently expressed as:

$$V(z) = V_0^+ e^{-j\omega\gamma} + V_0^- e^{j\omega\gamma} \tag{1.8}$$

Equation 1.8 effectively shows that for a transmission line, the voltage will vary as a function of position on the line. Furthermore, the solution can be expressed as a sum of forward and backward traveling waves. On the transmission line, a characteristic impedance, Z_0, can be defined to express the ratio between voltage and current. However, as mentioned in

Subsection 1.3.4, the entire purpose of the transmission line in context of this dissertation is to feed microwave signal into and out of resonators. Hence, the transmission line is terminated with some dissipating load, which is generally denoted as Z_L. Now, there appears to be a contradiction: at the boundary of the line and load (which is typically defined as z = 0), the ratio of the voltage and current must also be equivalent to the load impedance. To satisfy this boundary condition, there must also be a reflected wave, V_0^-, which can be expressed as:

$$V_0^- = \Gamma V_0^+ \tag{1.9}$$

where Γ is the reflection coefficient, given by:

$$\Gamma = \frac{Z_L - Z_0}{Z_L + Z_0} \tag{1.10}$$

Thus, the signal on the line as a function of position can be solved for if the characteristic impedance, Z_0, and propagation constant, β, are known for a given transmission line structure. Next, in Subsection 1.4.2, the on-chip transmission lines used in this dissertation will be introduced. Further application of transmission line theory and modeling are described in the respective relevant chapter, such as the case of impedance mismatched line modeling described in Chapter 2 or the addition of a lumped capacitively coupled resonator in Chapter 3.

1.4.2 Common On-Chip Transmission Lines

While several RF and microwave transmission lines exist, this section will focus on two that are employed in this dissertation: the microstrip and the grounded coplanar waveguide, shown in Figure 1.12(a) and (b) respectively.

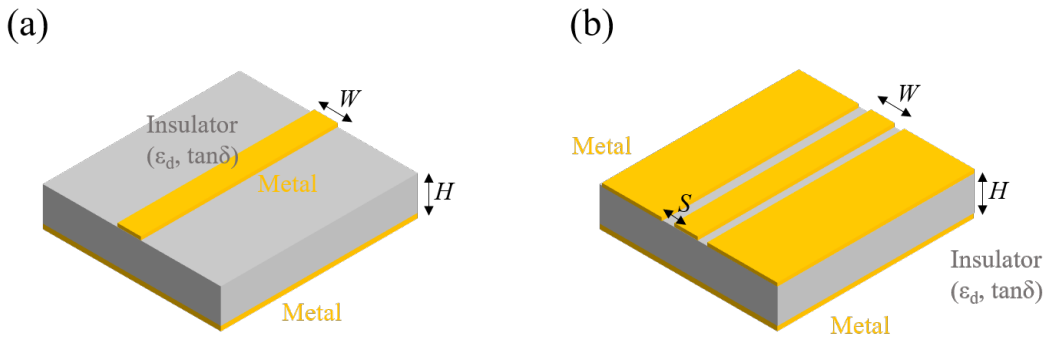

Figure 1.12: Schematic of (a) microstrip waveguide with made with a dielectric constant, ϵ_d, loss tangent $tan\delta$, dielectric thickness, H, and strip width, W; (b) grounded coplanar waveguide with dielectric constant, ϵ_d, loss tangent $tan\delta$, dielectric thickness, H, strip width, W, and slot width, S

As mentioned previously in Subsection 1.4.1, to adequately model the signal in these transmission lines, expressions for both the characteristic impedance (Z_0) and the effective mode permittivity (ϵ_{eff}) must be given. Due to the popularity of these two waveguide structures, well-known expressions are commonly employed.

For the microstrip, the expressions are given as [8]:

$$Z_{0u} = \frac{60}{\sqrt{\epsilon_{eff}}} ln\left(\frac{8H}{W} + \frac{W}{4H}\right) \tag{1.11}$$

$$\epsilon_{effu} = \frac{\epsilon_d + 1}{2} + \frac{\epsilon_d - 1}{2}\left[\frac{1}{\sqrt{1 + \frac{12H}{W}}} + 0.04\left(1 - \frac{W}{H}\right)^2\right] \tag{1.12}$$

for when $W/H < 1$; however, when $W/H > 1$:

$$Z_{0u} = \frac{120\pi}{\sqrt{\epsilon_{eff}}} \frac{1}{\left(\frac{W}{H} + 1.393 + 0.677ln\left(\frac{W}{H} + 1.444\right)\right)} \tag{1.13}$$

$$\epsilon_{effu} = \frac{\epsilon_d + 1}{2} + \frac{\epsilon_d - 1}{2}\left[\frac{1}{\sqrt{1 + \frac{12H}{W}}}\right] \tag{1.14}$$

The propagation constant can then readily be obtained from the effective permittivity:

$$\beta = \frac{2\pi\sqrt{\epsilon_{effu}}}{\lambda} \tag{1.15}$$

where λ is the wavelength of the microwave signal on the transmission line.

Similarly, well-known expressions for the characteristic impedance of the grounded coplanar waveguide are given in [47], though these expressions typically have a larger degree of complexity; these impedance calculators can commonly be found online and can be used to easily compute Z_{0cpw} and ϵ_{effcpw}. Thus far, only a basic introduction to transmission line theory has been provided. In Chapter 2, the case of mismatched transmission lines will be considered, which is relevant to the work in the rest of this dissertation.

Chapter 2

Modeling and Experimental Setups

This chapter introduces some general characterization techniques employed in the Wasserman lab as well as basics with regard to modeling the microwave circuits. Because several chapters of this dissertation describes novel characterization techniques, only well-known techniques used in our lab are described in this section. All specifics regarding the techniques developed as part of this dissertation are described within their respective chapters.

2.1 Modeling Methods and Example Calculations

This section describes three of the key modeling methods used in later chapters of the dissertation. The first subsection discusses solving mismatched transmission line equations, specifically with regard to obtaining an expression for the signal transmitted to the load. Next, some basics of the driven finite element method used in chapter three are reviewed. Finally, the last subsection gives a brief overview of the backwards Euler method, the technique used by the open-source time domain solver.

2.1.1 Mismatched Transmission Lines: A General Case

In Chapter 1, the concept of transmission lines was discussed, and accepted expressions for the characteristic impedance and propagation constant were given for both the microstrip and grounded coplanar waveguide. In this subsection, a common methodology for solving for the signal reaching a terminating load in the general case of mismatched transmission lines is provided. The procedure is important as the majority of work in this dissertation uses microwave ground-signal-ground (GSG) probes, and the port pads that are probed can be treated as a section of transmission line which may have different propagation characteristics from the primary microstrip busline, as illustrated below in Figure 2.1:

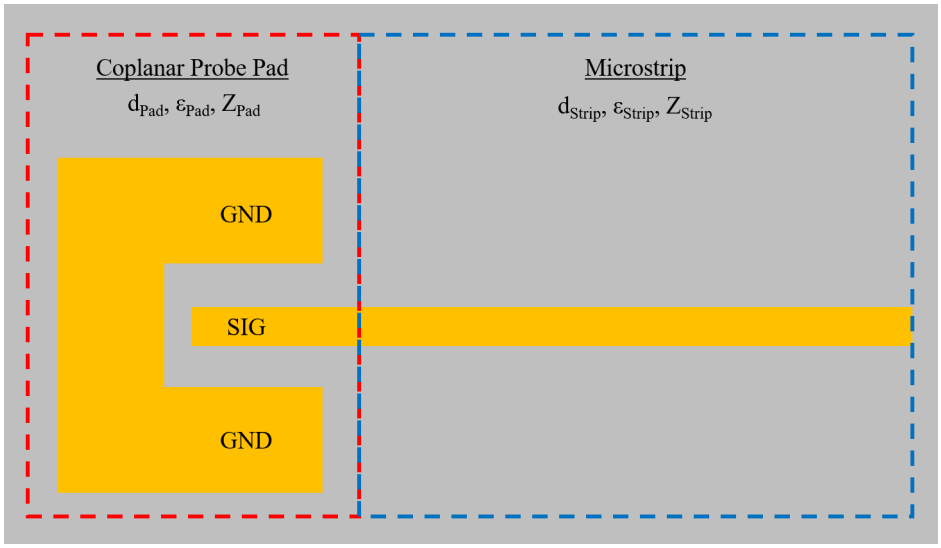

Figure 2.1: Overhead view of of an example port. The gold regions represent metal (typically gold in this dissertation) and the gray represents an insulator. A ground-signal-ground (GSG) probe makes contact to the coplanar probe pad (red dashed lines), which has a length, effective permittivity, and characteristic impedance. This pad can then lead into a microstrip, which has its own set of parameters describing propagation

Figure 2.1 represents a port used in nearly all of the work in this dissertation, a

coplanar pad consisting of a "U" shaped ground pad and the termination (either the end or beginning) of a microstrip transmission line; hence, being able to model the mismatch between the coplanar pad and microstrip is of significance. To do so, consider the following equivalent transmission line model:

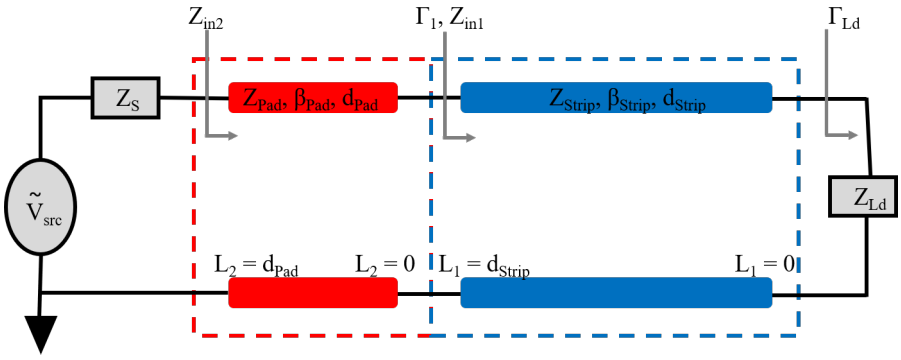

Figure 2.2: Transmission line model representation of Figure 2.1 with a source and source impedance, Z_S, and load termination of Z_L. The coplanar pad (red) and microstrip transmission line (blue) each have their own lengths, propagation constants, and characteristic impedances. Input impedances and reflection coefficients are defined at each node or potential mismatch.

From chapter one, using Equation 1.10, which describes the reflection coefficient between a line and load termination, the expressions for the reflection coefficient at the load, Γ_{Ld}, and Z_{in1} as defined in Figure 2.2, become [8]:

$$\Gamma_{Ld} = \frac{Z_{Ld} - Z_{Strip}}{Z_{Ld} + Z_{Strip}} \tag{2.1}$$

$$Z_{in1} = Z_{Strip}\frac{1 + \Gamma_{Ld}e^{-2j\beta_{Strip}d_{Strip}}}{1 - \Gamma_{Ld}e^{-2j\beta_{Strip}d_{Strip}}} \tag{2.2}$$

From this, the problem simply transforms to a simpler circuit consisting of the input port terminated by an input impedance Z_{in1}; Z_{in1} can now be treated as the new effective load,

as seen in Figure 2.3.

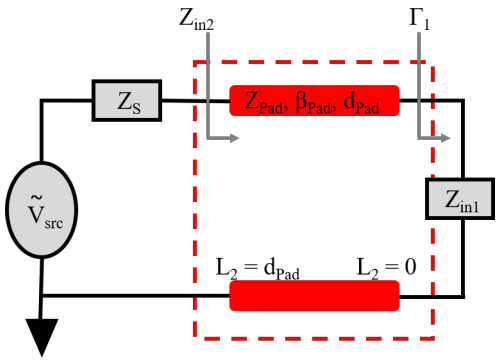

Figure 2.3: First transmission line reduction. Once Z_{in1} is computed, the problem in Figure 2.2 can be reduced to simply the coplanar pad line terminated by Z_{in1}, which now serves as the effective load

Repeating the procedure above, Γ_1 and Z_{in2} can now be computed as:

$$\Gamma_1 = \frac{Z_{in1} - Z_{Pad}}{Z_{in1} + Z_{Pad}} \tag{2.3}$$

$$Z_{in2} = Z_{Pad}\frac{1 + \Gamma_1 e^{-2j\beta_{Pad}d_{Pad}}}{1 - \Gamma_1 e^{-2j\beta_{Pad}d_{Pad}}} \tag{2.4}$$

Finally, the entire effective input impedance, Z_{in2}, can be placed in series with the the source impedance, Z_S, as shown in Figure 2.4.

The goal is now to find an expression for the amplitude of V_2^+, the amplitude of the forward traveling voltage wave on the coplanar pad transmission line. Generally, the voltage on any section of the line can be described as:

$$V(L) = V^+(e^{-j\beta L} + \Gamma e^{j\beta L}) \tag{2.5}$$

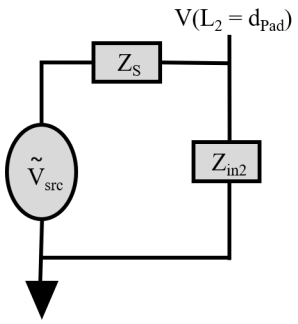

Figure 2.4: Final circuit reduction. Once Z_{in2} is computed, Figure 2.3 can be reduced to this diagram. The voltage dropped over Z_{in2}, which is equivalent to $V(d_{Pad})$, is obtained through simple voltage division

Furthermore, it becomes clear that the voltage dropped over Z_{in2} is equivalent to the voltage at $L_2 = d_{Pad}$ shown in Figure 2.3. Hence:

$$V(Z_{in2}) = V(L_2 = d_{Pad}) = V_2^+(e^{-j\beta_{Pad}d_{Pad}} + \Gamma_1 e^{j\beta_{Pad}d_{Pad}}) = V_{src}\frac{Z_{in2}}{Z_{in2} + Z_S} \tag{2.6}$$

And so, the forward traveling wave on the coplanar pad, V_2^+, is readily solved for:

$$V_2^+ = V_{src}\frac{Z_{in2}}{Z_{in2} + Z_S}\frac{1}{(e^{-j\beta_{Pad}d_{Pad}} + \Gamma_1 e^{j\beta_{Pad}d_{Pad}})} \tag{2.7}$$

Next, the voltage at Z_{in1} which is the beginning of the stripline ($L_1 = d_{Strip}$) can be solved for by realizing that it is equivalent to the end of the coplanar pad ($L_2 = 0$ for the pad is equivalent to $L_1 = d_{Strip}$ for the microstrip). And so, using Equation 2.5:

$$V(Z_{in1}) = V(L_1 = d_{Strip}) = V(L_2 = 0) = V_2^+(1 + \Gamma_1) \tag{2.8}$$

The forward traveling wave on the microstrip, V_1^+, can then be solved for as:

$$V_1^+ = V_2^+(1+\Gamma_1)\frac{1}{(e^{-j\beta_{Strip}d_{Strip}} + \Gamma_{Ld}e^{j\beta_{Strip}d_{Strip}})} \tag{2.9}$$

And, finally, the voltage at the load is simply:

$$V_{Ld} = V(L_1 = 0) = V_1^+(1+\Gamma_{Ld}) \tag{2.10}$$

In this dissertation, because the load is often a power detector (such as a Schottky diode operated in a square law region in which the output voltage is proportional to input power dissipated), the power dissipated over the load is also a useful quantity:

$$P_{Ld} = \frac{1}{2}Re\{V_{Ld} \times (\frac{V_{Ld}}{Z_{Ld}})^*\} \tag{2.11}$$

where the asterisk denotes complex conjugation.

2.1.2 Finite Element Method

Portions of this dissertation, especially Chapter 3 , use Ansys HFSS, a commercial finite element method (FEM) software [48]. It should be noted that entire textbooks on FEM have been written as the field is incredibly extensive. As such, this section will merely provide a brief introduction to the concept and provide a context to the work presented in this dissertation. For further analysis and understanding, the reader is referred to Prof. Jianming Jin's FEM textbook [49].

Consider the following arbitrary function, f, which is dependent on some variable such as position, x. If the functional relationship can be expressed as a differential equation, then generally:

$$A\frac{d^2 f}{dx^2} = B \tag{2.12}$$

Although there are many structures and situations in which the solution can be analytically determined, a general approach to solving difficult structures numerically is desirable, especially in the context of this dissertation. As mentioned in Chapter 1, even relatively simple structures, such as microstrip waveguides, do not possess entirely analytical solutions [8]. Hence, a quantity f (which, as an example, could refer to field distributions) as a function of x, in a situation that cannot be solved analytically, can be broken up as:

$$f = \sum_{i=1}^{n} \phi_i f_i \tag{2.13}$$

Typically, a complex 3D model is broken into smaller pieces, or finite elements which constitute a mesh. Positions where these finite elements connect can be referred to as nodes. To determine where to break a 3D structure and create nodes, many commercial FEM software have some form of adaptive meshing. In adaptive meshing, once the software identifies a region of rapidly changing function or high gradient, it re-meshes (for example, breaks into smaller pieces, as seen in Figure 2.5) the region and repeats the computation. Then, if the difference in solution between the new mesh and old mesh is less than a user-defined tolerance, the solution is considered converged. If not, the solution will try again iteratively for a user-defined number of times.

However, to actually obtain a usable solution to Equation 2.13, there are two common methods (among others) employed, depending on whether the problem possesses a known differential equation (Galerkin method), or if it has a functional that can be minimized (Ritz

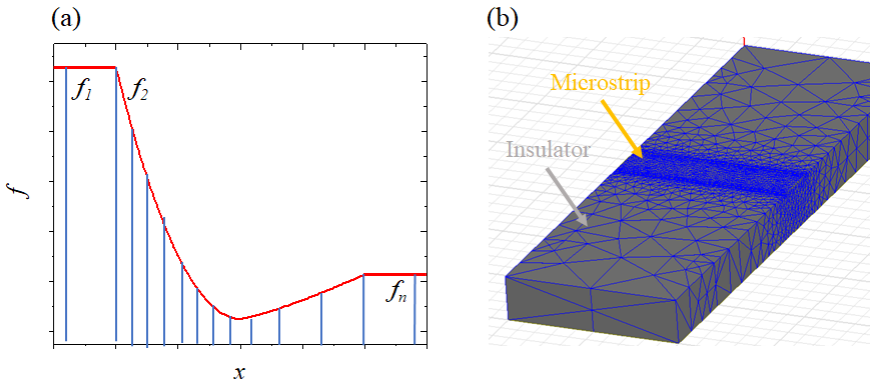

Figure 2.5: (a) Sample arbitrary function, f, as a function of x. The function is split at the blue lines into n pieces, with a denser set of pieces in regions of rapidly changing function or large gradients; (b) example of a mesh pattern in a simple microstrip FEM simulation

variational method)[49]. Further details on the actual algorithms used by the FEM solver can be found in [49] [50][51][52] as they are well beyond the scope of this dissertation.

The commercial FEM simulation software used in this dissertation is Ansys HFSS. Typically, the program creates a mesh using tetrahedral-shaped elements, as seen in Figure 2.5(b). Adaptive meshing algorithms refine the mesh in regions of highly varying function, as mentioned above. In this dissertation, driven solutions are employed in which excitation ports are defined on the 3D model, and reflected and transmitted signals are computed [48]. The application of HFSS toward our structures is described in further detail in Chapter 3.

2.1.3 Time Domain: Backwards Euler Method

The lumped element model formulation presented in an earlier subsection is quite effective for frequency domain transfer function modeling of well-known structures. Alternatively, the use of FEM approaches are more appropriate for the design and modeling of

more complicated geometries. However, both of these models use a coherent source (single frequency, single phase signal) as the input and define transfer functions or scattering parameters for the case of a coherently driven circuit. Chapter 5 of this dissertation models different forms of incoherent noise sources; hence, there exists a need to use a strictly time domain method rather than the above two approaches, which assume coherence, solve in the frequency domain, and then take a Fourier transform. To this end, time domain circuit modeling is done using transient analysis in LTSpice, an open-source circuit modeling software, which uses the Backwards Euler (BE) method, a well-known numerical technique, to solve time domain equations. Because the resonant circuits used in this dissertation will have reactive components such as capacitors and inductors, expressions for voltage and current will contain differential equations:

$$I(t) = C\frac{dV(t)}{dt} \tag{2.14}$$

$$V(t) = L\frac{dI(t)}{dt} \tag{2.15}$$

Hence, when several reactive components are present in a circuit and incoherent sources are introduced, a numerical technique is desirable. The basic principle behind the BE technique is rather straightforward: given a voltage, $v(t)$, the voltage at a given discrete time point, N+1, can be expressed in terms of the voltage at time N and an approximate slope:

$$v(t)_{N+1} \approx v(t)_N + h\frac{dv(t)_{N+1}}{dt} \tag{2.16}$$

where h represents the time step, Δt, between N and $N+1$ instances in time. Thus, the time derivative term in Equation 2.14 can be simplified using Equation 2.16. Furthermore, if $I = \frac{dQ}{dt}$ and $Q = CV$, where Q is the charge, after applying trapezoidal integration, Equation 2.16 can be expressed using only linear components. As an example, when performing basic circuit nodal analysis on a capacitor, a companion model composed of linear elements can be used to replace the capacitor as seen in Figure 2.6[9]

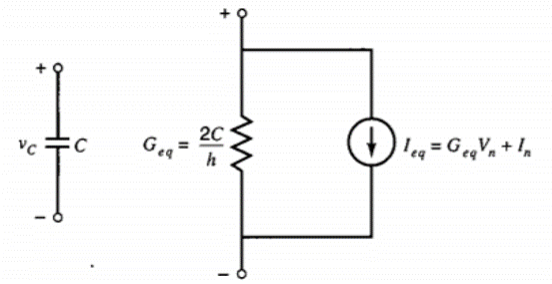

Figure 2.6: Example of a linear companion model for a capacitor; taken and adapted from [9]

LTSpice, the open-source software used in Chapter 5, breaks down components such as capacitors and inductors into a so-called linear companion models using the BE method outlined above to obtain an output signal as a function of time at a given/desired node. Similar to the FEM software mentioned in the previous section, the transient analysis identifies instances in time where the signal changes rapidly and dynamically reduces the time step accordingly; however, the user can define a maximum step size. The LTSpice simulations are used in Chapter 5 to model incoherent noise sources; specifically, we seek to understand via time-domain modeling how a microwave resonator modifies sources of noise generated by a semiconductor placed within.

2.2 Microwave Characterization

This section describes some general microwave engineering concepts as well as the basic working principles of the vector network analyzer, the instrument used in most of the microwave characterization techniques employed throughout the dissertation. The first subsection describes the concept of scattering parameters (S-parameters) and derives the conversion from the S-matrix to the impedance matrix (Z-matrix), which will be of importance later in Chapter 5.

2.2.1 Scattering Parameters and 2-Port Z-Matrix Conversion

Let us start by considering Figure 2.7 which shows a microwave circuit with N number of ports, or input/outputs. Each port has a voltage or current associated with it; however, the port can be considered to be simultaneously an input and output as both voltages and currents can be described by waves both entering (defined with a "+" superscript) and exiting (defined with a "−" superscript). Furthermore, in the general case, a voltage introduced in one port interacts with the microwave circuit and can manifest in the output of another port.

The "scattering parameter", or S-parameter for short, can be used to describe the ratio of the voltage at port i relative to port j, where i is not necessarily equal to j:

$$S_{ij} = \frac{V_i^-}{V_j^+} \tag{2.17}$$

Hence, for an N-port network, the voltage measured at one port due to a voltage at another port can be described by an $N \times N$ "S" Matrix:

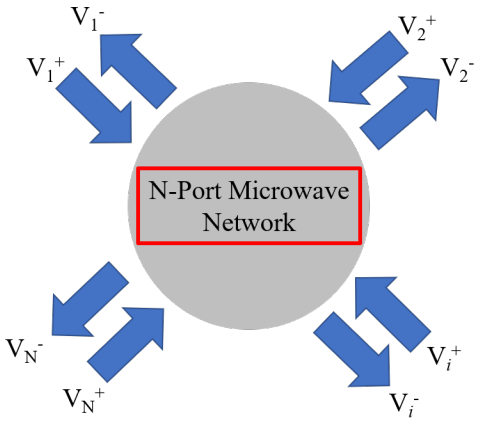

Figure 2.7: N-port network diagram. Each port has a signal, in this case a voltage, which enters (labeled with a "+" superscript and exits (labeled with a "-" superscript) the port

$$\begin{bmatrix} V_1^- \\ V_2^- \\ \dots \\ V_N^- \end{bmatrix} = \begin{bmatrix} S_{11} & S_{12} & \dots & S_{1N} \\ S_{21} & S_{22} & \dots & S_{2N} \\ \dots & \dots & \dots & \dots \\ S_{N1} & \dots & \dots & S_{NN} \end{bmatrix} \begin{bmatrix} V_1^+ \\ V_2^+ \\ \dots \\ V_N^+ \end{bmatrix} \tag{2.18}$$

However, in this dissertation, the circuits used are predominantly two-port networks, which allows the S matrix to be simplified to:

$$\begin{bmatrix} V_1^- \\ V_2^- \end{bmatrix} = \begin{bmatrix} S_{11} & S_{12} \\ S_{21} & S_{22} \end{bmatrix} \begin{bmatrix} V_1^+ \\ V_2^+ \end{bmatrix} \tag{2.19}$$

The S-parameters are especially important as they can be measured using a vector network analyzer (VNA), discussed in Subsection 2.2.2. That being said, there are many situations, such as in the discussion of noise in chapter five, in which the use of the impedance matrix (Z-matrix) is more convenient. The Z-matrix, or impedance matrix, is used to describe the Z-parameters, or ratio between the voltage applied at port i and current entering port j. For the general case, the relationship between the Z-matrix and S-matrix is as follows [8]:

$$[Z] = ([I_N] + [S]) \times ([S] - [I_N])^{-1} \tag{2.20}$$

where $[I_N]$ represents the $N \times N$ identity matrix. Assuming a two-port network, Equation 2.20 can be expanded and the Z-parameters solved from the S-parameters:

$$\begin{bmatrix} Z_{11} & Z_{12} \\ Z_{21} & Z_{22} \end{bmatrix} = (\begin{bmatrix} 1 & 0 \\ 0 & 1 \end{bmatrix} + \begin{bmatrix} S_{11} & S_{12} \\ S_{21} & S_{22} \end{bmatrix}) \times (\begin{bmatrix} S_{11} & S_{12} \\ S_{21} & S_{22} \end{bmatrix} - \begin{bmatrix} 1 & 0 \\ 0 & 1 \end{bmatrix})^{-1}$$

$$= \begin{bmatrix} 1 + S_{11} & S_{12} \\ S_{21} & 1 + S_{22} \end{bmatrix} \times (\begin{bmatrix} S_{11} - 1 & S_{12} \\ S_{21} & S_{22} - 1 \end{bmatrix})^{-1}$$

$$= \begin{bmatrix} 1 + S_{11} & S_{12} \\ S_{21} & 1 + S_{22} \end{bmatrix} \times \frac{1}{(S_{11} - 1)(S_{22} - 1) - S_{21}S_{12}} \begin{bmatrix} S_{22} - 1 & -S_{12} \\ -S_{21} & S_{11} - 1 \end{bmatrix}$$

$$\begin{bmatrix} Z_{11} & Z_{12} \\ Z_{21} & Z_{22} \end{bmatrix} = Z_0 \begin{bmatrix} \frac{(1+S_{11})(1-S_{22})+S_{12}S_{21}}{(S_{11}-1)(S_{22}-1)-S_{21}S_{12}} & \frac{2S_{12}}{(S_{11}-1)(S_{22}-1)-S_{21}S_{12}} \\ \frac{2S_{21}}{(S_{11}-1)(S_{22}-1)-S_{21}S_{12}} & \frac{(1-S_{11})(1+S_{22})+S_{12}S_{21}}{(S_{11}-1)(S_{22}-1)-S_{21}S_{12}} \end{bmatrix} \tag{2.21}$$

Since the circuits investigated in this dissertation are both reciprocal and symmetric, $S_{22} = S_{11}$ and $S_{12} = S_{21}$, so Equation 2.21 can be simplified, and the Z-parameters can be written as:

$$Z_{11} = Z_0 \frac{1 - S_{11}^2 + S_{21}^2}{(1 - S_{11})^2 - S_{21}^2} \tag{2.22}$$

$$Z_{21} = Z_0 \frac{2S_{21}}{(1 - S_{11})^2 - S_{21}^2} \tag{2.23}$$

Because the real part of the impedance is related to dissipated power, it can oftentimes be useful to describe a network in terms of its Z-parameters. For example, as will be described in Chapter 5, the rms voltage fluctuations from thermal noise are related to the dissipating element. Thus, the Z-parameters are used in Chapter 5 to describe thermal noise generated by the overall input impedance of a terminated two-port network.

2.2.2 Vector Network Analyzer and Calibration Techniques

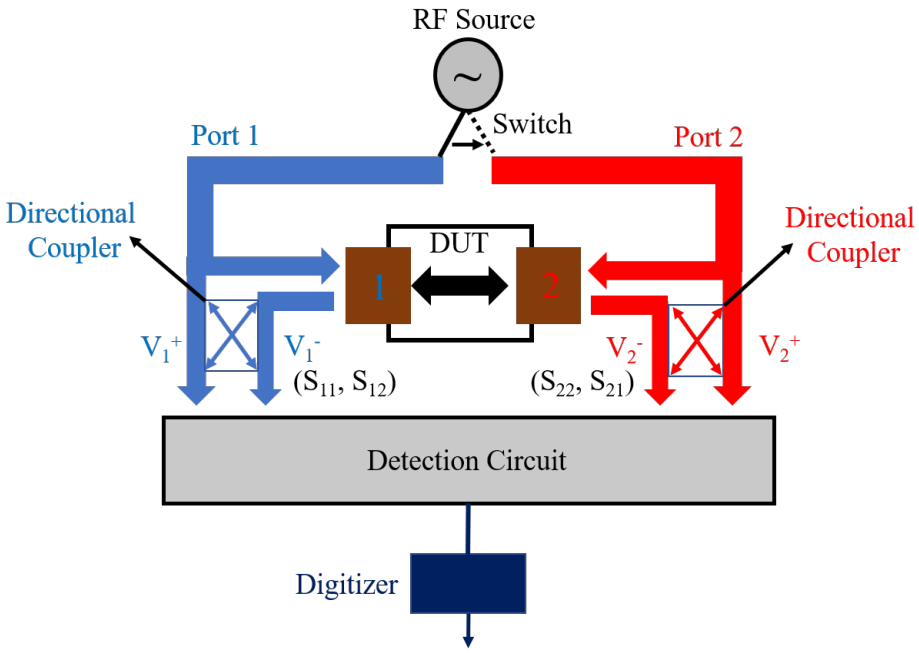

Figure 2.8: Diagram for the methodology of vector network analysis performed on a device under test (DUT)

To obtain the S-parameters mentioned in the Subsection 2.2.1, a vector network analyzer (VNA) is typically used. A basic diagram of a two port VNA is shown in Figure 2.8. An RF source is connected to a switch which determines the port that drives the circuit.

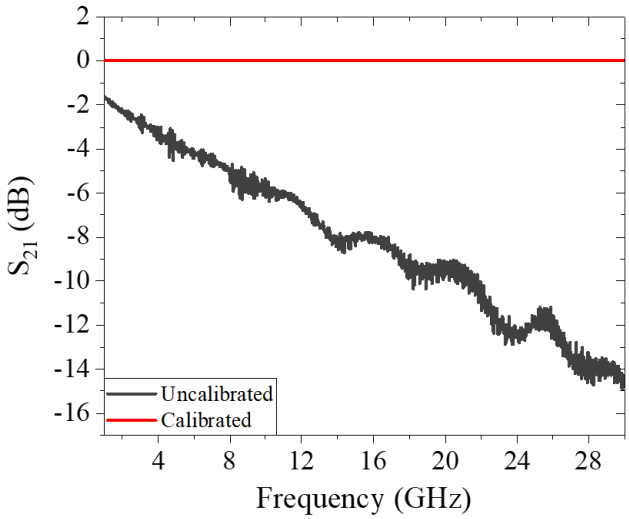

Figure 2.9: S_{21} spectra of both an uncalibrated (dark gray) and calibrated (red) matched coplanar waveguide. The calibrated curve accounts for the cables and probes and produces an ideal S_{21} across all frequencies

From here, for a given port, a signal selection module (typically a directional coupler) is used to pick either the forward traveling incident signal or the backward reflected signal. The signal is sent to the detection circuit, which typically consists of a tuned receiver that mixes the signal with a local oscillator and filters the intermediate frequency (IF) for digitizing. The output from the digitizer can then be readily converted between desired parameters and output onto a screen. The measured parameter depends on the port the source switch is currently set to. For example, if the source switch is set to port one, then the reflected signal from the port one directional coupler can be normalized to the port one incident signal, resulting in a S_{11} measurement. Conversely, if the switch is set to port two, the signal from the directional coupler in port one is normalized to the incident signal from the port two side, resulting in an S_{21} measurement.

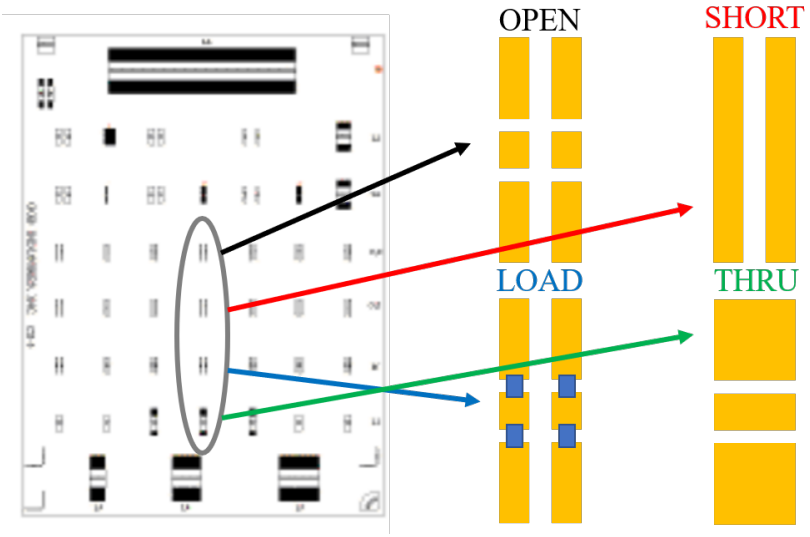

Figure 2.10: Schematic of the CS-5 calibration (left) substrate sold by GGB Industries for probe calibration; the calibration standards used are circled and expanded for clarity on the right

However, the reference plane, the location from which the parameters are measured, is typically at the front panel of the VNA. This is not ideal, as testing of devices typically requires cables and sometimes probes connected between the front of the VNA and the device under test (DUT). Hence, typically, calibration methods are employed to account for any testing equipment; in this dissertation most of the calibration accounts for losses and dispersive effects from both cables and probes. This is clearly seen in Figure 2.9, which compares the calibrated and uncalibrated S_{21} measurement of a lossless on-chip coplanar waveguide. The red curve shows the expected S_{21} parameter achieved after applying a calibration; however, if a calibration is not applied, it is clear from the dark gray curve that the S_{21} parameter can be significantly affected by the loss in the cables and probes, especially at higher frequencies. While several calibration techniques exist, this dissertation uses the short-open-load-thru (SOLT) technique. Essentially, each port (with the cable and

probe connected) is terminated with well-known, calibrated references. From Equation 2.1, it's clear that open and short terminations reflect all of the voltage, differing only in phase (0 versus π phase shift, respectively). A matched load results in zero reflection, and a matched thru allows all of the signal to travel from one port to the other. After calibration of cables and probes, an ideal S_{21} curve is produced as seen in the red curve of Figure 2.9. To perform the calibration, well-known calibrated references are required; in this dissertation, the CS-5 substrate sold by GGB Industries is used, as seen in Figure 2.10. Careful calibration allows for a clear picture of the DUT performance and RF properties, without the effects of probe and cable loss and dispersion, and is thus an essential component of any microwave measurement.

2.3 Optical Characterization

The following section is the final portion of this chapter, and describes optical characterization techniques used in this dissertation. The basic measurements described include well-known characterization techniques developed for our group's applications, as well as techniques improved upon by several Wasserman group members, including myself. First, Subsection 2.3.1 describes the basics of Fourier transform infrared (FTIR) spectroscopy, a common technique employed in our lab for measuring infrared spectra. The concept of amplitude modulation step scan and the use of the lock-in amplifier (LIA) is emphasized and applied toward mid-infrared photoluminescence (PL) in Subsection 2.3.2. Finally, the time-resolved photoluminescence (TRPL) setup in the lab is described in Subsection 2.3.3, although it should be noted that details on lifetime techniques are described in depth in Chapter 4.

2.3.1 Fourier Transform Infrared Spectroscopy

At shorter wavelengths, such as the visible and near-IR (VIS/NIR), spectral response is measured using diffractive elements which separate incident light spatially by wavelength. A schematic of such an instrument, the monochromator, is shown in Figure 2.11. While there are several flavors of this technique, the general approach is to have light incident upon a diffractive grating, from which different wavelengths diffract at different angles. Then, either a CCD array simultaneously captures the spatially separated light at the different positions and maps position to wavelength, or the grating is rotated, and the diffracted light is captured by a single element detector. Either of these configurations allow for a direct measurement of intensity as a function of wavelength, as the measured light intensity is dependent upon the angle of the diffracted light, which is directly related to wavelength.

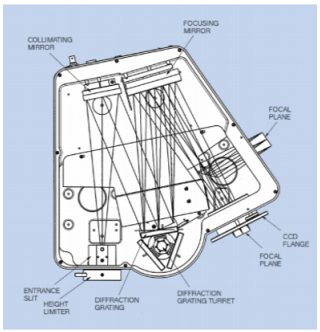

Figure 2.11: Sample diagram of a commercial monochromator from Horiba

FTIR spectroscopy [53] [54], on the other hand, is a more indirect measurement of spectra as it uses the reciprocal space relationship between wavenumber/momentum and spatial position. Instead of a grating, the FTIR spectrometer uses a Michelson interferometer, shown in Figure 2.12. A source is incident upon the interferometer and encounters a 50/50 beamsplitter. Half of the light enters the first arm of the interferogram with a fixed

mirror whereas the other half enters the arm with a movable mirror. Both beams then return to the beamsplitter and proceed to the detector. As the mirror moves in the second arm, the overall path length difference for the light in the two arms varies as a function of mirror position, which, along with wavelength, determines the interference (constructive or destructive) of the recombined beams incident upon the detector. The detector response can then be plotted as a function of mirror position, as shown in Figure 2.13 (a) and (b); these plots are known as the interferograms, as they represent the collective interference of recombined light incident upon the detector as a function of mirror position. Figure 2.13 shows interferograms of two different types of sources: in (a), the source is coherent and monochromatic (a 10.6 μm CO_2 laser), resulting in a periodic interferogram. A single frequency source will result in an interferogram having a single spatial frequency interferogram, while the coherence of the source determines the effective breadth of the interferogram oscillations. As the mirror moves as a function of position, the path length difference alternates between positions giving constructive (peaks, at path length differences of $n\lambda$) and destructive (nulls, at path length differences of $n\lambda/2$) interference regimes (where n is an integer). For an incoherent source's interferogram (Figure 2.13(b)), we see a relatively constant response on the interferogram until the mirror reaches near zero path difference (ZPD). Near the ZPD point, strong oscillations are observed, with the signal peaking at ZPD. At ZPD, the mirror is at a position in which the path lengths between the two arms of the interferometer are equal; hence, all wavelengths constructively interfere. The shape of this interferogram suggests that all incoherent sources actually possess a degree of coherence, but as the mirror moves away from ZPD, the limted coherence of the source decreases the amplitude of the interference fringes.

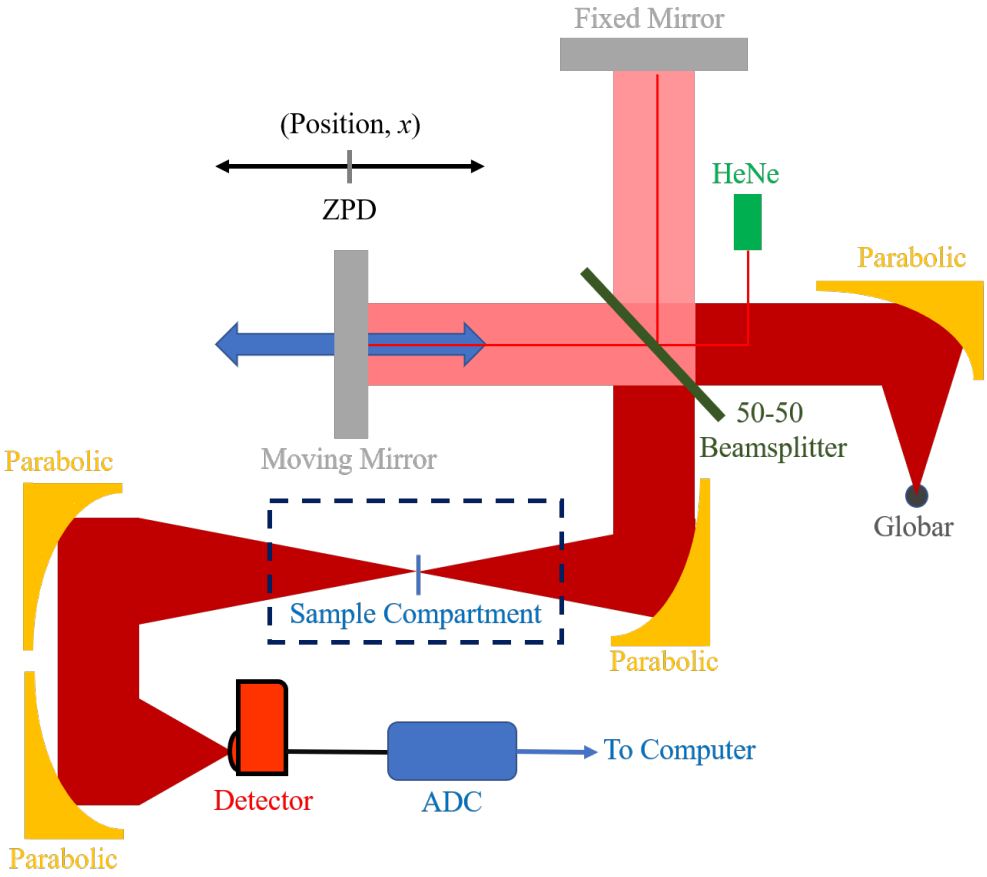

Figure 2.12: Schematic of an example FTIR spectrometer. This particular configuration shows an experimental setup for transmission through a sample; however, other setups maintain similar interferometry principles. To characterize a source, an entrance port couples external light, instead of the internal globar, into the interferometer. Conversely, for typical detector characterization, broadband light from the globar is sent out of the FTIR from an exit port and is incident upon the detector to be characterized. The signal from the detector is then measured as a function of mirror position to obtain the interferogram.

To obtain a spectrum from the interferogram, we must first convert to the reciprocal space quantity of position: namely momentum/wavenumber. In general, a physical quantity such as angular frequency, ω, can be expressed in terms of its reciprocal space quantity, such as time (t) through the use of a continuous Fourier transform (Equation 2.24) or more practically, the discrete Fourier transform (Equation 2.25):

$$F(\omega) = \int_{-\infty}^{\infty} f(t) e^{-j\omega t} dt \tag{2.24}$$

$$F_n = \sum_{k=0}^{N-1} f_k e^{-jkn/N} \tag{2.25}$$

Utilizing the reciprocal space relationship between position and momentum/wavenumber, a discrete Fourier transform is then applied, converting the interferogram to a spectrum as a function of wavenumber. By inverting the wavenumber, a conversion to wavelength is possible, and allows for a spectrum as a function of wavelength as shown in Figure 2.13 (c) and (d).

Oftentimes, there are advantages to measuring the reciprocal of the desired measured quantity and then utilizing Fourier analysis/transforms to retrieve the desired quantity. Fourier transform infrared (FTIR) spectroscopy is a methodology that falls under this category, and has three primary well-known advantages [54]:

1. *Throughput advantage (Jacquinot):* FTIR spectrometers measure all wavelengths of the detected light at once, as opposed to monochromators which split by the wavelength, with increased resolution resulting in even less light incident upon the detector. Furthermore, FTIR spectrometers oftentimes have larger circular apertures when compared to the slits

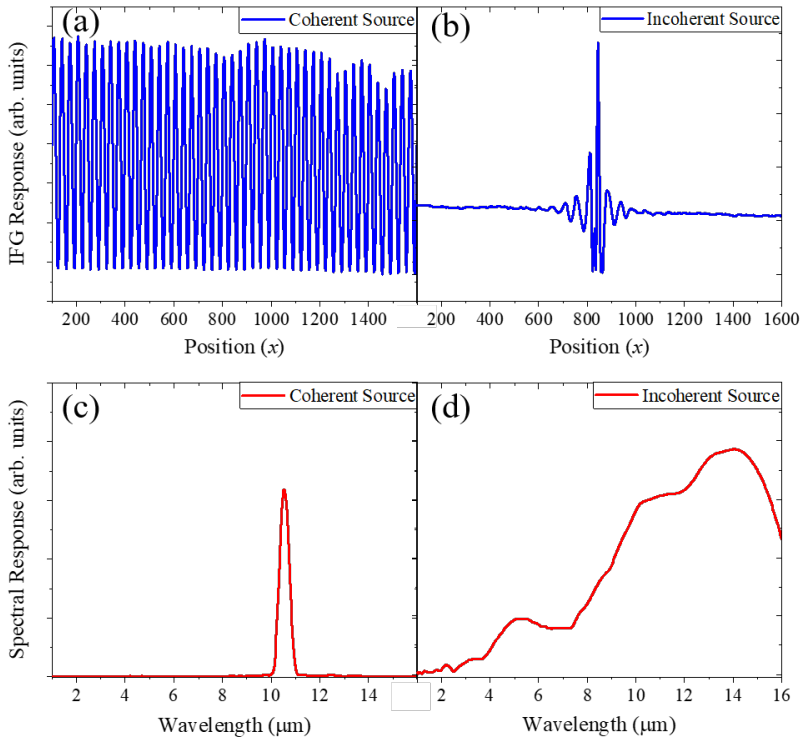

Figure 2.13: Interferograms (IFGs) of both (a) coherent and (b) incoherent sources. After applying a Fourier transform, the IFGs give the spectra shown for the (c) coherent and (d) incoherent sources

of monochromators, which also allows for more light incident upon the detector. The throughput advantage is also known as the Jacquinot advantage, and is possibly the most important advantage when working with incredibly poor signal to noise ratios (SNRs), which is often the case in the mid-infrared.

2. *Speed advantage (Fellget):* The FTIR spectrometer can take an incredible number of scans within a given time as, once again, all wavelengths are simultaneously collected. Hence, the speed, or time taken to complete a scan, is typically limited by the speed of the mirror movement as well as the length of moving arm (which affects resolution, resulting in

a time-resolution tradeoff). While this may not seem particularly appealing or important to a graduate student who doesn't have Friday night plans anyway, time saved actually manifests as better SNRs. This is because for a given block of time, more scans can be taken, and generally, the SNR scales with $\sqrt{N}$ scans. The speed advantage is also commonly known as the Fellget advantage.

3. *Resolution advantage (Connes):* Not surprisingly, the ability to resolve in wavenumber space depends on the resolution in position space. Hence, one may ask: how is the movement of the mirror tracked, and when does the digitizer collect a data point to record in the position space interferogram? Typically, a coherent source, such as a helium-neon (HeNe) red laser, also enters the beam path as shown in Figure 2.12. A separate detector (not shown) measures the response from the HeNe as a function of mirror position. Because the HeNe is coherent, as shown in Figure 2.13(a), the response will be periodic with peaks and nulls. Hence, at these specific HeNe nodes (typically null points), the digitizer acquires a point. So, the FTIR spectrometer possesses resolution advantages as its limit is related to the tracking of the mirror position, which in turn depends upon the relatively short-wavelength HeNe tracking laser. This resolution advantage is called the Connes advantage, although in context of this dissertation, it isn't particularly useful as the majority of spectra to be collected are broadband.

2.3.2 Step Scan and Mid-Infrared Photoluminescence

In Subsection 2.3.1, the working principles and advantages of FTIR spectroscopy were described. It was also mentioned that in the mid-infrared (MIR), and especially in context of this dissertation, the throughput (Jacquinot) advantage was most important as

signal to noise ratios (SNRs) in this wavelength range tend to be rather poor. This subsection starts by describing amplitude modulation step scan, a technique which significantly boosts our SNRs even further. We begin with a brief discussion of lock-in amplifiers (LIAs), and then apply the LIA's utility toward MIR photoluminescence (PL).

The lock-in amplifier (LIA) is critical to many techniques employed in this dissertation, as it can significantly boost SNRs. Experiments which use an LIA typically involve signal modulation in an attempt to isolate the signal from detector output noise (which will be discussed in detail in Chapter 5), as shown in the electronic spectrum of a modulated detector in Figure 2.14.

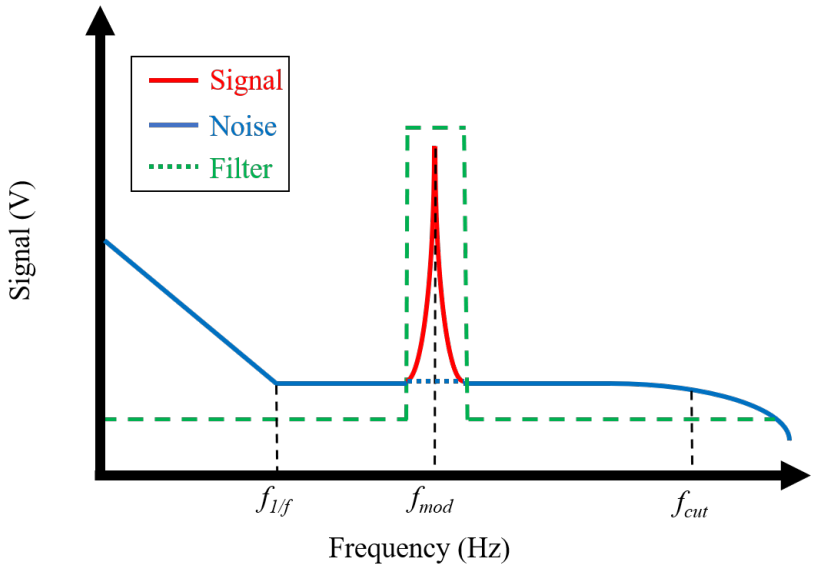

Figure 2.14: Electronic spectrum of detector output in a modulation experiment. The red line denotes the signal at the modulation frequency, f_{mod}, and the blue line denotes the output noise spectra of the detector, with 1/f corner frequency, $f_{1/f}$, and the cutoff frequency, f_{cut}, labeled. The green dashed line represents an ideal filter which can isolate the signal from the noise

For most cases in this dissertation, the signal comes from a detector, which for a periodically

modulated source, can be written as:

$$v_{det}(t) = v_1 \cos(\omega_{mod} t + \phi_{mod}) \tag{2.26}$$

Furthermore, if the signal to be detected is periodically modulated, a reference signal from the source of modulation is also typically available, and can be written as:

$$v_{ref}(t) = v_2 \cos\left(\omega_{ref} t + \phi_{ref}\right) \tag{2.27}$$

Ultimately, the goal is to improve SNR by creating the electronic filter described by the dashed green line in Figure 2.14 to isolate the signal and filter out the noise. To do so, the LIA can be used; in the conceptually simplified LIA, two stages/components exist: a mixer and a low-pass filter (LPF). In the first step, the detector signal is mixed with the reference signal, which can be simplified to:

$$v_{mix}(t) = v_{det}(t) \times v_{ref}(t) = v_1 v_2 \cos(\omega_{mod} t + \phi_{mod}) \cos\left(\omega_{ref} t + \phi_{ref}\right)$$

$$= \frac{1}{2} v_1 v_2 \{\cos\left[(\omega_{mod} + \omega_{ref})t + \phi_{mod} + \phi_{ref}\right] + \cos\left[(\omega_{mod} - \omega_{ref})t + \phi_{mod} - \phi_{ref}\right]\} \tag{2.28}$$

In Equation 2.28, the result of the mixing produces both a frequency sum term as well as a difference term. If the output of the mixer is then fed into a low pass filter (LPF), the sum term will drop out, and the output will be:

$$v_{out}(t) = \frac{1}{2} v_1 v_2 \cos\left[(\omega_{mod} - \omega_{ref})t + \phi_{mod} - \phi_{ref}\right] \tag{2.29}$$

From Equation 2.29, it becomes apparent that the output voltage is nonzero only for a bandwidth around $\omega_{mod} = \omega_{ref}$, depending upon the bandwidth of the LPF. Hence, the filter in Figure 2.14 can be realized: the passband of the filter is at the modulation frequency with a bandwidth, and noise is filtered out at all other frequencies, thus improving the SNR. Consequently, the LIA is used in nearly every experiment in this dissertation, including experiments done with the FTIR spectrometer.

In traditional FTIR spectroscopy, such as described in the Subsection 2.3.1, the detector sees an optical signal that is modulated by the movement of the mirror, related (though not exactly equal) to the chosen scanner velocity. This configuration is considered normal operation, though oftentimes it can also be called "rapid scan", since the mirror moves back and forth quickly, allowing for hundreds of scans to be taken in minutes. However, in step scan mode, the mirror instead takes a step and then waits, during which the signal from the detector is sent to a LIA, integrated within the LIA time constant (which is related to the bandwidth of the LIA's LPF), and then sent back to the FTIR spectrometer's digitizer. A stabilization delay is set in the software, and is usually set to be three times the time constant of the LIA. Once the time has passed, the mirror continues to the next position step and starts building the interferogram. The clear advantage of step scan is an improvement in SNR afforded by the LIA, although because stabilization times have to be set appropriately, the scans can take more time.

Because emission from narrow bandgap materials tends to be very poor as a result of short nonradiative recombination times (especially at non-cryogenic temperatures), step

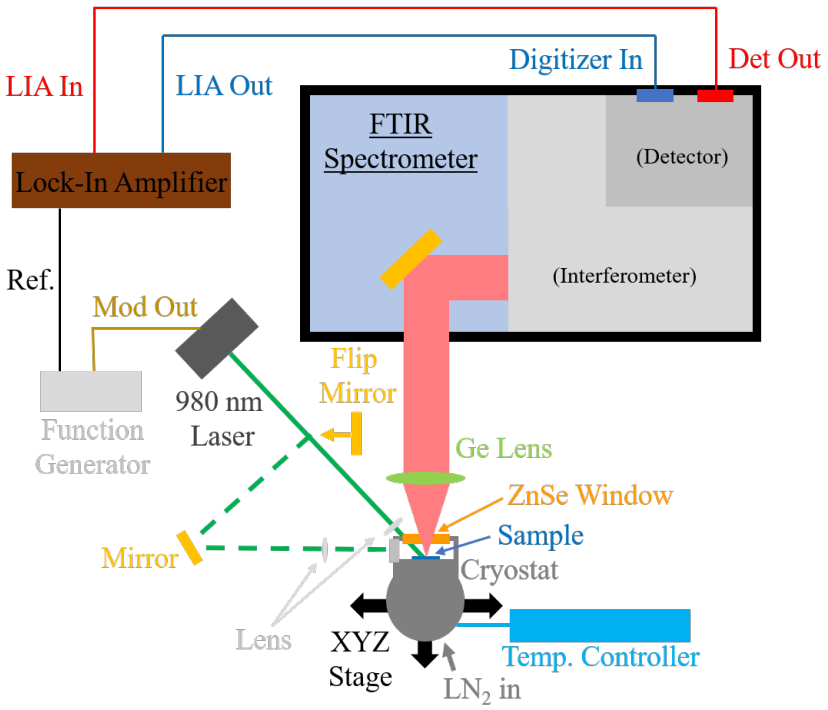

Figure 2.15: Schematic of the temperature dependent photoluminescence (PL) setup in the Wasserman lab built for the work in this dissertation. Both the regular PL (normal collection) and 45 degree/edge emission setups (activated with flip mirror) are shown

scan FTIR spectroscopy is an excellent methodology to use with photoluminescence (PL) setups in the mid-IR. Figure 2.15 shows a PL setup made in the Wasserman lab for the purposes of this dissertation. Samples are housed in a standing cryostat with a liquid nitrogen (LN_2) drip feeding from the top, and a temperature controller connected allowing for precise control of the cold-finger between 77 and 325 Kelvin. A 980 nm laser diode emitting 70 mW of power is modulated by a function generator at 10 kHz with a 50 % duty cycle. The incident beam, which comes in at an angle, is then focused upon the sample within the cryostat. For most cases, normal emission is collected from the sample by a three inch germanium lens and sent to the back port of the FTIR spectrometer. However, a

flip mirror is also easily added to the beam path of the laser, allowing for the laser beam to arrive from the left of the cryo (dashed green lines in Figure 2.15). Then, if the sample is rotated inside the cryo, instead of normal emission, either 45 degree or edge emisssion can be collected. Once the emission traverses the interferometer, it is focused upon the internal mercury cadmium telluride (MCT) detector. The output of the detector is then sent to the input of an LIA as v_{det}, synchronized to the reference from the function generator, which serves as v_{ref}. The output of the LIA is sent back to the FTIR spectrometer for digitization.

2.3.3 Time-Resolved Photoluminescence

This subsection describes the Wasserman group lab's time-resolved photoluminescence (TRPL) setup, used to characterize the carrier lifetime of an emitting material. In this section, only a description of the setup itself is provided. Details of the technique's pros/cons are given in Chapter 4.

In TRPL, a sample that can emit light is excited by an above band-gap pulsed laser source. The laser generates electron hole pairs (EHPs), and by radiative recombination of the EHPs, the sample emits light. This light is then collected via optics and sent to a high-speed detector. The detector signal is then sent to an oscilloscope which then allows for a recording of the transient decay. Figure 2.16 shows a schematic of the TRPL setup built for and used in this dissertation. Samples are housed in a microscope cryostat with a liquid nitrogen (LN_2) drip feed. A Nd:YAG 1064 nm Q-switched laser with a ~1 ns pulse width, 10 kHz repetition rate, and an energy of ~6.8 μJ per pulse is used as the excitation source. By using reflective neutral density (ND) filters, the excitation intensity from the source is controlled; note that the ND filter is placed at a slight angle with respect

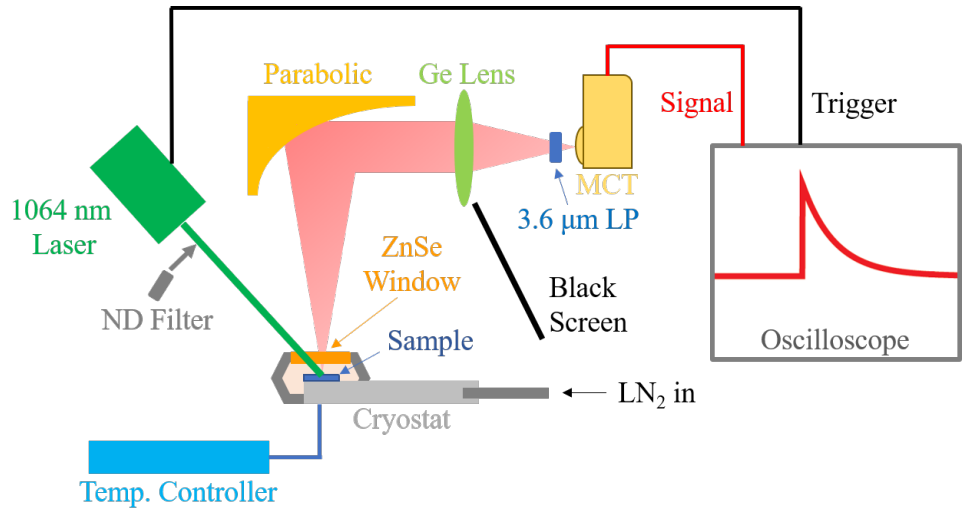

Figure 2.16: Schematic of the temperature dependent time-resolved photoluminescence (TRPL) setup in the Wasserman lab built for the work in this dissertation

to the laser to avoid back-reflection. Since the laser is placed at an angle with respect to the sample, a black screen is placed to block and prevent any of the reflected beam from blinding the detector. Emission from the sample is collimated by a six inch parabolic mirror. A three inch germanium lens focuses the emission (while simultaneously absorbing/blocking any scattered laser light) onto a high-speed, (approximately 4-5 ns rise time) LN_2-cooled mercury cadmium telluride (MCT) detector. In many cases, it is necessary to filter out light from an emitting substrate that makes it through the germanium (such as indium arsenide, or gallium antimonide). To do so, we use a 3.6 μm long pass filter; furthermore, this filter serves as an additional component which blocks any blinding laser light. The signal from the MCT is sent to an averaging oscilloscope triggered to the laser repetition rate.

Chapter 3

Microwave Mapping by Optically Induced Conductance (MMOIC)

This chapter reviews the microwave mapping by optically induced conductance (MMOIC) technique developed as a part of this dissertation. This work has been published in *IEEE Photonics Technology Letters* as "Optical Mapping of RF Field Profiles in Resonant Microwave Circuits". The authors listed on the paper are: Sukrith Dev, Runyu Liu, Jeffery Allen, Monica Allen, Brett Wenner, and Daniel Wasserman [12]; as such, this chapter serves as an extension of the paper, so portions of the text and figures in this chapter have been either taken or adapted from the published paper.

Here we introduce a microwave electric field mapping technique, which we dub microwave mapping by optically induced conductance (MMOIC). In the MMOIC technique, microwave circuits which are fabricated on semiconductor substrates are optically pumped with light above the bandgap while driven with a continuous wave (CW) RF source. The optical modulation of the RF carrier is shown to be proportional to the RF electric field. By spatially rastering the optical beam, a response per position, and thus a map of the field, is obtained. Furthermore, both analytic and FEM modeling provide further insight as to the effects of optically modulating a microwave circuit.

3.1 Traditional Field Mapping Techniques

The incredible improvement in computational strength has lent itself well to simulation methods such as the finite element method (FEM), discussed briefly in Chapter 2. FEM has aided in the design of semiconductor microwave devices, especially passive components such as filters, oscillators, waveguides, and read-out components. Despite this, experimental characterization of field distributions is typically more costly, time-consuming, or low-resolution. For example, in traditional field-mapping methods, a microwave near-field scanning probe (such as an open coaxial cable) is scanned above the sample surface [55][56][57]. In one configuration, the reflection of an RF signal on the cable allows for a readout of the surface conductivity (note that this is similar to a passive version of the time-resolved microwave reflection technique described in Chapter 4). Alternatively, the circuit device under test (DUT) is driven with a microwave signal, and the coax probe picks up and maps the scattered evanescent fields across the circuit. It is worth mentioning that improvements in spatial resolution have been achieved by replacing the coaxial cable with an ultra-subwavelength parallel strip transmission line or alternatively, a scanning tunneling microscopy (STM) tip [58][59][10] (shown in Figure 3.1), allowing for micron-scale resolution measurements of material conductivity. However, the significant length scale mismatch between probe tips and the free-space RF wavelengths (which can be on the order of mm to cm) results in potentially poor SNR for mapping of active circuits due to weak coupling of fields. Because of this, any measurements of field profiles are more difficult with these techniques, especially in structures or spatial/spectral regions of weak fields.

Hence, mapping of RF field profiles using an optical probe is of significant interest as it addresses the resolution and sensitivity issues faced by aforementioned techniques. A

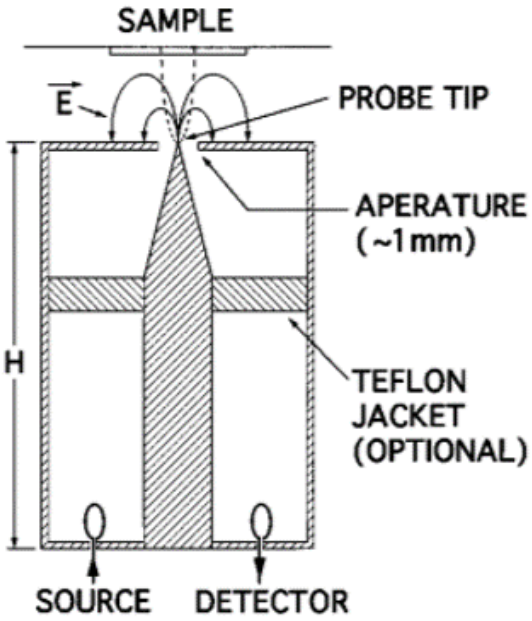

Figure 3.1: Schematic of the microwave tip based on scanning tunneling microscopy (STM), used for mapping evanescent microwave fields with a high spatial resolution, typically on the order of microns. Taken and adapted from [10]

focused laser beam (typically on the order of microns) is significantly subwavelength relative to RF/microwave fields; thus, optical modulation of the RF circuit with a focused laser excitation allows for sub-wavelength (at RF wavelengths) probing of the RF circuit. Such an approach provides the opportunity for improved spatial resolution in the characterization of RF circuitry. To this end, another existing field mapping technique utilizing the electro-optic (EO) effect [15] in crystals is employed. In this technique, a laser emitting <ps pulses is reflected from the DUT which incorporates an EO crystal. The polarization shift of the optical probe beam due to the RF field-induced birefringence is used to extract the amplitude and direction of the RF field at the laser spot. Typically, the technique is categorized as

either an internal or external technique. In the internal EO technique, the DUT is fabricated on a substrate which inherently possesses an EO effect (such as semi-insulating gallium arsenide). However, for DUTs that do not have an EO effect, or alternatively, for mapping 3D-fields above the DUT, an external EO crystal is placed above the DUT, as seen in Figure 3.2[11]. While the use of the external crystal allows for measurement of more diverse DUTs, it could be argued that the use of an external crystal loads the DUT and therefore can modify the fields intended to be measured. Furthermore, because the polarization shift of the probe beam accumulates over the length of the beam's optical path through the RF field in the EO material, spatial resolution on the optical axis can be limited.

Despite this, the EO RF field mapping technique can be quite powerful as it allows for high resolution, 3D measurements of the amplitude and phase of the RF field. However, as can be seen in Figure 3.2, it's clear that this technique requires expensive equipment such as ultra-fast lasers and spectrum analyzers. As a part of my PhD, we were interested in the modulation of RF circuits using infrared light. To achieve maximum modulation, it was necessary to qualitatively determine the spatial distribution of RF fields among different RF structures. Hence, we didn't necessarily need 3D profiles of the absolute RF fields, but rather just a desired a high spatial resolution, non-invasive, low-cost, experimental method for mapping relative electric field strength in an RF circuit. As an alternative method to mapping the relative electric fields, we present the MMOIC technique. Like the EO sampling technique, the MMOIC technique uses an optically induced effect from an ultra subwavelength focused laser, and thus offers spatial resolution orders of magnitude below the free-space wavelength of the RF signals in our circuits. We present a proof of principle for the MMOIC technique, and discuss the advantages and challenges of this approach.

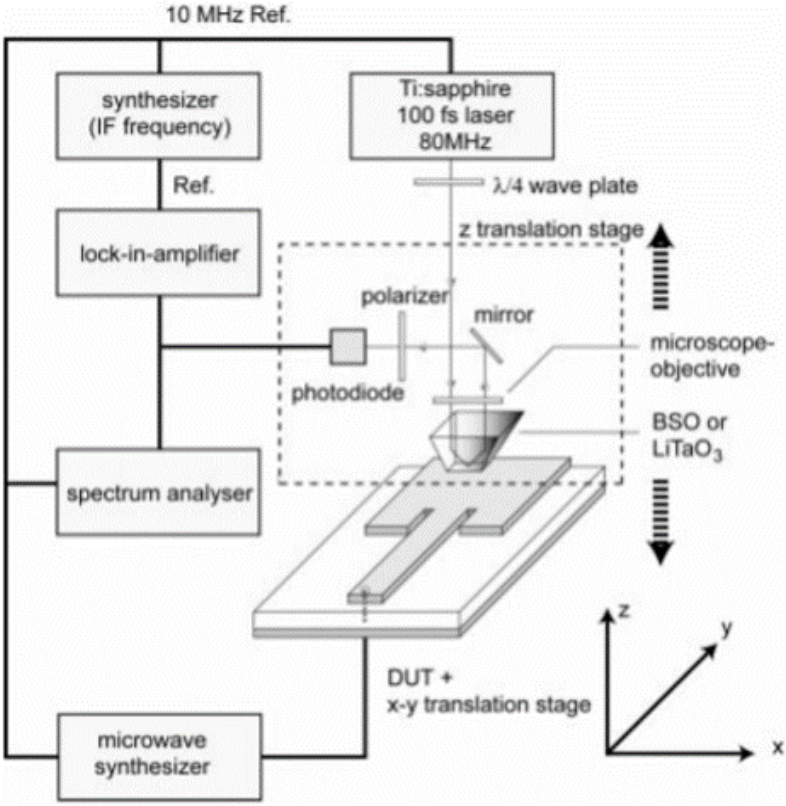

Figure 3.2: Schematic of the electro-optic (EO) field mapping technique utilizing an external crystal. Taken and adapted from [11]

Potential improvements to the technique are presented and discussed. Experimental data is compared to field simulations and transmission line models, with excellent agreement, suggesting the potential utility of MMOIC for RF circuit characterization.

3.2 Overview of the MMOIC Technique

3.2.1 Setup and Operating Principles

A schematic of the MMOIC technique is given in Figure 3.3(a). The DUT is driven by a continuous wave (CW) RF source at a single frequency, while an electrically modulated laser with a photon energy above the bandgap of the DUT substrate optically generates electron-hole pairs (EHPs), altering the local conductivity and modulating the RF transmission, or S_{21} parameter, as seen in Figure 3.3(d). This optically induced conductivity modulation can be read out on the RF carrier via a Schottky diode detector and lock-in amplifier (LIA) which is referenced to the laser modulation. By placing the laser on an electronic motor XY stage, using a simple LabView program, a response as a function of spatial position can be collected and stitched together, which ultimately forms a spatial (and RF spectral) map of the effect of the optical pulses on the RF circuit.

A schematic of our DUT is shown in Figure 3.3(b); ground-signal-ground (GSG) probes contact the "horseshoe-like" coplanar pad in which the signal pin makes contact to the the microstrip and the two grounds contact the pad. The sample is placed on a vaccuum chuck to prevent sliding during probing. For these measurements, laser light from a 785 nm laser diode is focused onto the sample using a half-inch diameter, one inch focal length BK7 lens, where the relatively long focal length is needed to safely avoid running into the expensive GSG probes. Although diffraction-limiting optics (for example, diffraction-limited aspheric lenses sold by ThorLabs) could focus the laser spot size better than the BK7 lens, at some point, the spatial resolution will be limited by the diffusion length of carriers generated in the semiconductor rather than the spot size. Nonetheless, using the BK7, the laser was focused to a spot size of approximately 16 μm full-width half-maximum

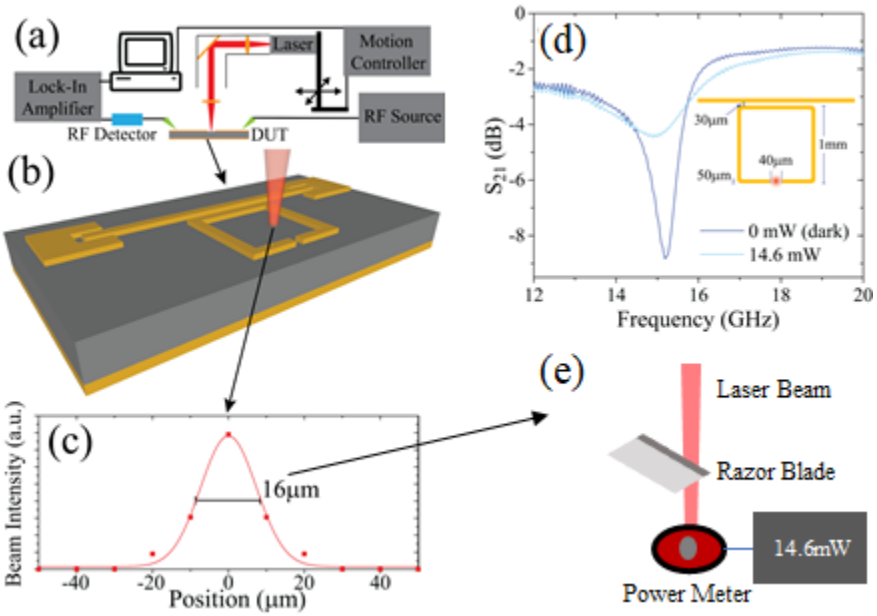

Figure 3.3: Overview of the microwave mapping by optically induced conductance (MMOIC) technique; (a) schematic and operation; (b) overhead view of the device under test (DUT) consisting of split-ring resonators (SRRs) coupled to a microstrip; (c) beam spot size measurement; (d) S_{21} of both a dark and illuminated SRR; (e) schematic of beam spot size measurement method; partially adapted from [12]

(FWHM), as seen in Figure 3.3(c). The spot size was determined by placing a razor blade at the same focus of the DUT over a ThorLabs S302C power meter, as shown in Figure 3.3(e), and then spatially rastering the laser over the razor blade. A power per position point is recorded, which ultimately allows for a Gaussian fit to the beam profile as done in Figure 3.3(c). Here we simply wish to convey an approximate size for the beam; hence, we assume it to be circular and symmetric. However, it should be noted that in Chapters 4 and 5, two-dimensional beam profiles are measured as we desired a more accurate spot size for the techniques and measurements in these chapters.

The 785 nm laser, which outputs approximately 15 mW, is mounted on two Thorlabs

electronic motors stacked orthogonal to each other; a function generator modulates the laser at 50 Hz with a 50% duty cycle. An HP 8341B is used to supply the RF signal, and the transmitted signal is collected by a Pasternack 8013 (10 MHz - 18.5 GHz) Schottky diode detector which is connected to a PAR 5210 LIA. Control of the RF signal frequency allows for mapping of fields at different microwave frequencies, which in this case, is used to map resonant structures on and off resonance. The range of RF frequencies we can map is determined by equipment, specifically, the RF cables (< 26.5 GHz), probes (< 40 GHz), and Schottky diode (< 18.5 GHz). The laser modulation frequency is limited by either the laser driver or the demodulation of our LIA, which in this case is 100 kHz. Scans of our DUT are obtained with 10 μm motor step size with a time delay of 500 ms per point, providing sufficient time for the LIA to integrate the signal. In principle, the scan time could be significantly less by reducing the time constant (and hence, the time delay) of the LIA, although doing so would be at the cost of signal to noise ratio (SNR), which may not allow for mapping of weak signals.

3.2.2 Fabrication of Split Ring Resonators

In this work, we investigate a class of RF circuitry consisting of a split-ring resonator (SRR) capacitively coupled to a microstrip busline, as seen in Figure 3.3(b). The fabrication of these devices is described in Figure 3.4. As mentioned, in this chapter, we fabricated circuits on semi-insulating (note that the choice of substrate must ideally be as insulating as possible to help reduce dielectric losses of the microstrip and resonant circuit) gallium arsenide (SI GaAs), though in Chapter 4 and 5 which use different substrates, the overall fabrication process is still generally similar. Using an electron-beam evaporator, 10 nm

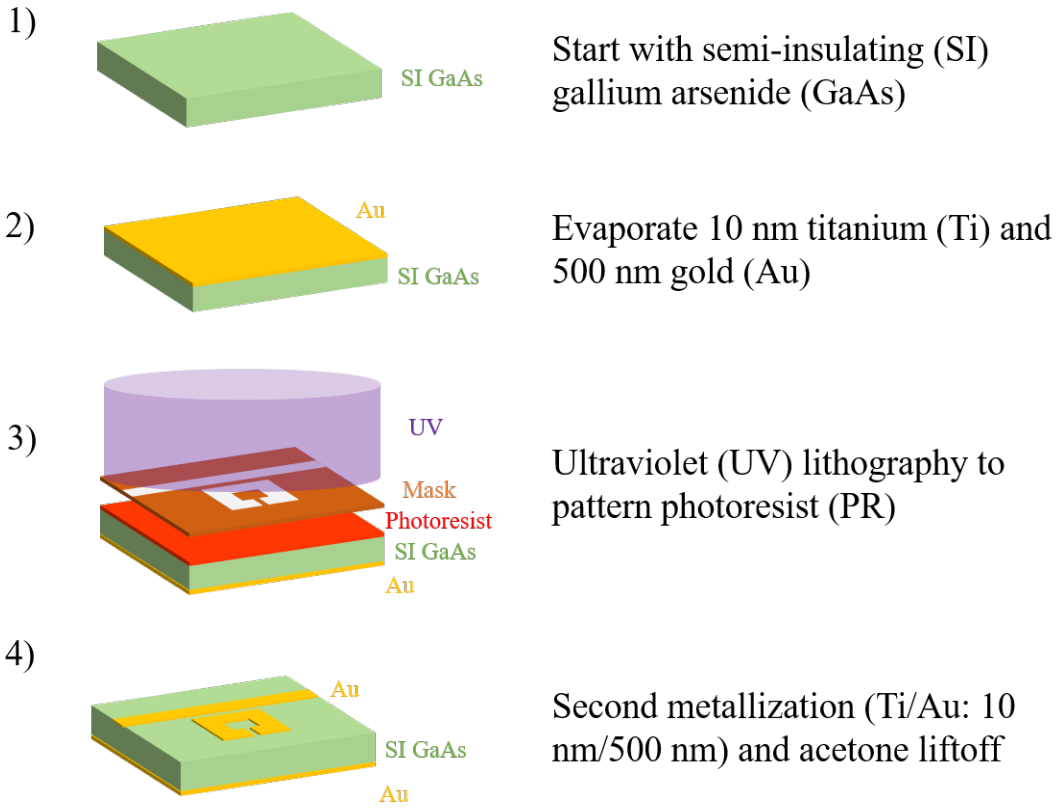

Figure 3.4: Fabrication process for split-ring resonator circuits, with further details/specifics provided in Appendix B. Note that the coplanar "horseshoe" probe contact pad seen in Figure 3.3(b) is not shown in the diagram of step 4) for simplicity

of titanium (Ti) followed by 500 nm of gold (Au) is evaporated on the backside of the SI GaAs to serve as the ground plane. Photoresist is spun on the front side, and standard UV photolithography patterns the resist. Finally, a second deposition (also 10 nm of Ti followed by 500 nm of Au) and liftoff in acetone forms the final resonant microwave circuit. For further details/specifics on the fabrication, please refer to Appendix B.

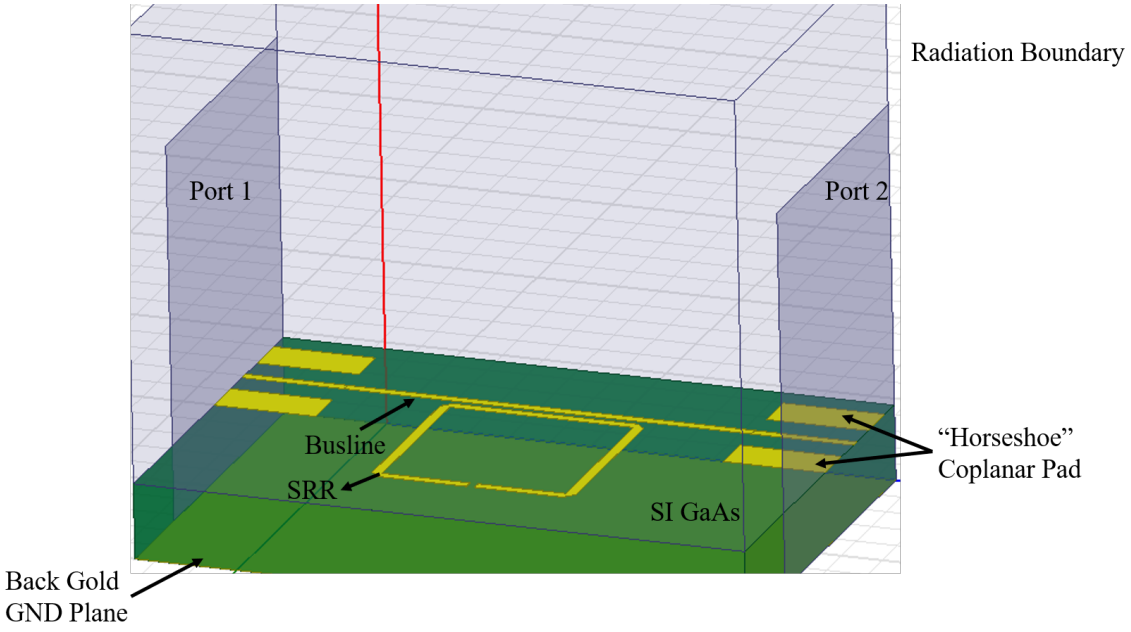

Figure 3.5: Overhead view of the HFSS simulation drawing

3.3 Modeling

To support any experimental data taken using the MMOIC, two modeling techniques were utilized. The first was a commercial finite element method (FEM) software, Ansys HFSS, and was used to compare field distributions between the experimental data and computation. Secondly, an analytical lumped element model of our circuit (written in Wolfram Mathematica) was used to gain further insight into the effects of optically induced conductance. In this section, the two modeling methods are described. Results from the simulations are shown in Section 3.4 together with the experimental data for easier comparison.

3.3.1 HFSS Simulations

Figure 3.5 shows an overhead view of the HFSS simulation. A radiation boundary condition covers the circuit and also extends into the air above the microstrip. The substrate is gallium arsenide and is modeled with the software library's RF permittivity of 12.8 and a loss tangent of 0.004. The thickness of the substrate is 0.375 microns, which is comparable to what was measured for the fabricated substrate thickness using a Mitutoyo thickness monitor. Both the ground plane and microstrip/SRR lines are modeled as 3D finite rectangular pieces of gold and use the software's material library for gold. To approximate the effect of the coplanar horseshoe pad seen in Figure 3.3(b), the two ends of the microstrip are each sandwiched between two metal pieces such that the ends mimic a grounded coplanar waveguide. The dimensions of this coplanar waveguide resemble the dimensions of the horseshoe pad. Wave ports are used on both ends, with integration lines drawn between the microstrip and ground plane on each side.

Because we will utilize a lumped element model in Subsection 3.3.2, we needed to determine the coupling mechanism between the microstrip busline and the SRR. Our HFSS simulations allowed us to investigate the coupling mechanism between our busline and the SRR structure. While in the literature, the coupling in similar structures is sometimes described as inductive [60] and other times as capacitive [61][62], we ultimately used the phase relationship between fields on the microstrip and SRR to argue that for our specific configuration, size, and frequency, our SRRs are capacitively coupled. We observed a nonzero divergence in the current on the busline, with a maximum value out of phase with the maximum E-fields on the SRR; thus, we justify the coupling for this structure as capacitive.

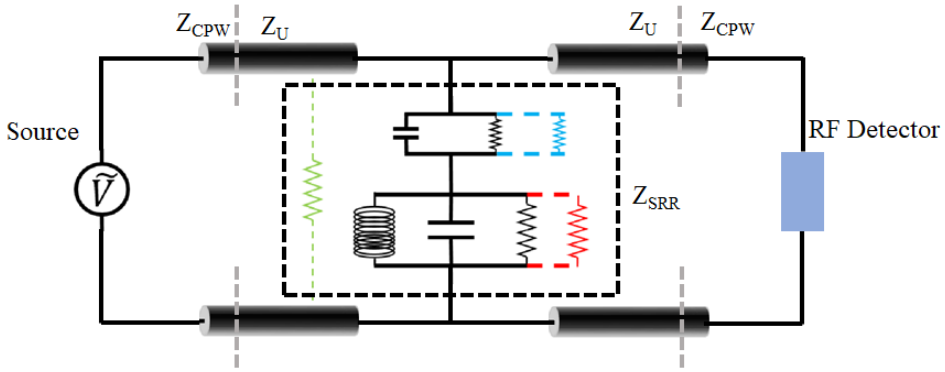

Figure 3.6: Lumped element model for our split-ring resonator (SRR) capacitively coupled to a microstrip busline

3.3.2 Lumped Element Modeling

The lumped element model employed in this chapter for analytical modeling of our system is shown in Figure 3.6. The RF detector is our Schottky diode, and has an impedance of 50 Ω. The black cylinders represent transmission lines, where the horseshoe probe pad is modeled as a grounded coplanar waveguide and is attached to the microstrip. Details on mismatched line modeling is given in Chapter 2; following the methodology outlined in Chapter 2, we can reduce the terminated mismatched line into an effective input impedance, Z_{in1}, as seen in Figure 3.7.

Next, it's clear from Figure 3.7 that Z_{in1} is in parallel with the SRR impedance, Z_{SRR}. To more easily describe the SRR impedance, we can write:

$$Z_{SRR} = (Z_{RLC} + Z_{Coup})||R_{sh} \tag{3.1}$$

Henceforth, the "||" operator denotes a parallel circuit element. So, we can break Z_{SRR} into three components: the impedance of the RLC (Z_{RLC}), the impedance of the coupling

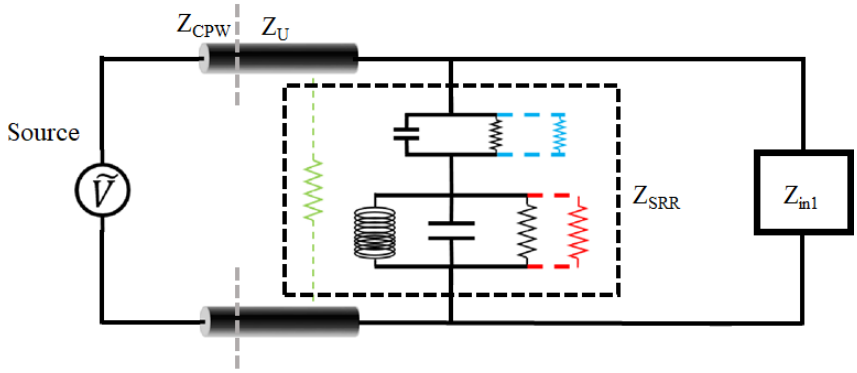

Figure 3.7: First circuit reduction; the terminated mismatched lines from Figure 3.6 on the right hand side is reduced to Z_{in1}

region (Z_{Coup}), and the shunt resistance (R_{sh}) used to describe loss (and optically induced conductance) along the transmission line. From basic circuit theory, the impedance of an inductor (with inductance L) and capacitor (with capacitance C) can be represented in the frequency domain as:

$$Z_L = j\omega L \tag{3.2}$$

$$Z_C = \frac{1}{j\omega C} \tag{3.3}$$

where j represents the imaginary unit, $\sqrt{-1}$, and ω represents the angular frequency in radians per second. Since Z_{RLC} has parallel RLC components, it can be written as:

$$Z_{RLC} = \frac{1}{j\omega C}||j\omega L||R = \frac{\frac{1}{j\omega C}j\omega L}{\frac{1}{j\omega C} + j\omega L}||R = \frac{j\omega L}{1-\omega^2 LC}||R = \frac{j\omega RL}{j\omega L + R(1-\omega^2 LC)} \tag{3.4}$$

And similarly, Z_{Coup} can be represented as:

$$Z_{Coup} = \frac{1}{j\omega C_{Coup}} || R_{Coup} = \frac{R_{Coup}}{1 + j\omega R_{Coup} C_{Coup}} \tag{3.5}$$

Note that the subscript "Coup" is added to both the coupling capacitance and coupling resistance to distinguish them from the capacitance and resistance of the RLC. Next, from Equation 3.1, Z_{RLC} and Z_{Coup} must still be added and then computed in parallel with a shunt resistance, R_{sh}. Then, this entire impedance must be computed in parallel with Z_{in1} of the transmission line. The remainder of the calculations were solved in Mathematica and are thus not shown here for brevity.

In order to demonstrate the link between our experimental mapping of circuit geometry, and the lumped elements used to describe our circuit, we incorporate the effect of localized optical pumping into our TL model. To do so, the change in the local conductivity from the incident light is modeled as a shunt conductance (resistor) positioned at the lumped element corresponding to the position of the incident light. Figure 3.1 shows these resistors, color coded for light incident upon the bus line (green), the coupling gap (blue) and the SRR capacitive gap (red). Note that because the coupling region is shared with the busline, a combination of conductances added to both the coupling resistor and shunt resistor was used for fitting. We can then modify the impedances in the model to account for the optically induced conductances; these modified impedances are denoted with a prime (’):

$$Z'_{RLC} = Z_{RLC} || \frac{1}{G_{RLC}} \tag{3.6}$$

$$Z'_{Coup} = Z_{Coup} || \frac{1}{G_{Coup}} \tag{3.7}$$

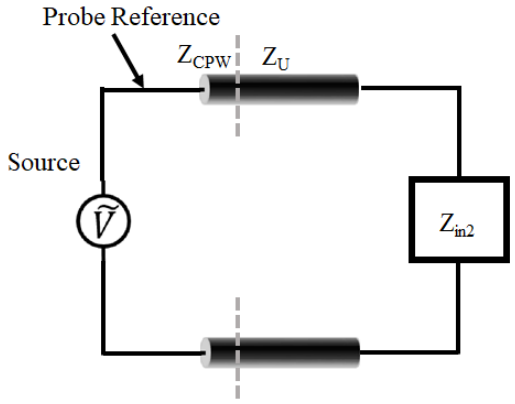

Figure 3.8: Second circuit reduction; the impedance of the SRR is computed in parallel with the Z_{in1} from Figure 3.7

$$R_{sh}^{'} = R_{sh} || \frac{1}{G_{sh}} \tag{3.8}$$

However, because the probe area (beam spot) is much smaller than the physical realization of the lumped elements in the model, the effect of the probe, incident upon the SRR for example, will vary significantly with the probe's position on the SRR. We could model this by allowing the additional photoinduced conductance in our model to vary as a function of the beam's position on the SRR. We then look to relate the magnitude of the modeled shunt conductance vs. probe position on the lumped elements to the strength of the RF field at those positions.

Once Z_{SRR} is computed (or alternatively, $Z_{SRR}^{'}$ if including the optically induced conductance) in parallel with Z_{in1}, the circuit can once again be reduced as a new effective input impedance, $Z_{in2} = Z_{SRR} || Z_{in1}$, as shown in Figure 3.8.

Now, this circuit looks familiar to that of Figure 2.4 in Chapter 2. The same method-

ology from Chapter 2 can be applied to this circuit, with an additional 50 Ω impedance mismatched considered between the probe and pad denoted by the arrow in Figure 3.8. This is because for fitting, we compare to experimental data taken with a vector network analyzer (VNA) which is calibrated to move the reference to the probe tips assuming a 50 Ω impedance at each port. Furthermore, for the actual MMOIC measurement, there is still a 50 Ω impedance to consider from the cables and/or source. However, when using the LIA with the Schottky diode, because the Schottky diode produces an output voltage proportional to the power, once the voltage over the Schottky is solved for, Equation 2.11 should be used to solve for the power.

3.4 Results and Experimental Data

Figure 3.9 shows the experimental (taken with a VNA), HFSS simulated, and Mathematica lumped element-model of dark (no illumination) RF S_{21} spectra for a 1 mm SRR with a 40 μm capacitive gap, coupled to a microstrip busline via a 30 μm coupling gap (Figure 3.3(d)). Both models show excellent agreement with the experimental data.

Figures 3.10(a) and (b) show the HFSS simulated normalized electric field profile at the circuit surface on and off resonance, respectively, for the SRR resonator whose spectrum is shown in Figure 3.3(b). The experimental MMOIC data from the same sample, on and off resonance, is shown in Figure 3.10(c) and (d). Note that the color intensity is scaled differently for positive and negative signals to better observe the weaker negative signals of the experimental data. Qualitatively, the basic field profiles observed in our simulations match nicely with the experimental MMOIC data. As shown in Figure 3.10(c), the strongest spatial position of response is located in the SRR split-gap when driven on

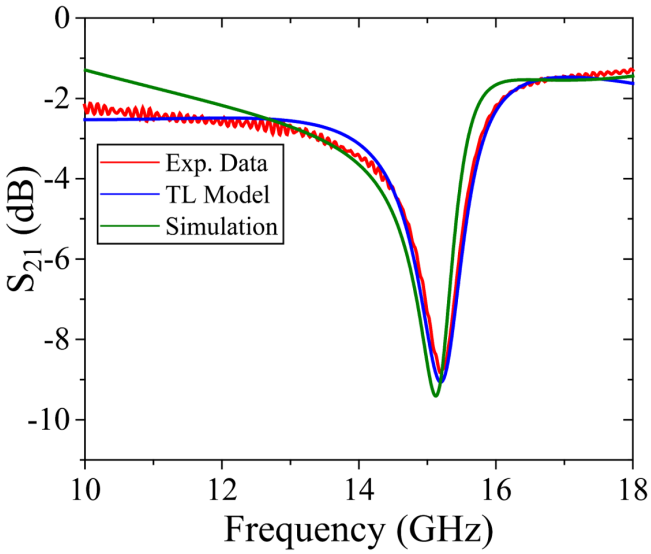

Figure 3.9: Comparison of S_{21} spectra taken with a VNA (red), modeled analytically (Mathematica) via lumped elements and transmission lines (blue), and simulated using HFSS (green)

resonance, which is corroborated by the simulation in Figure 3.10(a). When driven off resonance, no significant buildup of field (and thus response) is observed in the SRR split-gap; instead, the response is predominantly along the microstrip and in the coupling gap, and is now negative in sign.

Despite qualitative agreements, there are differences between the experimentally measured response and simulated fields. First, as one of the limitations, our MMOIC technique cannot induce any significant losses or additional conductivity in metal, preventing any measurement of the field on the lines themselves. The second, and potentially most significant difference between the simulations and the MMOIC experimental results is the sign of the field profiles. In the experimental results, the change in the power delivered to the load is negative for laser light incident on the busline and coupling region for all frequencies, as well as for light incident upon the SRR off resonance. However, when the circuit is

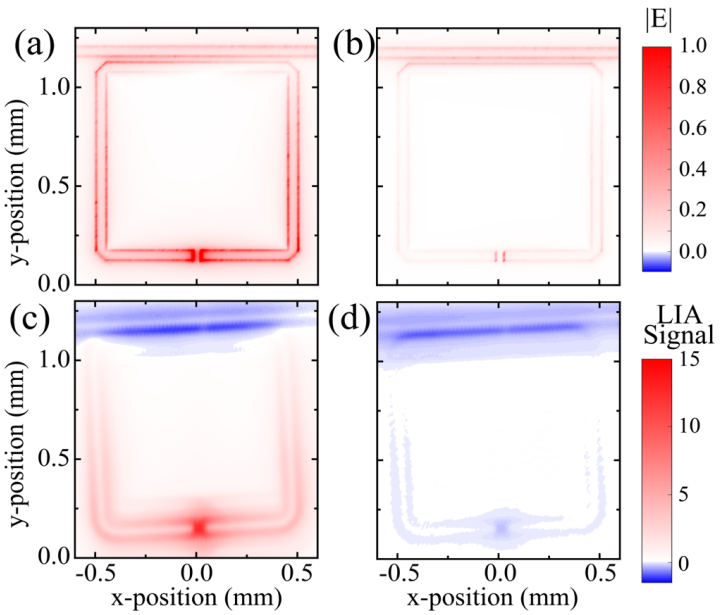

Figure 3.10: HFSS simulated (a, b) normalized electric fields and experimental (c, d) MMOIC contour plots for a square SRR resonator driven (b, d) off and (a, c) on resonance. Simulations performed at (a) f_{on} = 15.24 GHz and (b) f_{off} = 10 GHz. Experimental data taken at (c) f_{on} = 15.2 GHz and (d) f_{off} = 10 GHz

driven on resonance, and optically pumped on the SRR, a positive signal is observed. The simulations, which show |E|, will of course show a positive signal for all frequencies and positions. The existence of both positive and negative signal in our measurements can be understood by considering that our LIA measurement yields an optically induced change in transmitted RF signal, which can be written as:

$$\Delta S_{21} = \Delta S_{11} + \Delta\delta \tag{3.9}$$

Equation 3.9 simply states that the experimentally measured change in transmission, ΔS_{21}, is related to the change in reflection, ΔS_{11} and the change in dissipation, $\Delta\delta$. Because the

SRRs are reflective bandstops, when the optically induced conductance results in a decrease in reflected signal (which is the case when pumping the SRR on resonance), the overall change in transmission is positive. Conversely, when pumping off resonance or spatially away from the SRR, the optically induced conductance results in a combination of increased reflection (which, intuitively, makes sense as in the extreme case of a short shunt to ground, all signal is reflected) and dissipation. To further suggest that the sign is related to the effects an optically induced conductance has on the circuit, we utilize the lumped element model from Subsection 3.3.2 and compare modeled results to experimentally determined results across the full frequency range, as seen in Figure 3.11. We observe reasonable agreement between the experimental and modeled modulation of the frequency-dependent transmitted signal of our circuit for light incident at three different positions: on the busline (green), the coupling gap (blue) and the SRR gap (red).

The variation of the sign of the experimentally measured signal indicates that a purely linear relationship between experimental signal and RF field strength, across the surface of an entire circuit, is not possible. This is because of potential null points (where slight changes in reflection are balanced by slight changes in dissipation), which are typically present in areas where multiple "regions", or lumped elements, starts to overlap. Referring to Figure 3.10(c), we see some null points in the experimental data around the coordinates (-0.5 mm, 1 mm), where the top arm of the SRR starts to overlap with the busline and coupling regions. Pumping the top arm of the SRR, where the fields are weak, results in a slight positive sign in RF transmission (decrease in reflection), but this is balanced by a slight negative sign resulting from pumping near the busline, ultimately yielding an artificial null point. However, for regions that are more well-defined by the lumped elements (such

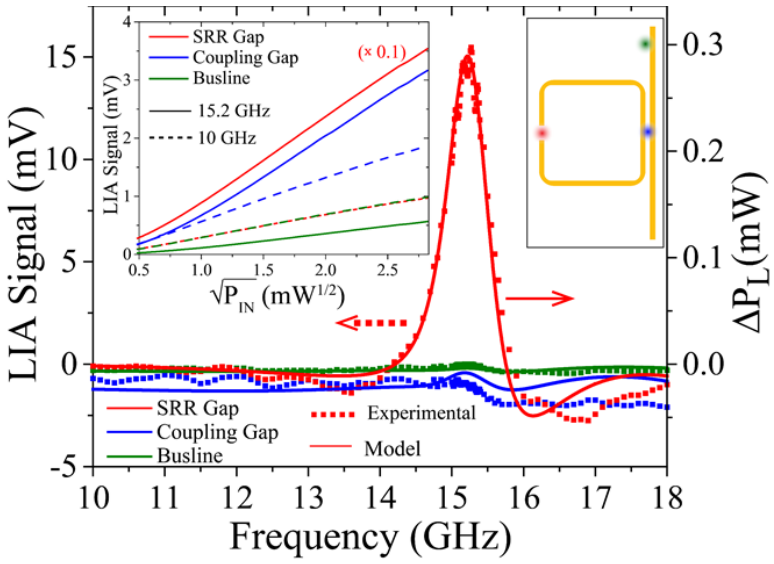

Figure 3.11: Modeled (solid) and experimental (scatter) change in transmitted power as a function of frequency for light incident on busline (green), coupling gap (blue), and SRR gap (red); inset demonstrates linearity of our measured signal with respect to $\sqrt{RFPower}$, suggesting we are measuring a relative electric field

as the lower arms of the SRR, the split gap, or the busline), we see in the inset of Figure 3.11 that the signal is proportional to the square root of RF power, or field. Hence, for a given lumped element, the MMOIC can paint a reasonable picture of the relative fields.

Furthermore, the MMOIC can provide valuable information regarding the electric field distribution for varying circuit geometries; Figure 3.12 shows the experimental MMOIC data on and off resonance for square SRRs with (a) 20 μm and (b) 70 μm gap sizes and (c) a circular SRR with 40 μm gap, respectively. The off-resonance scans are scaled to better observe the entirely negative valued (and weak) MMOIC signal. We see that the MMOIC data allows for the comparison of field distributions even in similar structures, showing, for instance, the strong field confinement possible in the smaller gap structures

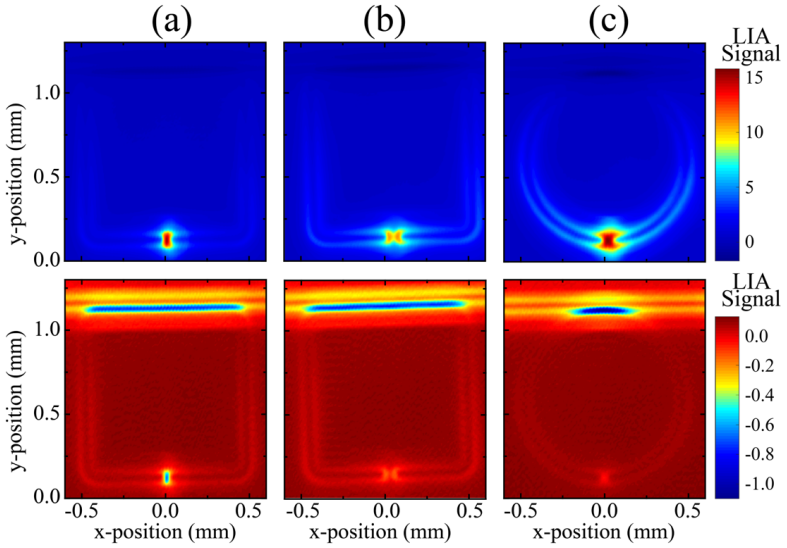

Figure 3.12: Experimental MMOIC plots for different resonator structures (a) 20 μm SRR gap (b) 70 μm SRR gap and (c) circular SRR with 40 μm gap. Top row shows on-resonance scans ((a) f_{on} = 15.76 GHz, (b) f_{on} = 15.4 GHz,(c) f_{on} = 17.9 GHz) while bottom row shows off-resonance data (f_{off} = 10 GHz)

(which is consistent with previous work from our group [63]), or the change in the field distribution in the coupling region of the circular gap, when compared to the square gap structures.

3.5 Suggested Future Work and Summary of Technique

In this section, we will conclude our discussion of the MMOIC technique by suggesting some future work and then ending with a summary of the technique. While the current proof-of-principle demonstration of MMOIC probes only the surface of RF circuits fabricated on semiconducting substrates, future iterations of the technique could be envisioned which allow for a greater range of circuitry to be investigated or, alternatively, three-dimensional (3D) probing of fields in RF circuits. For the former, either spin-on

or low temperature-deposited photoconductive films [64] could be applied to RF circuits on non-photoconductive substrates, providing a photo-excited source of loss on the circuit surface. Following mapping, the photo-responsive film could be removed without harming the circuit itself, assuming the correct choice of film. However, it is worth mentioning that this line of thinking is parallel to that of using an external crystal in the EO mapping technique outlined in Section 3.1. Hence, it is prone (arguably more prone) to similar potential issues; for instance, even if the photoconductive film could be removed without damaging the circuit, its presence may alter the behavior of the fields in the circuit in the first place. Ultimately, the use of an external film would only realize its true utility if we could somehow account for the effects the film may have on the circuit a priori. For possible 3D mapping, two-photon absorption [65] could be utilized to provide not only smaller excitation volumes, but control of the focal spot position both laterally and into the circuit dielectric. Such an approach could offer a 3D image of fields inside of the dielectric substrate of an RF circuit. Practically, this would be straightforward to incorporate into the setup in Figure 3.3(a), with motion control in the z-direction to alter the focus of the laser beam.

In conclusion, we demonstrate a technique (MMOIC) for imaging field profiles in RF circuits. We demonstrate the potential of our approach for field mapping, and discuss the limitations of our technique, as well as potential future improvements. We show that by controlling the position of photoexcited free-carriers on the surface of an RF circuit, we are able to map profiles related to the electric fields in our circuit. Our experimental field maps show excellent agreement with numerical simulations of the electric fields in our test circuits. In addition, we develop a transmission line model of our system,

which matches our experimental spectral results, and offers insight into the relationship between our experimental signal and the field within the distributed realizations of lumped circuit elements. We demonstrate here, as proof of principle, MMOIC on SRR structures capacitively coupled to microstrip buslines, though our technique can be applied to a range of RF structures. MMOIC provides a comparably cost-effective, high-sensitivity, non-destructive approach to experimentally mapping the fields in RF circuits, and offers a potential tool for the characterization and better understanding of a range of RF electronic and optoelectronic systems.

Chapter 4

The Micro-Scale Time-Resolved Microwave Resonator Response (μ-TRMRR) Technique

Here we present the second characterization technique developed as part of this dissertation: micro-scale time-resolved microwave resonator response (μ-TRMRR). It should be noted that this work has been published in *Nature Communications* as "Measurement of carrier lifetime in micron-scaled materials using resonant microwave circuits" [66]. The authors listed on the paper are: Sukrith Dev, Yinan Wang, Kyounghwan Kim, Marziyeh Zamiri, Clark Kadlec, Michael Goldflam, Samuel Hawkins, Eric Shaner, Jin Kim, Sanjay Krishna, Monica Allen, Jeffery Allen, Emanuel Tutuc, and Daniel Wasserman. Portions of the text and figures have been taken or adapted from the published work. However, some of the work towards the end of this chapter has not been peer-reviewed or published yet. Specifically, we demonstrate the effectiveness of the presented technique on WS_2 samples as well as short-lifetime, narrow bandgap semiconductor material. For the latter, only one plot will be shown to prove the time-resolution of our technique. The remainder of the high-speed work has been continued by my labmate Yinan Wang and will be fully described in future publications and his PhD dissertation.

The measurement of minority carrier lifetimes is vital to determining the material quality and operational bandwidth of a broad range of optoelectronic devices. Typically,

these measurements are made by recording the temporal decay of a carrier-concentration-dependent material property following pulsed optical excitation. Such approaches require some combination of efficient emission from the material under test, specialized collection optics, large sample areas, spatially uniform excitation, and/or the fabrication of ohmic contacts, depending on the technique utilized. In contrast, here we introduce a technique which provides electrical readout of minority carrier lifetimes using a passive microwave resonator circuit. We demonstrate > 10^5 improvement in sensitivity, compared to traditional photoemission decay experiments, and the ability to measure carrier dynamics in micron-scale volumes, much smaller than is possible with other techniques. The approach presented is applicable to a wide range of 2D, micro-, or nano-scaled materials, as well as weak emitters or non-radiative materials. As a proof of principle, we also demonstrate a lifetime measurement made on WS_2 as well as a high-speed material to demonstrate sub-nanosecond time resolution of the technique.

4.1 Background

In this section, a very brief overview of some common carrier lifetime (defined as the average time a generated free carrier remains excited prior to recombination) measurement techniques is given. The discussion of the underlying theory of minority carrier lifetimes is common to many textbooks, such as S.L. Chuang's "Physics of Photonic Devices" [67]; thus, for further reading on this subject, I would recommend both the textbook and the PhD dissertation of Benjamin Olson (former member of the Boggess group at the University of Iowa). Similarly, it should be noted that while this chapter covers several lifetime measurement techniques such as photoconductive decay (PCD), time-resolved microwave

reflectance (TMR), time-resolved photoluminescence (TRPL), as well as the novel presented technique, not all techniques that exist have been considered, such as time-resolved pump-probe transmission measurements.

4.1.1 Common Lifetime Measurement Techniques

Traditionally, direct electrical measurements of minority carrier lifetimes are made using direct current (DC) photoconductive decay (PCD) measurements [68][69]. In PCD, non-blocking ohmic contacts are made to the sample under test, and following pulsed optical modulation, a transient of the sample's DC conductivity is measured, from which a carrier lifetime can be extracted. To illustrate this, consider the very simple PCD setup in Figure 4.1. A DC bias is applied across the semiconductor material under test (MUT) and an output load resistor. Prior to optical excitation, some amount of voltage divides over the load as a baseline voltage signal. Once a pulsed excitation generates electron-hole pairs (EHPs), the conductivity of the MUT changes, resulting in a change in voltage division. As the EHPs start recombining, the output voltage on the load appropriately decays.

While PCD is an effective technique and can even be applied to small (micron-scale) materials, the approach requires fabrication of ohmic contacts to the material under test, and thus increased time and expense associated with the contact patterning and metal deposition. Furthermore, the processes for contact formation can vary depending on the MUT and may not be feasible for materials or structures such as polymers, organic dyes, nanowires, or micron- or nano-scale 2D materials. Hence, contact-free lifetime techniques such as TRPL and TMR have gained significant popularity. In TRPL, a short laser pulse optically excites a light-emitting material, and the resulting photoluminescence (PL) is then collected as a

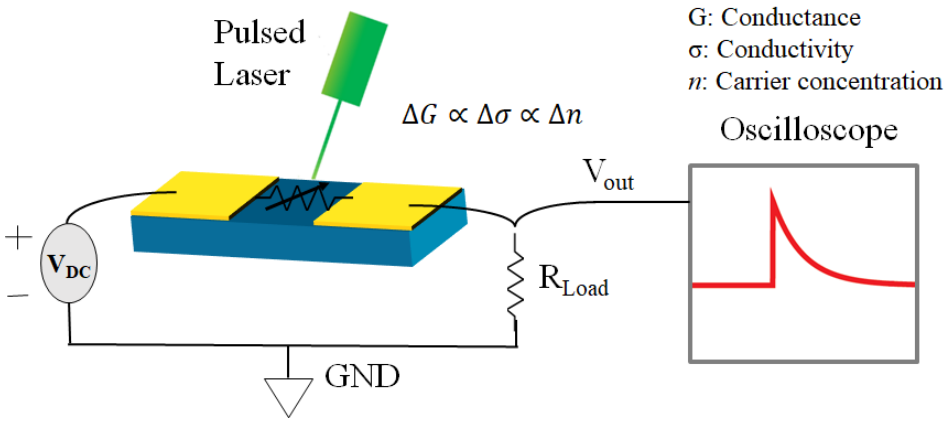

Figure 4.1: Schematic of a basic photoconductive decay (PCD) setup

function of time; carrier lifetimes are then extracted from the temporal decay of the emitted PL [70]. However, in addition to the pulsed laser, TRPL also requires collection optics and a detector that have both been tailored to the wavelength of light emitted by the sample. Hence, oftentimes entirely different optics and photodetectors are required for samples emitting in different regions of the electromagnetic spectrum. In addition, TRPL often requires trade-offs in the choice of detectors, balancing detector sensitivity (allowing for measurement of weakly-emitting or small samples) and detector response times (allowing for measurement of shorter carrier lifetimes), with more sensitive detection almost always accompanied by poorer time resolution. Note that in this chapter, we will compare our proposed technique to the TRPL setup described in Chapter 2.

The non-invasive, contact-free analogue to PCD is time-resolved microwave reflectance (TMR), which records the time evolution of the microwave reflection from a sample following optical excitation, essentially probing a change in the sample's radio frequency (RF) conductivity [71][72]. An example TMR setup is shown in Figure 4.2(b); a

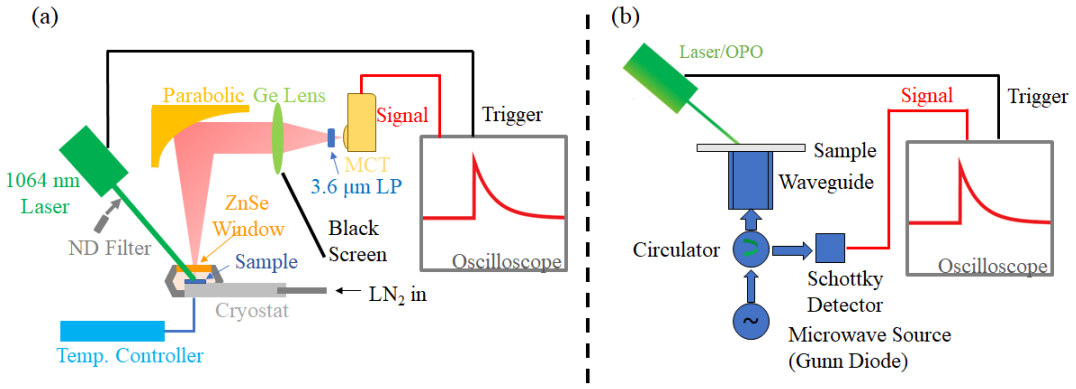

Figure 4.2: Two popular contact-free carrier lifetime measurement techniques: (a) time-resolved photoluminescence (TRPL) as described in chapter two; (b) example of a time-resolved microwave reflectance (TMR) setup

free-space microwave source, typically a Gunn diode, emits an RF signal which is incident upon a sample via a circulator and waveguide. Optical excitation is incident upon the sample and ideally spatially overlaps with the microwave radiation. The excitation and then the subsequent recombination of the optically generated EHPs modulates the conductivity of the semiconductor material, which in turn modulates the RF reflectivity of the surface. The incident microwave signal's reflection thus changes as a function of minority carrier concentration, and is measured by a Schottky diode after passing through the circulator. In this manner, the optical modulation (and therefore the transient decay of the photoexcited carriers) can be extracted. Compared to TRPL, TMR has the advantage of improved sensitivity; furthermore, because it is the photoconductivity which is probed, the sample does not need to emit light, and so there is no need for wavelength-tailored collection optics or a high-speed optical detector. While TMR is an excellent technique for measuring large area samples, for pixel-sized samples, the mismatch between the large RF probe and the micron-scale sample area will significantly decrease the TMR signal to noise ratio (SNR)

as only a small fraction of the reflected RF signal is modulated by the change in the micro-scale sample's carrier concentration. Similar difficulties would be encountered for TMR measurements of photoexcited carriers in 2D materials, as exfoliation processes typically result in micron-scale flakes of 2D material [73].

However, if instead of using free-space microwave probes, one was able to confine the microwave signal to small volumes (on the order of the sample size), one would be able to effectively characterize the time response of micron-scale materials without the requirement of ohmic contact to sample. In Chapter 3, the results from the microwave mapping by optically induced conductance (MMOIC) technique, specifically the data presented in Figures 3.10 and 3.12, suggested that we can use coupled Ku band (defined here as 12-18 GHz) split-ring resonators (SRRs) to concentrate microwave fields. Specifically, if we drive the SRR circuit on resonance, we build up and confine microwave fields in the capacitive split-gap of the lower arm of the SRR. Here we seek to place a micron-scale semiconductor pixel within the split-gap of the SRR and effectively apply the advantages of TMR toward small material volumes.

4.2 Optical Characterization of InAsSb Pixels

Prior to describing our lifetime characterization technique, we will first describe the material system we characterized as a proof of principle. Specifically, we measure the photoexcited carrier lifetimes in 24 μm $\times$ 24 μm pixels of the narrow bandgap III-V material indium arsenide antimonide (InAsSb), which is of practical interest for mid-wave infrared (MWIR) detector applications [74][75][76][77].

4.2.1 Fabrication of InAsSb Pixels

A brief overview of the grown layer structure of the bulk material as well as the fabrication of the InAsSb pixels from bulk material is given in Figure 4.3. Although our group has developed a process for pixelation, the pixels used in this chapter and those used in Chapter 5 were fabricated and provided to us by Marziyeh Zamiri, a former member of Prof. Sanjay Krishna's group, using bulk material grown by Jin Kim and Samuel Hawkins at Sandia National Labs. The bulk material consists of 1 μm thick unintentionally doped (UID) InAsSb grown on 250 nm of aluminum arsenide antimonide (AlAsSb), both lattice matched to a gallium antimonide (GaSb) substrate. Hall effect measurements determined the carrier concentration to be $2.11 \times 10^{16} cm^{-3}$ at 77 K and $2.4 \times 10^{17} cm^{-3}$ at 300 K, although it should be noted that the Hall measurement could overestimate the true carrier concentration [78].

To fabricate the pixels from the bulk material, a standard lithography and dry etch process forms the pixels. Next, dilute acid etches the AlAsSb etch release layer, which undercuts the InAsSb pixels. This allows for a PDMS stamp to be used to rip pixels off the original GaSb host substrate and if desired, transfer to a new substrate such as thermal release tape. An overview of the process is given in Figure 4.3, though details of the process are described in [79].

4.2.2 Photoluminescence and Time-Resolved Photoluminescence

Figure 4.4 shows both the temperature-dependent PL and TRPL from bulk, as-grown InAsSb and an array of InAsSb pixels transferred to thermal release tape, as described in the previous section. Using the PL setup described in chapter two, strong mid-wave infrared

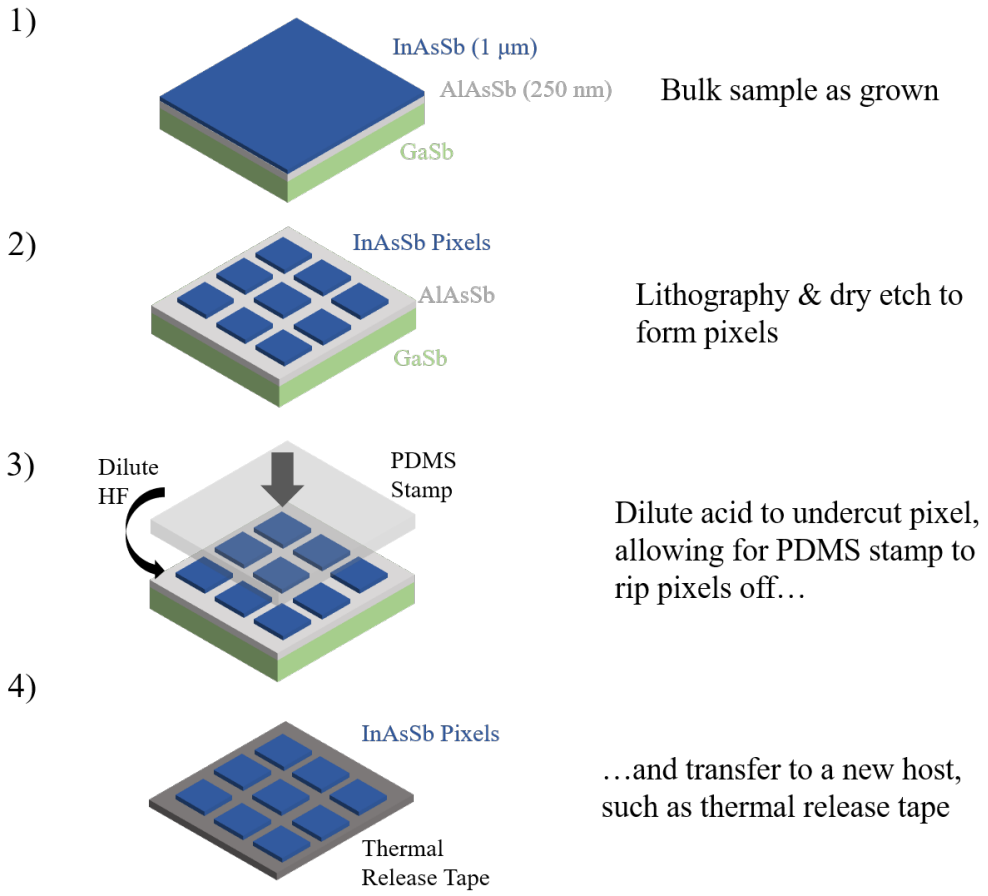

Figure 4.3: Fabrication process for InAsSb pixels made from bulk material grown on top of a sacrificial etch release

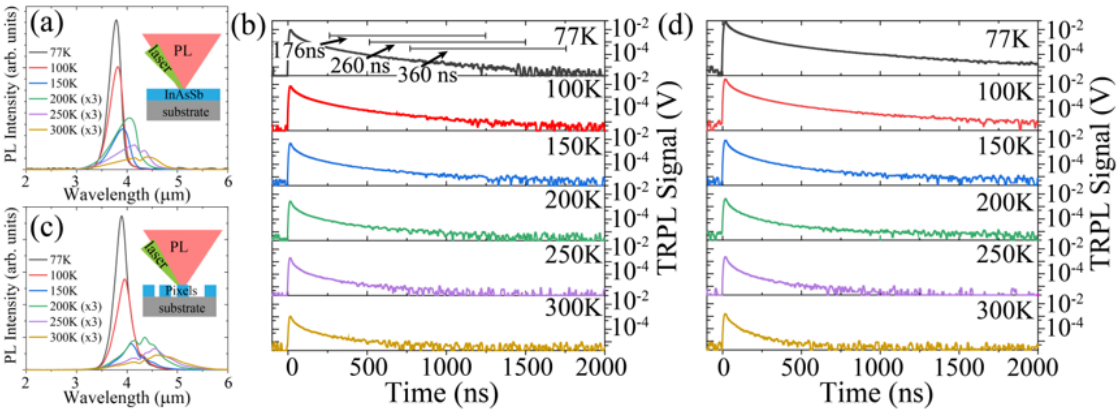

Figure 4.4: Photoluminescence spectra of the (a) bulk, as-grown InAsSb structure in Figure 4.3 step 1) and (b) fabricated cluster of pixels shown in Figure 4.3 step 4); time-resolved photoluminescence of (c) bulk, as-grown structure and (d) pixel cluster

PL is observed from both the bulk as-grown and pixel array of the narrow-bandgap InAsSb, particularly at low temperature; furthermore, as the temperature increases, the PL intensity decreases (from increased nonradiative effects) and red shifts (from a decrease in the InAsSb bandgap). Despite the decrease in intensity, we can still clearly observe PL with an excellent signal to noise ratio in 4.4 (a) and (b). It should also be noted that the PL plots of (a) and (b) are on the same scale; hence, we did not observe any degradation in photoluminescence as a result of the pixel fabrication process.

In Figure 4.4(c), TRPL measurements on the bulk material give low-injection minority carrier lifetimes varying from 360 to 194 ns as temperature increases from 77 K to 300 K. Figure 4.4(d) shows the TRPL from the large area pixel array on thermal release tape. The pixel TRPL lifetime measurement shows a similar temperature dependence as the bulk InAsSb sample, with lifetimes ranging from 381 to 112 ns with increasing temperature. Although we are able to obtain a TRPL signal from the pixels, note that this is from a large

area cluster; the emission from single pixel would be far too weak to be time-resolved.

The TRPL shown in Figure 4.4(c) and (d) use the setup described in Chapter 2. As mentioned in Chapter 2, the detector utilized in this setup is a mercury cadmium telluride (MCT) detector. The benefits of the MCT detector used for these TRPL measurements include response out to wavelengths less than 12 μm, but more importantly, a relatively fast rise time of approximately 4 ns. However, the faster response time of the MCT comes with a significant sensitivity penalty, making detection of weak emission challenging. As demonstrated in the 77 K data of 4.4(c), the choice of fitting interval strongly determines the lifetime extracted from TRPL. In the low injection condition ($\delta n = \delta p < n_0$), the photo-excited excess carrier concentrations ($\delta n = \delta p$) are less than the background doping (n_0). Typically, low-injection is the regime of greatest interest for detector material characterization for two reasons: first, the low-injection region can be described by a single, power-invariant time constant, τ. As an example, if a detector is operated in continuous wave (CW) or relatively low frequency modulation, the total generated carrier concentration, Δn is the product of the generation rate, G_0, and lifetime, τ. If τ is a constant and therefore does not change as a function of incident power, then the generated carriers are proportional to optical power. Hence, the low injection condition defines a region of linear detector operation. The second importance of the low-injection region is somewhat more practical, as it corresponds to the typical photon fluxes encountered by infrared (IR) detectors.

Technically, in low injection, a single exponential fit can be used to extract a minority carrier lifetime. However, weak emitters and/or inefficient detection can result in the TRPL signal falling beneath the system noise floor before the low injection condition is satisfied. This limitation becomes particularly problematic for long wavelength materials,

where high-speed and high-sensitivity detectors are harder to come by, and where non-radiative recombination can dominate carrier dynamics and make for inefficient emission, especially at non-cryogenic temperatures [80][81]. When the noise floor is reached prior to satisfying low-injection, fitting to different portions of the decay signal will give very different lifetimes, as shown in Fig. 4.4(c), making the extraction of an accurate minority carrier lifetime challenging in the case of large area samples, and effectively impossible for a single, micron-scale infrared pixel.

However, we will demonstrate that by placing a single pixel into the concentrated fields of a microwave resonator (described in Section 4.3), we can effectively characterize the carrier lifetime of a micro-scale material without collecting any photoluminescence from the sample under test.

4.3 Single Pixel Transfer into a Microwave Resonator

4.3.1 SRR Fabrication and Dimensions

The dimensions of the specific SRR circuit used in this chapter are given in Figure 4.5. Although the fabrication is similar to the SRRs in Chapter 3 (Figure 3.4), the key difference is that we use a 99.6% aluminum oxide (Al_2O_3, also called alumina) substrate instead of semi-insulating gallium arsenide (SI GaAs). The reason for this is that we found a significant response from the bare, unloaded SI GaAs SRR when pumped with a 1064 nm laser, which is below the bandgap. The use of a 1064 nm bandpass filter ruled out any possible short-wave leaking diode light from the laser, and the lack of nonlinear scaling when using power reducing neutral density (ND) filters ruled out nonlinear two-photon absorption. Furthermore, at 11 K, (and at temperatures lower than approximately 50 K)

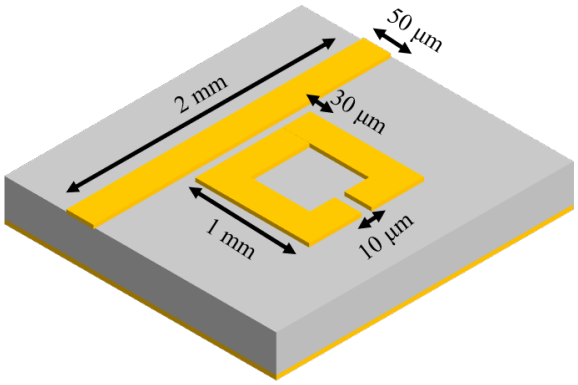

Figure 4.5: Dimensions of the fabricated SRR used in this chapter; the microstrip busline length is 2 mm, SRR side length 1 mm, busline width 50 μm, SRR to busline coupling gap 30 μm, and SRR split-gap 10 μm

despite using a sub-bandgap, 0.001% duty cycle (1 ns pulse width, 100 μs repetition rate) laser, we observed persistent photoconductivity. Currently, we attribute this anomalous response to trap states in the SI GaAs [82]. Hence, to avoid this, we used an alumina substrate, which, as expected, exhibited no photoconductive response by itself.

4.3.2 Pixel Transfer General Procedure

With the help of my colleagues Kyounghwan Kim (this chapter) and Yimeng Wang (Chapter 5) in Prof. Emanuel Tutuc's group who have developed an effective dry transfer technique, a single pixel was transferred to the split-gap of the SRR. Here a general overview of the process is given; for further details, I refer the reader to the Tutuc group's paper which describes the technique [83].

A PDMS stamp containing a cluster of pixels is placed in the sample holder of a Karl Suss MJB4 lithography/mask aligner. As seen in Figure 4.6(a), a single pixel is lifted from the PDMS host substrate by using the polymer PPC. Because the PPC is usually larger

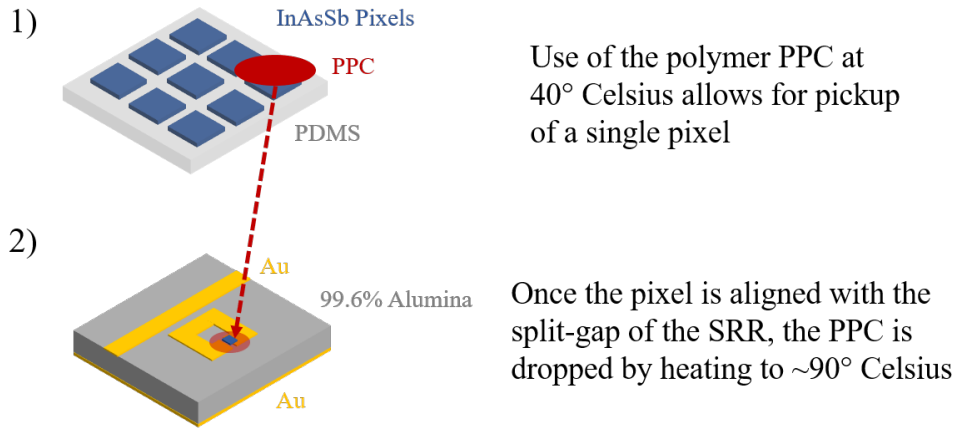

Figure 4.6: Overview of pixel transfer technique

than a single pixel, typically, we look around the edges of the pixel cluster to find a pixel that is slightly isolated; this allows us to more easily pick up only one pixel instead of several. At 40 degrees Celsius, the adhesion of the PPC was enough to overcome the van-der-Waals force between the pixel and PDMS. Once the pixel was lifted off the PDMS, the SRR circuit was placed in the MJB4 and using the microscope, aligned such that the pixel is on top of the bottom arm split-gap of the SRR, the region of highest fields as shown in Chapter 3. We found that ultimately, the pixel was strongly adhered to the PPC; hence, we needed to drop the PPC with the pixel, which was done by heating the PPC to > 90 degrees Celsius. To remove the PPC, the sample was very gently placed in acetone for 5 minutes and then isopropanol alcohol (IPA) for another 5 minutes. Once the sample was taken out, it was placed upright, which allowed the alcohol to fall down and dry on a wipe. It is critical to be gentle when placing the sample in solutions and to also avoid using nitrogen guns to blow dry the sample; otherwise, the pixel will fly out of the SRR.

4.3.3 hBN and Lumped Element Modeling

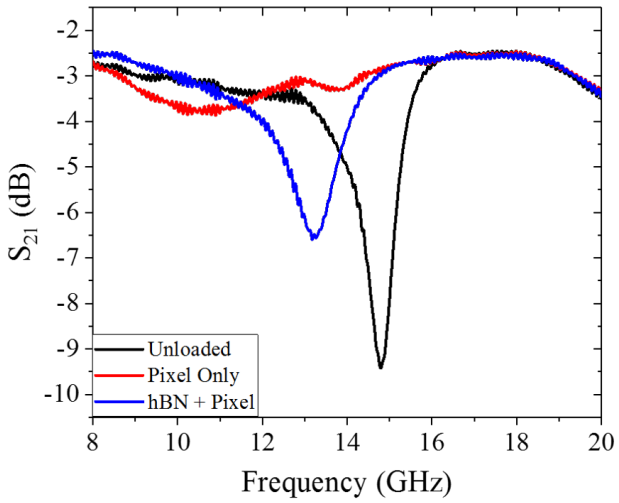

Figure 4.7: Effects of loading the pixel into the resonator; S_{21} spectra of the bare, unloaded resonator (black), pixel loaded resonator (red), and pixel loaded on top of a thin hBN layer (blue)

Because the InAsSb pixel is unintentionally doped, its dark conductivity can inadvertently short the resonator. Furthermore, filling the air in the split-gap of the SRR with a high index material can cause significant capacitive loading of the resonator. In Figure 4.7, the black curve shows the S_{21} spectrum of a bare, unloaded resonator with a split-gap of 10 μm. If an InAsSb pixel is added, a significant shift and weakening of the resonance is observed, as seen in the red curve. To help mitigate these effects, we placed an approximately 20 nm thick hexagonal boron nitride (hBN, provided by Takashi Taniguchi and Kenji Watanabe) spacer layer prior to the pixel. This layer adds a series capacitance to the pixel capacitance (which ultimately lowers the net added capacitance) and thus reduces the effects of the loading, as seen in the blue curve of Figure 4.7. Hence, depending on

the size and properties of the material under test (MUT), if the capacitive loading strongly quenches the resonance of the SRR, a spacer can be used to mitigate the effects.

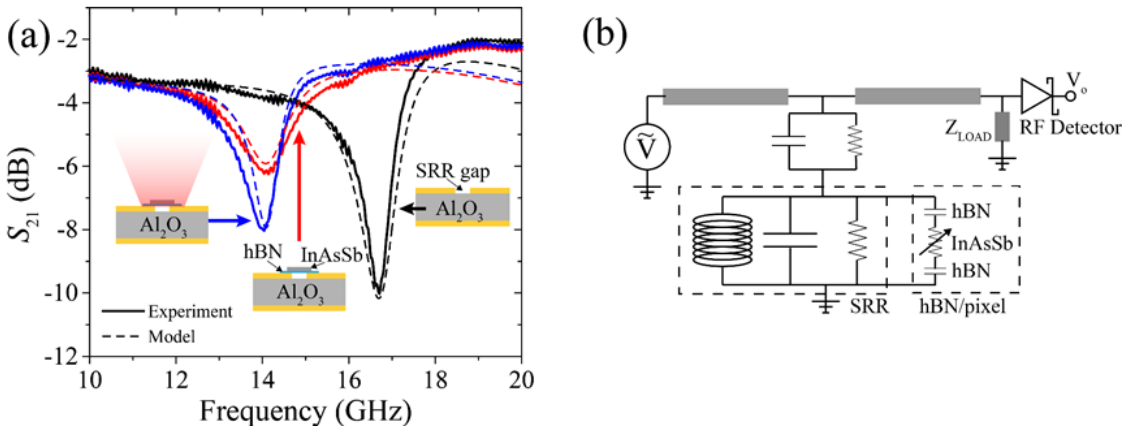

Figure 4.8: (a) Measured (solid lines) and modeled (dashed lines) $|S_{21}|$ parameter for the bare SRR (black), loaded SRR (red), and illuminated SRR (blue); (b) transmission line model used in (a)

For the pixel and SRR used for the proof of concept of the proposed technique, the experimental (solid curves) and modeled (dashed curves) S_{21} spectra for the unloaded (black), pixel and hBN loaded (red curves), and loaded with illumination (blue curves) resonator are shown in Figure 4.8(a). A clear bandstop feature is observed at 16.5 GHz for the bare SRR, which shifts to lower frequency (and weakens in magnitude) when the SRR is loaded with the InAsSb pixel and hBN spacer. The transmission line model for the bare and loaded circuit is shown in Figure 4.8(b), where the hBN and pixel are modeled as a shunt across the SRR consisting of a series combination of capacitance (pixel and hBN) and conductance (pixel). The overall procedure for modeling is very similar to what was described in Chapter 3 and will not be repeated here. However, the key difference is with the addition of the pixel and hBN to the SRR circuit. Hence, we modify Equation 3.1 to include the effects of the pixel in the cases of the loaded and illuminated SRR:

$$Z_{pix} = \frac{1}{j\omega C_{pix}} + R_{pix} = \frac{1 + j\omega R_{pix} C_{pix}}{j\omega C_{pix}} \tag{4.1}$$

When we consider the loaded SRR (red curve in Figure 4.8), this pixel impedance then appears in parallel with the RLC impedance of the resonator:

$$Z_{PixRLC} = \frac{1}{j\omega C} || j\omega L || R || Z_{pix} = \frac{j\omega RL}{j\omega L + R(1 - \omega^2 LC)} || Z_{pix} \tag{4.2}$$

The expression for coupling impedance remains the same:

$$Z_{Coup} = \frac{1}{j\omega C_{Coup}} || R_{Coup} = \frac{R_{Coup}}{1 + j\omega R_{Coup} C_{Coup}} \tag{4.3}$$

And finally, as in Chapter 3, the overall shunt impedance of the SRR is given as:

$$Z_{PixSRR} = Z_{PixRLC} + Z_{Coup} \tag{4.4}$$

When illuminated, as done in Chapter 3, a conductance (G_{pix}) can be added to the resistance of the pixel, which modifies the pixel impedance (denoted with a prime):

$$Z'_{pix} = \frac{1}{j\omega C_{pix}} + R_{pix} || \frac{1}{G_{pix}} = \frac{1 + R_{pix} G_{pix} + j\omega R_{pix} C_{pix}}{j\omega C_{pix}(1 + R_{pix} G_{pix})} \tag{4.5}$$

Optical excitation of the pixel generates EHPs, increasing the pixel conductivity, and thus modulating the circuit's S_{21} parameter. This modulation can clearly be observed in the modeled and experimental RF spectra of our device under illumination in Figure 4.8(a), where a significant change in transmitted RF signal can be obtained by changing the conductivity of the micron-scale pixel over the SRR gap via illumination.

4.4 Overview of μ-TRMRR Technique

Now that the pixel has been loaded in the strong, confined fields of the SRR, we can apply our micro-scale time-resolved microwave resonator response (μ-TRMRR) technique to extract the carrier lifetime.

4.4.1 Schematic and Working Principles

An overview of the μ-TRMRR technique is given in Figure 4.9. From Figure 4.8(a), it's clear that the greatest optical modulation of the loaded SRR occurs on resonance. Hence, an HP 8341B continuous wave (CW) RF source outputting 9 dBm at the resonant frequency of the SRR is connected to port 1 via a high frequency (< 26.5 GHz) cable and ground-signal-ground (GSG) probes. The resonant carrier signal propagates through the microstrip toward port 2, which is represented as the blue signal curve in Figure 4.9. A 1064 nm pulsed laser with a pulse width of 1 ns and a repetition rate of 10 kHz excites EHPs in the pixel which instantly (note that in practice, the modulation is not instant, which will be discussed in Subsection 4.6.2) modulates the amplitude of the resonant carrier. As these EHPs start recombining, the amplitude of the carrier restores to its original state. By using an RF Schottky diode detector (Pasternack 8013 model), the transient decay envelope (red curve in Figure 4.9), can be downconverted and extracted from the carrier. This signal is then sent to a 600 MHz LeCroy Waverunner 64-XI-A digital oscilloscope (triggered to the laser repetition rate) for averaging.

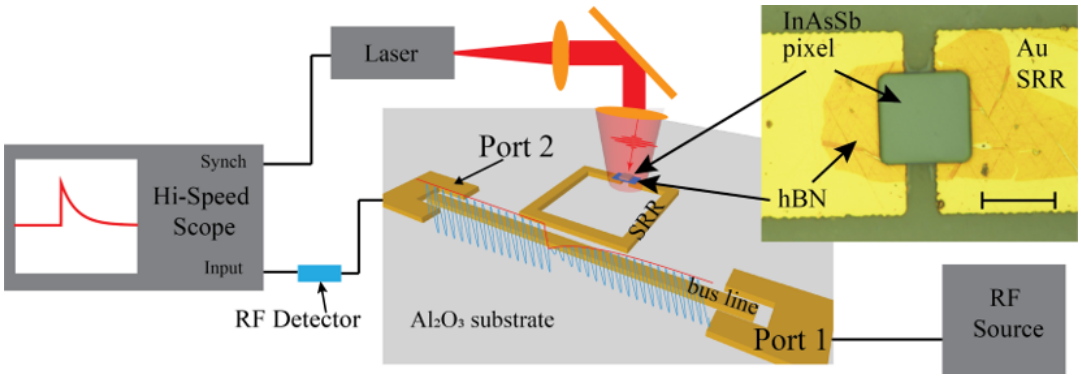

Figure 4.9: Schematic of of the μ-TRMRR technique for measuring carrier lifetimes in micro-scale volumes. A micrograph of the pixel and hBN transfered to the split-gap of the resonator is shown in the top right, with a scale bar of 20 μm

4.4.2 Linearity of Response

Linearity of the measured change in transmitted RF signal (ΔS_{21}) with respect to carrier concentration is key to extracting accurate, low-injection lifetimes. Fundamentally, the measured time response envelope must be proportional to carrier concentration to extract a carrier lifetime; otherwise, analysis becomes complicated as the contribution to the time response curve could be either from the material or from the circuit response. From the S_{21} plots in Figure 4.8(a), we observe that photoexcitation of carriers results in a negative ΔS_{21} (when measured on resonance, at the dip in the dark S_{21} spectra), which thus must limit the dynamic range of the circuit response to the dark S_{21} value. Under continuous wave (CW) optical excitation [Fig. 4.10(a)], we see a clear saturation in the ΔS_{21} with increasing laser intensity, which could result from the circuit response saturation, or alternatively, excitation power dependent mobility or lifetimes in the InAsSb, the latter coming from the increased contribution of fast non-radiative recombination mechanisms (Auger recombination in particular) to the total recombination rate [84][77][85][86]. However, our modeled

ΔS_{21} [Fig. 4.10(b)], as a function of increasing shunt conductance in the circuit, matches the experimental ΔS_{21} data under CW illumination, suggesting the observed saturation (at these excitation powers) is mostly intrinsic to the SRR circuit and unrelated to carrier lifetime.

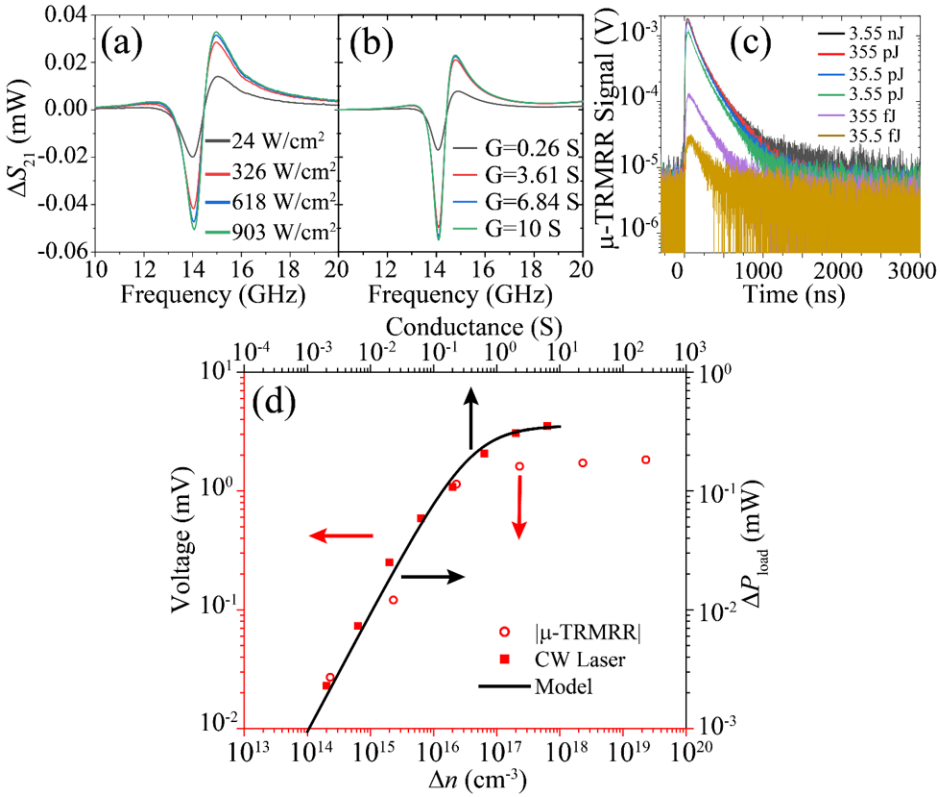

Figure 4.10: Linearity of the presented technique. (a) Measured ΔS_{21} (the change in the S_{21} parameter when light is incident upon the pixel) for varying CW laser excitation at room temperature, (b) modeled ΔS_{21} as a function of pixel conductance, and (c) measured room temperature μ-TRMRR signal as a function of energy incident upon the pixel. (d) $|\Delta S_{21}|$ on resonance from CW response shown in (a), (red squares), and peak $|\mu$-TRMRR| signal shown in (c) (red circles) as a function of excess carrier concentration and modeled $|\Delta S_{21}|$ (black, solid) as a function of conductance, from (b)

Figure 4.10(c) shows the excitation pulse energy dependence of the μ-TRMRR signal. Measuring the initial response amplitude $|\mu$-TRMRR| versus pulse energy, we can obtain an experimental picture of the circuit response (independent of carrier lifetime),

which also shows a clear saturation with increasing excitation energy. To properly compare the results in Figure 4.10(c), which has units of energy per pulse incident upon the pixel to 4.10(a), which has units of incident power, we can convert excitation units to generated carrier concentration, Δn. For the case of CW optical excitation, this becomes [67]:

$$\Delta n_{CW} = G_0 \tau = \frac{P_{inc} T_{window} T_{sample}}{V h\nu} \tau \tag{4.6}$$

Here, G_0 represents the carriers generation rate, which is simply the incident photon rate (incident power divided by photon energy, $h\nu$, where h is Plank's constant and ν is the frequency) multiplied by the transmission of the window (usually ZnSe, approximately 0.7) as well as the sample surface transmission (also typically approximately 0.7), divided by V, the total volume of generation (dimensions of the pixel 24 μm $\times$ 24 μm $\times$ 1 μm). Note that we assume all photons generated at this wavelength are absorbed. The calculated generation rate is then multiplied by τ, a carrier lifetime, which we assume to be a constant 250 ns, which will be justified later. Because of the size of the pixel, we also measured a two-dimensional spot size and applied a double Gaussian fit to extract a full-width half-max (FWHM) in each direction. A double Gaussian can then be used to describe the spatial characteristics of the beam. The expression is integrated within the bounds of the pixel, which then results in the total incident power upon the pixel. For further details, I refer the reader to Chapter 5, where a more comprehensive and rigorous treatment of incident power and spot size for responsivity measurements is provided.

A similar procedure can be applied to obtain the peak Δn for the |μ-TRMRR| measurements in Figure 4.10(c); however, this time, the units are in energy per pulse instead of power. So, the expression for peak generated carrier concentration becomes:

$$\Delta n_{peak} = \frac{E_{inc} T_{window} T_{sample}}{V h\nu} \tag{4.7}$$

Here, E_{inc} represents the incident energy per pulse. To obtain this value, the total energy per pulse of the full laser beam, E_{beam}, is obtained by measuring the average power and dividing by the laser repetition rate. Then, the incident energy is computed by measuring the two-dimensional spot size, obtaining a double Gaussian expression for the beam profile, and integrating within the area of the pixel, as mentioned in the CW power calculation above.

Once the excess carrier concentrations are known, both the |μ-TRMRR| signal and the circuit response to CW excitation assuming constant minority carrier lifetime can be plotted as a function of excess carrier concentration, as shown in the red axes of Figure 4.10(d). Similarly, the modeled circuit response as a function of added photo-induced conductance, G_{pix}, is plotted using the black axes. Both the |μ-TRMRR| data and CW response show a clear saturation at carrier concentrations greater than $10^{17} cm^{-3}$, which is near or slightly larger than the measured background carrier concentration in the InAsSb. For carrier concentrations less than $10^{16} cm^{-3}$, a region corresponding to the low-injection regime, our circuit response remains linear, in agreement with our modeled response for small photo-induced conductances. The results summarized in Fig. 4.10(d) suggest that while the circuit response saturates at large excess carrier concentrations, the strong sensitivity to carrier concentration and the linear response of our system across several orders of magnitude of carrier concentration offers a range of operation well-suited for exploring Auger, radiative, and Shockley-Read-Hall lifetimes in IR detector materials. This result points to the primary advantage of our μ-TRMRR technique when compared

to TRPL, which requires significant trade-offs between detector sensitivity and speed, and which for fast detector response times and weakly-emitting samples, cannot accurately measure carrier dynamics at low carrier concentrations.

4.4.3 Temperature Dependent Minority Carrier Lifetimes of a Single InAsSb Pixel

By housing our samples in an ARS cryogenic probe station, we can perform the μ-TRMRR as a function of temperature. Figure 4.11(a) shows the temperature dependent μ-TRMRR data from the single InAsSb pixel, at the same pump energy used for the TRPL data in Figure 4.4 (but with only 2,000 averages, compared to the 50,000 averages required for the TRPL). A clear improvement is observed in the μ-TRMRR SNR, with fitting possible to much longer times. Figure 4.11 also shows a direct comparison of the TRPL data from the array of InAsSb pixels [Fig. 4.11(b)] and our μ-TRMRR results from a single InAsSb pixel [Fig. 4.11(c)] at 300 K (both with 2,000 averages, for an accurate comparison). In order to achieve SNR adequate to extract a lifetime, the pixel array requires pumping with a pulse energy of 68 nJ, whereas a comparable signal is observed from the μ-TRMRR with only 68 pJ of pulse energy (equivalent to 35.5 fJ incident on the pixel).

Even with the three orders of magnitude attenuation in pump energy, the μ-TRMRR allows for fitting to the tail of the emission signal, where the tail of the TRPL emission is well below the noise floor. Thus, the μ-TRMRR approach has significant benefits over TRPL, where weak signals from poor emitters or long carrier lifetimes (effectively stretching photon emission over longer time intervals), can lead to low SNR and thus inaccurate measurement of lifetimes. Moreover, the significant improvement in our time-response data using the μ-TRMRR approach comes from the response of a single pixel, as opposed

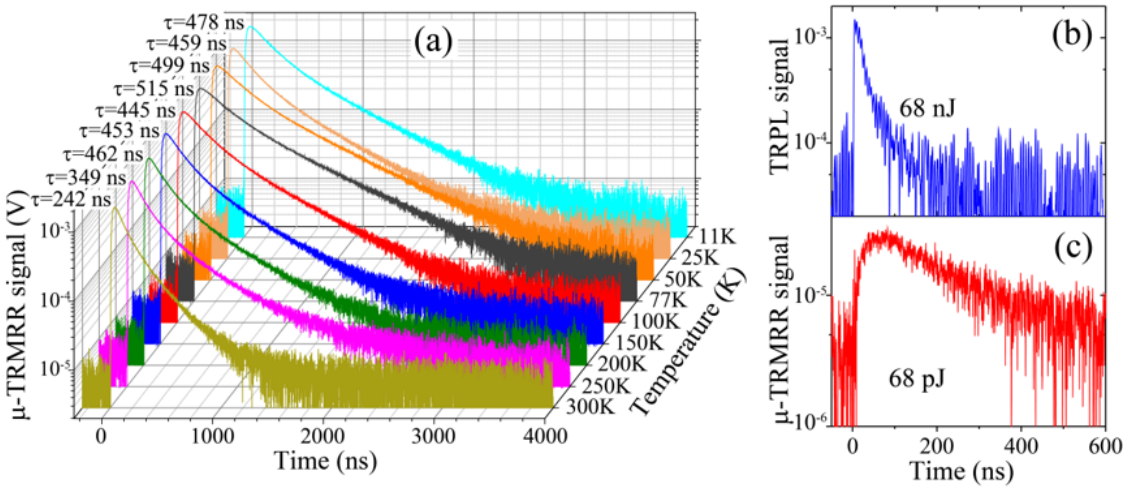

Figure 4.11: Transient decay curves. (a) Temperature-dependent μ-TRMRR signal from InAsSb pixel using 35.5 pJ pulse energy on pixel and with 2,000 averages on oscilloscope. Extracted lifetimes are shown above each curve. (b) time-resolved photoluminescence (TRPL) response of pixel array with 68 nJ laser pulse energy (equivalent to 16.6 nJ incident on pixels) and (c) μ-TRMRR data for a single pixel with 68 pJ total laser pulse energy (equivalent to 35.5 fJ incident on pixel). Both experiments in (b) and (c) are performed at 300 K, with 2,000 averages on the oscilloscope

to the TRPL data, which comes from the collective response of more than 1,000 pixels. As TRPL requires three orders of magnitude more power with >1,000 pixels, our μ-TRMRR approach offers at least a 10^5 improvement in sensitivity when compared to TRPL performed with a conventional, high-speed MCT. Alternatively, by calculating the absorbed optical energy required to achieve comparable responses from the pixel array (16.6 nJ) and the single pixel in our μ-TRMRR system (35.5 fJ), we similarly obtain a > 10^5 improvement in sensitivity.

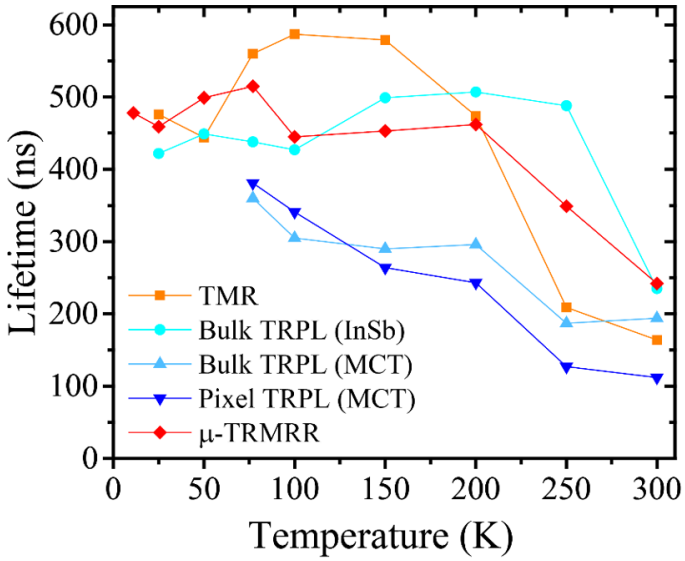

Figure 4.12: Comparison of lifetime measurement techniques. Extracted carrier lifetimes as a function of temperature for time-resolved microwave reflectance (TMR) on as-grown InAsSb (orange), time-resolved photoluminescence (TRPL) on as-grown InAsSb using InSb (cyan) and mercury cadmium telluride (MCT) (light blue) detectors, TRPL from pixel array using MCT detector (blue) and single-pixel μ-TRMRR (red) techniques. TRPL (InSb), TMR, and μ-TRMRR agree well, but as shown, when using a less sensitive detector (such as MCT), the TRPL signal falls beneath the noise floor before the low-injection condition is satisfied, preventing an accurate lifetime extraction

4.5 Comparison of Lifetime Techniques

Although we demonstrated the linearity of the described uTRMRR system in Subsection 4.4.2, to further verify our results, we asked collaborators at Sandia National Labs (Clark Kadlec, Michael Goldflam, and Eric Shaner) to perform measurements on the bulk InAsSb using both their TMR system (described in [84]) and TRPL using a more sensitive (but slower) indium antimonide (InSb) detector. The lifetime data from TMR, our μ-TRMRR technique, and TRPL (with MCT and InSb detectors) are compared in Figure 4.12. We observe that the TMR, μ-TRMRR, and TRPL (with an InSb detector) all give similar lifetimes and temperature dependence, indicating that the increased sensitivity of our

μ-TRMRR approach does not come with an associated penalty in the accuracy of lifetime extraction. However, the MCT detector TRPL data shows a clear discrepancy in extracted lifetimes, particularly as temperature increases and emission from the material decreases in efficiency. This effect again points to the primary deficiency of the TRPL method as described earlier in the discussion of Figure 4.4(c), where weak emission and/or low detector sensitivity prevents the accurate measurement of low carrier injection lifetimes in the tail of the decay from poorly emitting samples. The use of an InSb detector buys us at least an extra order of magnitude in sensitivity when compared to our MCT detector, which allows for a more accurate fit further into the tail of the TRPL signal as low injection carrier concentrations are now above the noise floor. However, this comes at a time resolution penalty as the InSb detector has a time constant of approximately 23 ns (as opposed to a 4 ns rise time from the MCT). Furthermore, InSb can only detect out to the mid-wave (approximately 5.5 μm). It should also be noted that the InSb TRPL measurements were performed on bulk material, and the increase in sensitivity obtained by using the InSb detector is still not enough to resolved emission from a single pixel.

In summary, using the μ-TRMRR method we are able to effectively characterize the minority carrier lifetime in a micro-scale InAsSb pixel with > 10^5 sensitivity when compared to results obtained by TRPL with an MCT detector. While we have illustrated the utility of our approach using bulk InAsSb pixels for our proof of priniciple demonstration, we also wanted to determine the extent to which the μ-TRMRR technique is applicable to even smaller volumes of material (such as a 2D materials) and analyze time resolution limits.

4.6 Application of Technique to Other Material Systems

In this section, we show that the μ-TRMRR method can be applied to 2D materials as well as high-speed materials. Work in this section serves as an extension of the μ-TRMRR to further demonstrate its utility; as such, note that data in this section has, as of yet, neither been published nor peer reviewed.

4.6.1 Monolayer WS_2

In a collaboration with Prof. Keji Lai's group (Physics department at UT), we attempted to characterize the lifetime of a monolayer of WS_2 placed within our SRR. Thus far, we have performed temperature dependent and power dependent μ-TRMRR measurements; while we were able to obtain a strong, resolvable signal across several temperatures and powers, definitive conclusions have not been drawn yet regarding the data set. Its inclusion in this section of the dissertation serves to merely reinforce sensitivity claims of the μ-TRMRR and show that we can, in fact, obtain a reasonable SNR from a 2D material using this technique. This μ-TRMRR measurement is similar to that of the InAsSb single pixel measurements except the laser used is a 532 nm, 20 kHz repetition rate, 1 ns pulse width laser.

Peak carrier concentration is calculated in a manner similar to Equation 4.7, except this time, the material is two dimensional; furthermore, we can no longer assume that all photons entering the material are absorbed. The expression therefore becomes:

$$\Delta n_{peak} = \frac{\alpha E_{inc}}{A} T_{ND} \tag{4.8}$$

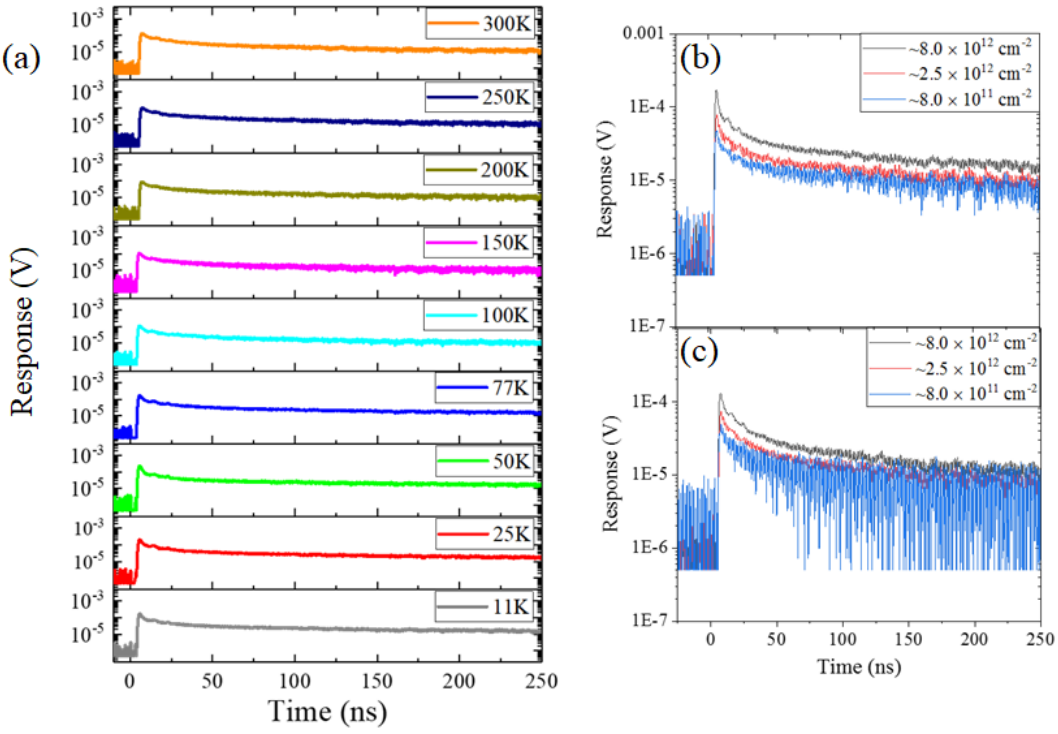

Figure 4.13: μ-TRMRR technique performed on monolayer WS_2: (a) temperature dependence performed using an injected carrier concentration of approximately $8\times10^{12}cm^{-2}$; power dependence performed at both 11 K (b) and 300 K (c)

where α is the percentage of absorbed photons, A is the area of the WS_2 flake, $h\nu$ the energy per photon, and T_{ND} is the transmission of the neutral density filter. In Figure 4.13, we see that the transient decays, which have extracted lifetimes of approximately 500 ns, have a general lack of dependence on both the temperature (a) and power (b and c). Currently, we attribute this to long trap lifetimes in the material, although future studies (such as passivation of the layer using hBN) would need to be performed to make more specific claims. Regardless, the data presented in Figure 4.13 has excellent SNR, which further

supports the utility of the μ-TRMRR technique toward small volumes.

4.6.2 Pushing to High-Speed Materials

At this point, some readers may have noticed and pointed out that the μ-TRMRR results on the InAsSb seem to have a characteristic rise time; this is especially clear in Figure 4.11(c). We believe that this rise time comes from the use of the Schottky diode (Pasternack 8013) which has an output capacitance of 470 pF as listed on the specifications. Since the scope is terminated with 50 Ωs, we can approximate a time constant on the order of 25 ns, which is close to what we see in the rise time of Figure 4.11(c). Technically, this should be considered in our sensitivity claim; because the time resolution is at most an order of magnitude worse than that of the TRPL data shown in Figure 4.11(b), one could argue that since the bandwidth would be less, there is also less integrated noise. However, I would like to mention that we have considered this! In actuality, our improvement in SNR is closer to $> 10^6$, but to account for this difference in time resolution (and therefore integrated noise), we tone down our claim to $> 10^5$.

Although faster Schottky diodes with similar bandwidth and responsivities exist (such as the Krytar 302A used in Chapter 5), one could ask: is there a way to operate without the Schottky diode and improve the time resolution? In this section, we show that such an operation is possible and results in significantly greater time resolution. In Figure 4.9, we see that a blue resonant carrier propagates down the microstrip busline and is modulated by the recombination of optically generated EHPs. In the frequency domain, this modulation (which is significantly lower frequency than the driving carrier frequency) actually mixes and reads out with the resonant carrier. Hence, the Schottky diode serves as

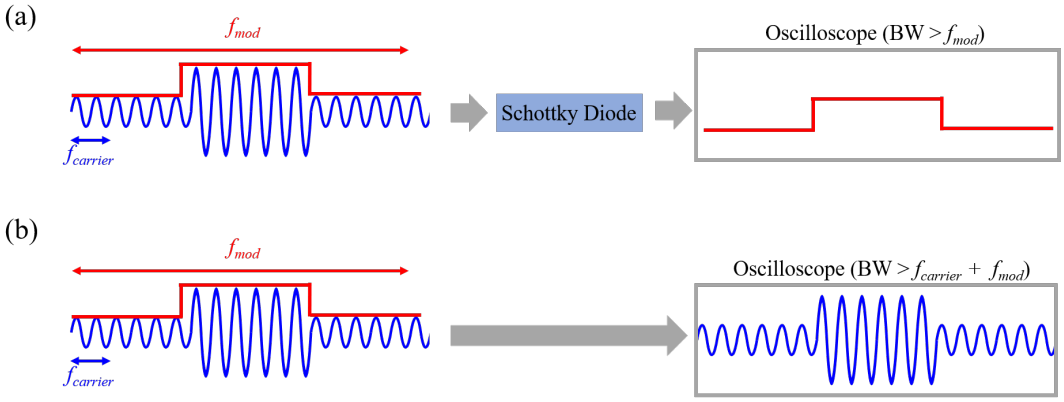

Figure 4.14: (a) An optical modulation (red square wave) rides on top of the carrier (blue sinusoid) and enters a Schottky diode, which "de-mixes" and produces the modulation as the intermediate frequency (IF); (b) the mixed optical modulation and carrier go straight to an oscilloscope without a Schottky diode; note that the oscilloscope would require a bandwidth greater than $f_{carrier} + f_{mod}$ instead of needing to be simply greater than f_{mod}, which is the case in (a)

a second mixer which extracts the transient decay envelope from the carrier, as shown in Figure 4.14(a). In principle, we could simply send the mixed carrier and transient envelope straight to an oscilloscope (Figure 4.14); however, as our carrier is in the Ku band (12-18 GHz), this would require an oscilloscope with a bandwidth of 18 GHz instead of a scope with a bandwidth greater than frequency components of the transient decay only. Using an 18 GHz scope borrowed from Dr. Praveen Pasupathy in Prof. Neikirk's group, we performed a μ-TRMRR measurement (without the Schottky diode and using a borrowed fs fiber laser) on high-speed lattice mismatched indium antimonide (InSb) pixels [44] to show that without a Schottky diode, we can achieve sub-nanosecond rise times using our technique! Note that because we could not simultaneously synchronize the output from the RF source and the laser repetition rate, the resonant carrier is not clearly distinguishable from the time response curve shown in Figure 4.15; instead, only the decay, which is

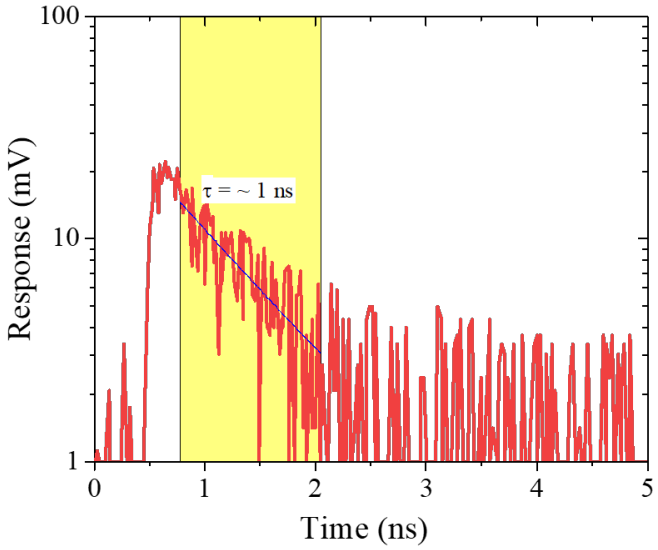

Figure 4.15: μ-TRMRR response of a high-speed indium antimonide (InSb) pixel without the use of a Schottky diode; note that the time resolution is much better than in 4.11(c), with a rise time significantly less than a nanosecond

triggered to the laser, is visible.

The high speed detectors using InSb pixels have been developed even further by Yinan Wang, my lab mate and the successor to this project. More detailed results and analysis will be described in future publications and his PhD dissertation.

4.7 Summary of Technique

In summary, we have presented the micro-scale time-resolved microwave resonator response (μ-TRMRR) technique, capable of measuring minority carrier lifetimes in micro-scaled volumes of optoelectronic materials without the need for contacts or current collection. When compared to the results from TRPL measurements on the same material using

an MCT detector, we show that the μ-TRMRR technique achieves a comparable signal using a factor of > 10^5 less absorbed energy, which allows us to characterize micron-scaled volumes of weakly emitting infrared materials. Our μ-TRMRR results match well with lifetimes extracted from both conventional TMR and TRPL measurements, pointing to the accuracy of our technique for measuring carrier lifetimes in weakly-emitting or long-lifetime materials. Since our technique measures the material response at microwave frequencies, light emission from our samples is not required, and thus there are no collecting optics and optical detectors which have to be adjusted to cater to optoelectronic materials operating in different wavelengths.

Chapter 5

Resonant Microwave Photoconductive Detectors

In this chapter, we formally evaluate a pixel reactively coupled to a microwave split-ring resonator (SRR) as a candidate for mid-IR light detection. This work is currently under review as "Room Temperature Mid-Infrared Detection via Resonant Microwave Circuits", so much of the figures and text have been taken or adapted from the submitted manuscript. The authors listed on the manuscript are: Sukrith Dev, Yinan Wang, Yimeng Wang, Monica Allen, Jeffery Allen, Emanuel Tutuc, and Daniel Wasserman.

Here we demonstrate a room temperature mid-wave infrared (MWIR < 5 μm) photoconductive detection architecture utilizing a compact, Ku-band microwave SRR loaded with a micron-scale indium arsenide antimonide (InAsSb) pixel. Our resonant microwave photoconductor (RMPC) does not require the fabrication of ohmic contacts, or the need for DC current collection. We compare our RMPC architecture to a traditional DC photoconductor (DCPC) and evaluate the conditions in which the overall sensitivity of our RMPC exceeds that of the DCPC. Time domain simulations suggest that while the architecture may not directly provide advantages with regard to generation-recombination (G-R) noise in the semiconductor, the resonator can shape and suppress the fundamental Johnson thermal noise of the semiconductor photon-absorbing element loaded within, resulting in decreased total noise and thus increased detectivity, with the SRR circuit itself being the primary

generator of thermal noise. For this material system, we show that our RMPC has more than a factor of three improvement in the overall Johnson-limited D* when compared to the standard DCPC and discuss situations for which this improvement could be significantly larger as well as practical noise considerations.

5.1 Background

In this section, a motivation is provided for why a contact-free detection architecture, especially in the mid-IR, could have inherent advantages over direct current (DC) photodetectors (Subsection 5.1.1). Next, some background on the history of RF-based sensors and detectors will briefly be mentioned in Subsection 5.1.2, followed by an overview of the proposed architectures (5.1.3) and a discussion on specific detectivity (D*, described in Subsection 5.1.4), the main metric used to quantify sensitivity in this chapter.

5.1.1 Motivation for Contact-Free Detector Architectures

Consider Figure 5.1(a), in which a square-shaped narrow bandgap semiconductor absorber of side length l is uniformly illuminated with an irradiance of Φ, in units of W/cm^2. Assume that the irradiant beam has a diameter of l, energy greater than the bandgap of the semiconductor, and that the absorber is sufficiently thick such that all of the light which enters the material is absorbed and generates some signal (either a photocurrent or voltage). In such a system, noise (which will be discussed extensively in Section 5.3), in the form of thermal fluctuations in the number of free carriers within the semiconductor, serves as a limiting mechanism in the detectivity of the detector. Such noise is especially problematic for narrow bandgap materials operating at room temperature. The total noise resulting from

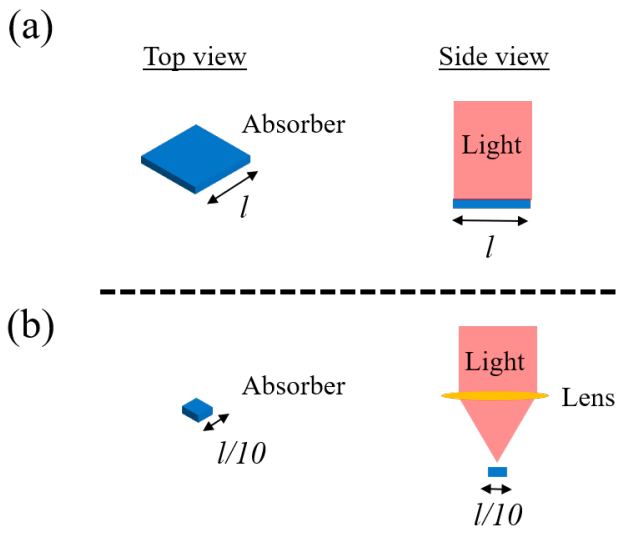

Figure 5.1: Comparison of signal to noise ratio (SNR) between two different area semiconductor absorbers; (a) shows a square absorber of length l, and (b) shows that absorber of length $l/10$ can still collect the same incident radiation as (a) with the help of focusing, despite having a significantly smaller area

these fluctuations is known to be proportional to the $\sqrt{A}$ [36], where A is the area of the absorber, or $l \times l$ in this case. To combat this, intuitively, one could reduce the active area of the absorber to reduce the noise, as shown in Figure 5.1(b). However, to still obtain the same response for the given irradiance, Φ, some form of focusing, such as a lens, is required to ensure all of the incident photons enter the absorber. Therefore, assuming that the detector is still operating under linear low-injection conditions (as mentioned in Chapter 4), the thermal fluctuation noise in Figure 5.1(b) is an order of magnitude less than that of Figure 5.1(a) (due to a 100 times decrease in area), but because of the increase in light absorption due to focusing, the smaller detector still maintains the same signal level as the larger one.

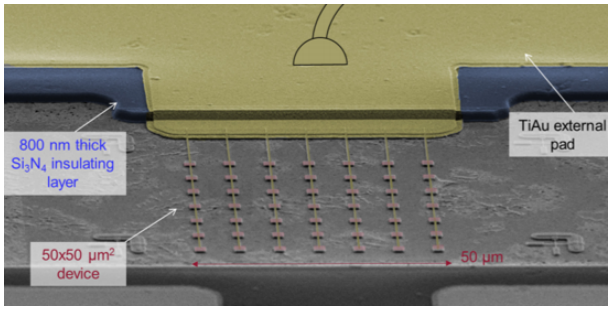

Figure 5.2: Work done by Carlo Sirtori's group demonstrating the increase in detector operating temperature by reducing thermal fluctuations via miniaturization of active area; figure taken and adapted from their published work in [13]

In the extreme case of this miniaturization concept, the system reaches its diffraction limit, and light can no longer be further concentrated by the lens. Thus, further reduction in the detector area provides no additional sensitivity in detection. For this reason, there has been significant interest in applying nanophotonic and metamaterial concepts to confine light to subwavelength volumes. In Figure 5.2, work from Carlo Sirtori's group [13] demonstrates the use of a patch cavity to miniaturize their quantum well infrared photodetector (QWIP) absorbers. By doing so, they demonstrated increased operating temperature (up to room temperature) from reduced thermal fluctuations for their device. However, we can clearly see in Figure 5.2 that all of the active areas are electrically connected as they are using a DC detection architecture. If a contact-free architecture could be developed and alleviate this requirement, the door would open to a plethora of materials and nano structures which would otherwise be impractical to employ due to the requirement of contacts.For instance, electrical connections between absorbers could become difficult for structures such as densely packed absorbers on the micro or nanoscale, nanowire arrays, all-dielectric resonators, and monolithically integrated doped semiconductors for long-wave infrared

plasmonic structures.

5.1.2 Microwave Resonators: From Sensors to Detectors Overview

Contact-free techniques for measuring response to optical signals are of significant interest for their flexibility in use of material and the ability to design light concentrating structures without having to worry about the optical response of the conducting contact. In addition to the μ-TRMRR technique presented in Chapter 4, microwave resonant structures have been successfully used for gas sensing, detection of cosmic background radiation using superconducting kinetic inductance detectors [62], material characterization [66][87], permittivity measurements [88][89][90], and microfluidics sensing [91][92]. For further reading, in addition to the references provided, I recommend the PhD dissertation of Jack Naylon from Cardiff University, which provides an extensive review of these techniques. Despite the vast applications of microwave resonant sensors, there have been significantly fewer demonstration of such structures' utility for light detection, especially in the mid-infrared. To the best of my knowledge, the use of microwave structures for photoconductive light detection was first presented in 1964 by Sommers and Teutsch in the Proceedings of the IEEE [14]. They proposed the coupling of photoconductive materials to RF structures such as waveguides or resonant structures, as shown in Figure 5.3 (a) and (b), respectively.

Nonetheless, these RF architectures employed were rather bulky and impractical for implementation in optical systems, especially in comparison to other existing DC detection architectures. Over the past decades, however, significant advances in microwave technology, commercially-available RF components, and semiconductor material growth and fabrication techniques, have opened the door to revisiting the concept of reactively

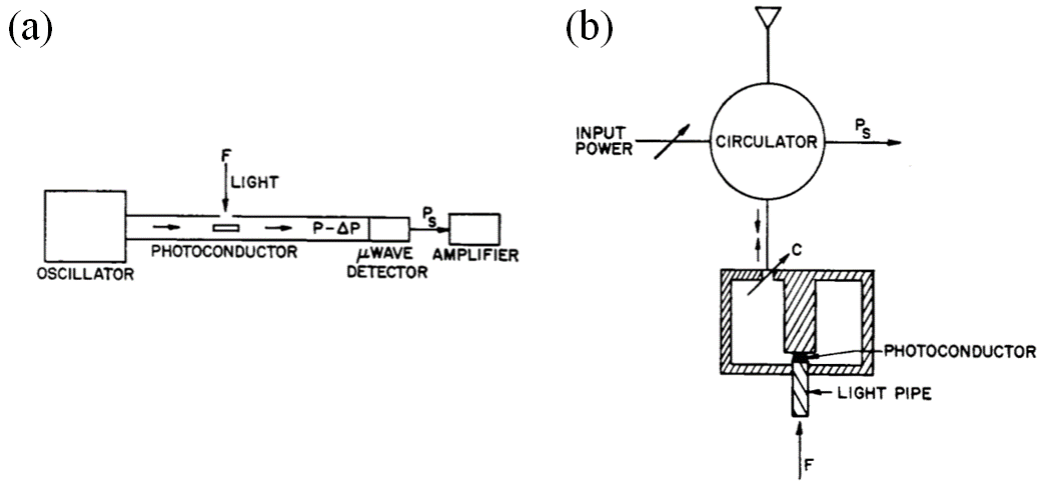

Figure 5.3: (a) Coupling of photoconductive absorber to a transmission line; (b) reflection cavity-based photoconductive detector. Figures taken and adapted from [14]

coupled detector readout architectures. Specifically, as seen in Chapters 3 and 4, the use of inexpensive and compact sub-millimeter scale RF resonators allows for strong confinement of RF fields, and thus enhanced interaction with absorber material integrated into the RF resonator.

5.1.3 Overview of Direct Current Photoconductors and Resonant Microwave Photoconductive Architectures

If a newly proposed architecture, such as a microwave-based contact-free architecture, significantly underperforms compared to a standard direct current (DC) architecture, any advantages associated with avoiding contacts (mentioned in Subsection 5.1.1) could be nullified. Hence, in this chapter, we will compare our proposed contact-free architecture to a standard DC photoconductor (DCPC), shown schematically in Figure 5.4(a). A DC voltage source applies a bias across the photoconducting element and a series resistor, with

the voltage output read across either the photoconductor or the resistor. Light incident upon the photoconducting element with an energy greater than the bandgap excites electron hole pairs (EHPs), which (nominally) lowers the resistivity of the photoconducting element and changes the voltage measured at the output. However, the DCPC, like most other architectures, is a DC system that requires a combination of non-blocking ohmic contacts and electronic transport.

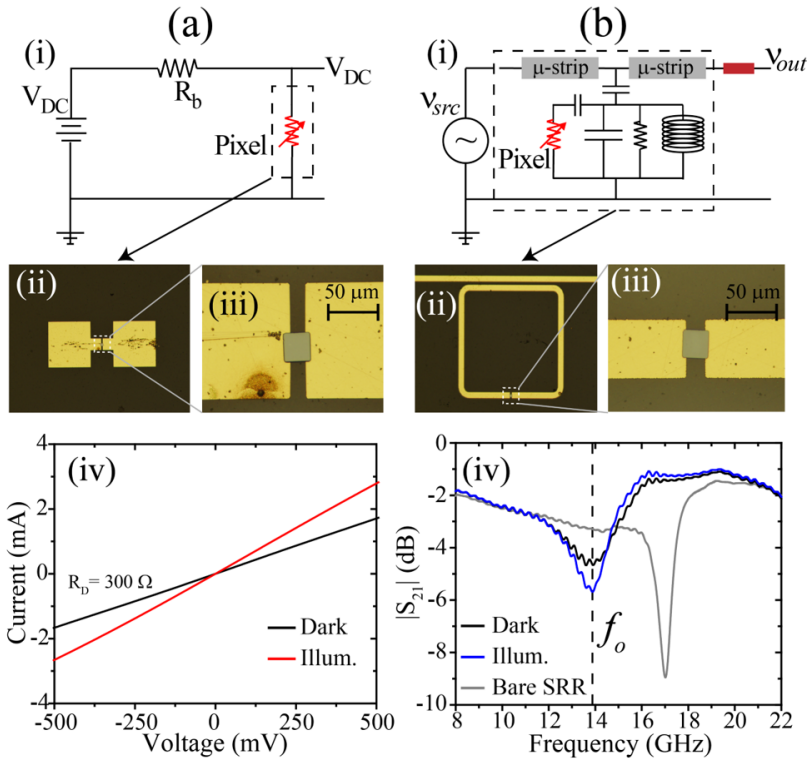

Figure 5.4: (a) DC photoconductor and (b) resonant microwave photoconductor; (i) detection circuit diagrams, (ii) micrograph of the overall device with (iii) an expanded view; (iv) dark and illuminated (100 μW of power at λ = 3.39 μm) current-voltage (DC photoconductor) and $|S_{21}|$ curve (resonant microwave photoconductor) plots.

Here we propose a photoconductive detector architecture, the resonant microwave

photoconductor (RMPC), which utilizes a millimeter-scale, on-chip Ku-band microwave split-ring resonator (SRR) loaded with an active infrared semiconductor material, shown in Figure 5.4(b). In Fig. 5.4(b-iv), we see the expected band stop feature [12] from the $|S_{21}|$ at around 17 GHz (black dashed lines) for the bare SRR coupled to the microstrip busline. In this work, we demonstrate a proof of principle using a micro-scale pixel of narrow-bandgap III-V material, indium arsenide antimonide (InAsSb) as described in Chapter 4, capacitively loaded via van-der Waals placement [83] into the split gap of our SRR so as to maximize overlap with the strong, localized RF fields at this position. As a result of both capacitive loading and unintentional doping (UID) from the InAsSb pixel, the resonant feature at 17 GHz red-shifts and the quality factor reduces as in Chapter 4, although a resonant band stop feature is still clearly observable, as seen in the solid black curve of Fig. 1(b-iv). It is worth noting that here, we do not make use of the hexagonal boron nitride (hBN) spacer that we did in Chapter 4. To minimize capacitive loading effects seen in Figure 4.7, instead of using an hBN spacer, we use a different SRR with a slightly larger split-gap; since the fields are slightly less localized for larger split-gap SRRs [63][12], the SRR is less impacted by the effects of the pixel loading.

When light is incident upon the semiconductor, generated electron-hole pairs (EHPs) modulate the semiconductor conductivity and hence the RF circuit's S_{21} parameter (Fig. 5.4(b-iv) blue curve) as done in Chapter 4. A microwave signal on the microstrip busline is modulated by this optically-induced change in impedance, and the modulated signal is then read out by an RF Schottky diode detector. Although our RMPC architecture is contact-free, to evaluate and compare the sensitivity performance relative to the DCPC, we use the specific detectivity (D*) metric, described next in Subsection 5.1.4.

5.1.4 Specific Detectivity

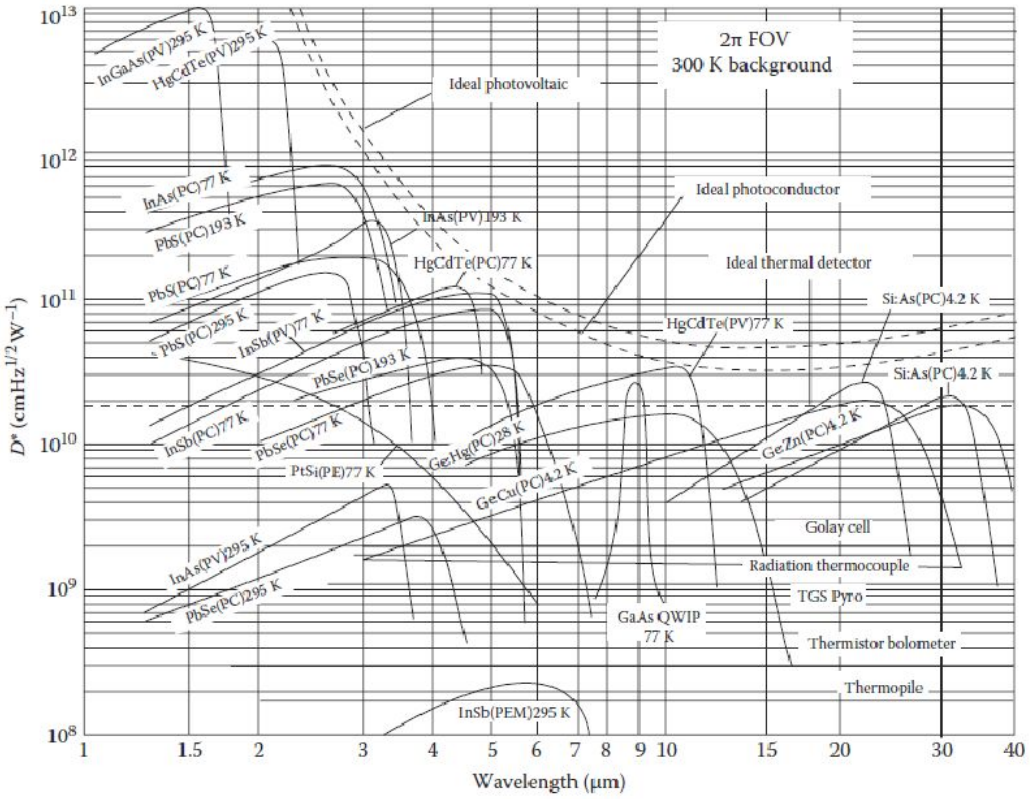

Figure 5.5: Spectral specific detectivities (D*) of several commonly used detectors. Taken and adapted from [4]

In this chapter, the specific detectivity (D*) is used as the metric for quantifying sensitivity. It is therefore appropriate to define D*, explain the origin of its constituent terms, and describe methods and limits associated with its calculation. Generally, the D* as a function of both wavelength, λ, and bandwidth, Δf, can be expressed as (in units of $cmW^{-1}Hz^{1/2}$):

$$D^*(\lambda, \Delta f) = \frac{\sqrt{A}}{NEP(\lambda, \Delta f)} \tag{5.1}$$

where A is the area (cm^2) and $NEP(\lambda, \Delta f)$ is the noise equivalent power in units of $WHz^{-1/2}$, or the lowest detectable power as a function of wavelength, λ, normalized to a measurement bandwidth, Δf. Here we define the NEP as:

$$NEP(\lambda, \Delta f) = \frac{v_n(\Delta f)}{R(\lambda)} \tag{5.2}$$

where R is the responsivity (V/W) and v_n is the output noise normalized to the bandwidth considered ($V/Hz^{1/2}$). Note that the wavelength dependence of both the D* and NEP comes from the responsivity, or the electrical output per input optical power. This is generally true for semiconductor-based detection architectures for at least two reasons: first, the absorption coefficient for the semiconductor varies as a function of wavelength. For a bulk material, if the absorption coefficient follows the three-dimensional density of states, it is proportional to $\sqrt{E - E_g}$, where E is the energy of the light and E_g is the bandgap of the semiconductor. Hence, more absorption will occur for higher energy photons within the thickness of the detector. However, even if the detector is sufficiently thick and most photons above the bandgap are absorbed, the detector will still exhibit a wavelength dependent responsivity. This is because at shorter wavelengths (higher energies), the energy per photon is greater, so for a given power, there will be fewer photons and therefore fewer electron-hole pairs (EHPs) generated. This is known as the 'quantum defect', and plays an important role when trying to optimize the efficiency of detectors and/or solar cells. Thus, when detectors are sufficiently thick, oftentimes the responsivity (and consequently the D*) will drop as the

energy of the incident photon becomes sufficiently greater than the bandgap. We can clearly see this relationship in Figure 5.5, where the specific detectivities of the quantum detectors have a significant spectral dependence. The responsivity setup and methodologies used in this dissertation are described further in section 5.2.

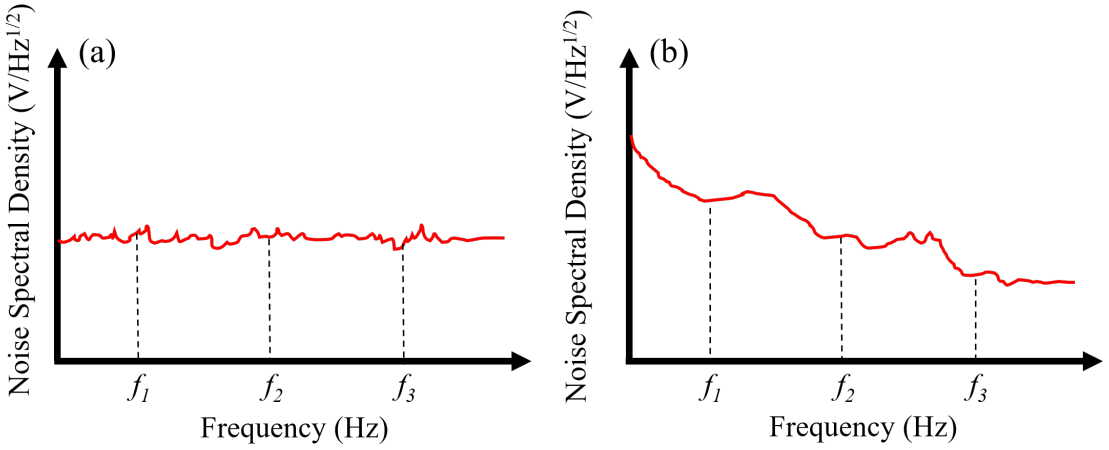

Figure 5.6: Example noise spectra of (a) white noise and (b) frequency dependent spectra

In many analyses, the bandwidth-dependence, Δf, of v_n is neglected from the D* expression. Even though the v_n term is the total bandwidth normalized voltage noise, it may still have a dependence on the bandwidth considered if different frequency bands have different noise spectral densities. To illustrate this, consider the two cases in Figure 5.6. In (a), an example of a white noise spectral density (NSD) is shown. If a source of noise is considered white, it will exhibit no frequency dependence, as seen in Figure 5.6(a). The bandwidth-normalized noise, v_n, can be calculated across a bandwidth, $\Delta f = f_j - f_i$, from a NSD as follows:

$$v_n = \sqrt{\frac{\int_{f_i}^{f_j} (NSD)^2 df}{f_j - f_i}} \tag{5.3}$$

When the noise is white, the frequency bandwidth and region in which the noise is integrated does not affect v_n as it is effectively normalized out. For example, referring to Figure 5.6(a), the total integrated noise in the bandwidth from f_1 to f_2 will be less than the total integrated noise from f_1 to f_3 since $f_3 > f_2$. However, when the total noise is normalized by the bandwidth considered, we see that the bandwidth normalized noise, v_n, is independent of the band considered.

While this is generally true for white noise sources, much of the noise considered in this dissertation does not possess frequency independence; hence, in the D* expression in equation 5.1, there will be a bandwidth dependence on the noise, v_n, even when the bandwidth is normalized over. This is clearly seen in Figure 5.6(b); because the NSD does not possess a spectrally flat shape, even when the total noise is normalized by the bandwidth over which the noise is integrated, a larger v_n will be obtained for $\Delta f = f_2 - f_1$ versus $\Delta f = f_3 - f_1$. Further noise analysis is given in section 5.3.

5.2 Comparison of Responsivities

5.2.1 Bias Dependent Setup

The responsivity, as mentioned, is the electrical output generated per unit incident optical power. Because both the DCPC and RMPC are photoconductive detector architectures, the output will be a voltage; thus, the responsivity will be in units of V/W. To measure the responsivity, typically, a blackbody of known temperature is placed a known distance

away from the sample. An optical bandpass filter allows for a single wavelength (though of course, in practice it will have a finite bandwidth) from the blackbody to be incident on the sample. Furthermore, since both power and spectral distributions for blackbodies are well-known, the power incident upon the sample can be calculated. If the blackbody is chopped, then a lock-in amplifier (LIA) can be used to determine the output of the sample; finally, the output can be divided by the input power for a responsivity. This approach for responsivity calculations is commonly used; details are described in the PhD dissertation of Dan Zuo, one of my former labmates.

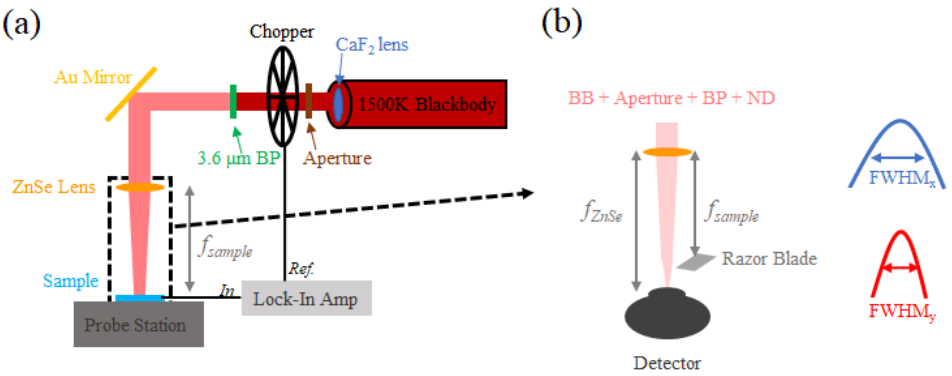

Figure 5.7: (a) Diagram of the responsivity setup employed in this chapter; (b) shows the method of beam spot calculation

However, a slightly different approach is used in this section where the power incident upon the sample is partially measured instead of fully calculated. This approach is used for practical reasons: since our samples are housed in a probe station, the blackbody must be mounted on the side, collimated, reflected downward toward the sample, and then focused. Furthermore, the size of our active area (a single 24 × 24 μm pixel) requires focusing of the blackbody to achieve an appreciable signal to noise ratio. A diagram of the

responsivity setup is given in Figure 5.7(a). A ThorLabs SLS203L blackbody is mounted on the side of the probe station. The blackbody contains a built-in lens which collimates the blackbody emission. An aperture is used to ensure that the beam falls within the spacing of an optical chopper to ensure full modulation. In this chapter, a 3.6 μm bandpass filter is used to measure the mid-wave responsivity. A 45 degree gold mirror held by cage rails redirects the 3.6 μm beam downward toward the sample housed in a ARS probe station. A zinc selenide (ZnSe) lens is used to focus the beam onto the pixel within both the DCPC and RMPC detector architectures.

The ZnSe focusing lens is deliberately placed off focus to ensure uniform illumination of the pixel, but more importantly, to minimize error with regard to the incident power calculation. Because the pixel is small relative to a focused incoherent beam, the beam spot size must be measured, fit with a double Gaussian, and then integrated within the area of the pixel to know the power incident upon the pixel. To measure the beam spot size, a razor blade is placed at a distance away from the ZnSe lens, f_{sample}, as seen in Figure 5.7(b). The razor blade is mounted on micrometers with gradations and slowly scanned over the beam which enters a separate detector of known responsivity. Because the separate detector and razor blade cannot fit within the probe station, the setup (which is on a breadboard) is moved to an optical table for beam spot measurements. The distance between the ZnSe lens and sample (f_{sample}) in the probe station is measured, and the razor blade is placed at the same distance on the optical table. Hence, the further away the sample is from the focus of the lens, the larger the beam spot and therefore the less percentage error there will be in measuring the beam spot size when transferring the setup to an optical table. On the other hand, if the sample is placed too far away from focus, there will be too little light incident

upon the pixel, thus decreasing the SNR.

Once the beam profile is fit with a Gaussian, the full-width half-maximum (FWHM) of both x- and y-directions can be extracted. Consequently, at f_{sample}, the total power of the beam, P_{beam}, can be expressed as:

$$P_{beam} = A \int_{-\infty}^{\infty} \int_{-\infty}^{\infty} e^{\frac{-x^2}{2c_L}} \cdot e^{\frac{-y^2}{2c_V}} dxdy \tag{5.4}$$

where x and y are distance units, $c_L \approx FWHM_x/2.35482$ and $c_V \approx FWHM_y/2.35482$ are Gaussian constants with a direct relationship to each respective FWHM, and A is a constant that must be solved for. The power of the entire beam, P_{beam} is measured during the spot size calculation. Since the detector in Figure 5.7(b) has a known responsivity, R_{known}, the total power of the beam can be calculated as:

$$P_{beam} = \frac{V_{LIA}}{R_{known} \cdot M \cdot T_{ND}} \tag{5.5}$$

where V_{LIA} represents the voltage on the LIA, M is the so-called modulation factor when using an LIA with a square wave reference, and T_{ND} is the transmission of a neutral density (ND) filter used to cut the power of the blackbody. The ND filter is added to ensure that the power is low enough such that the known detector is operating in a linear region. The integral of a Gaussian is well-known, so the constant, A, can now be solved for:

$$A = \frac{P_{beam}}{2\pi c_V c_L} \tag{5.6}$$

Now that all of the values in Equation 5.4 are known, the power incident upon the pixel, P_{inc}, can be computed as:

$$P_{inc} = A \int_{-l/2}^{l/2} \int_{-w/2}^{w/2} e^{\frac{-x^2}{2c_L}} \cdot e^{\frac{-y^2}{2c_V}} dxdy \tag{5.7}$$

where the size of the pixel is $w \times l$. Because we operate off-focus, the beam is typically sufficiently large compared to the pixel, resulting in a relatively constant illumination across the pixel area. So, instead of computing the integral in Equation 5.7, the following approximation for incident power can be used:

$$P_{inc} \approx A \cdot w \cdot l \tag{5.8}$$

The input, or power incident upon the pixel is now known. To obtain the output, for the DCPC, as shown in Figure 5.4, a source (Keithley 2460) drives a biasing resistor and the photoconductive element, and the output can be taken over either resistor. For the RMPC, an HP8341B RF source supplies the bias on one side of the device (which we call Port 1), and the output on the other side (Port 2) is collected by a Krytar 302A zero-bias Schottky diode power detector. The outputs for both architectures are sent to an LIA which references the chopper modulation of the blackbody, as shown in Figure 5.7(a). However, because there are cryogenic probe arms between the RF cable from the source and the probe tips at Port 1 as well as between the probe tips at Port 2 and the Schottky diode, for fairest comparison, it is necessary to compute and normalize the signal loss in probe arms.

Figure 5.8 shows the measured S_{21} RF transmission for the RF cables, cryo probe arms, and probes as well as the RF cables only. Hence, we can effectively take the difference

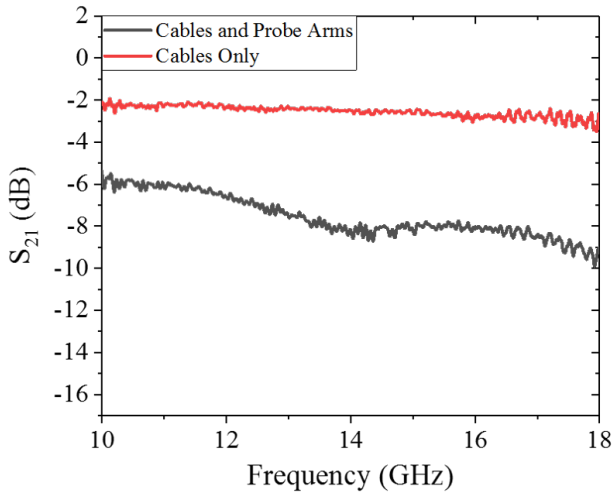

Figure 5.8: Magnitude of RF transmission (S_{21}) for the cable and probe arms (black curve) and cables only (red curve). The difference in dB yields the total loss in both probe arms

to compute the signal (in dBs) lost in the probe station *only*. We can thus scale the value on the LIA to account for the experimentally lost signal in the probe arm. Furthermore, we scale the bias on our RF source such that the bias which reaches the device is comparable to the bias supplied by the DCPC.

Since the output and input are both known, now the responsivity, or ratio between the output and input, can be computed as a function of bias as seen in Figure 5.9. Despite being a contact-free architecture, the RMPC exhibits a responsivity in excess of 150 V/W as the bias (voltage supplied by DC source for the DCPC or approximate rms voltage of the RF source incident upon the probe tips of the U-shaped coplanar pad for the RMPC) exceeds 200 mV, which is comparable to that of the DCPC. Yet, the origin of each architecture's response is somewhat different. DCPC architectures, for instance, can have large responsivities as a single generated EHP can contribute multiple times to the photocurrent resulting from

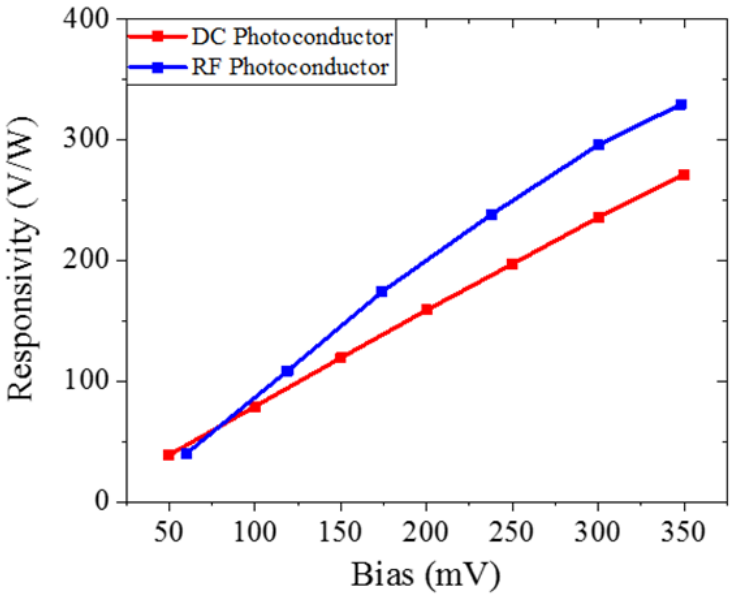

Figure 5.9: Bias dependent responsivity obtained at $\lambda = 3.6\mu$m

a so-called photoconductive gain [6][36], the origin of which has been recently debated [93]. However, the RMPC does not collect carriers or DC current; instead, the strong fields afforded by the SRR interact with the optically induced change in the pixel's AC conductivity, resulting in a significant amplitude modulation of the resonant carrier signal. Obviously, the responsivities of both the DCPC and RMPC could be improved by choice of material with a greater quantum efficiency, as more absorbed light would result in more EHPs, but the responsivity of the RMPC can also be further improved via improvements to the microwave circuit. Specifically, thicker metal, impedance matched lines, and higher quality factor resonators could improve the responsivity independent of improvements made to the semiconductor absorber. It should be noted that although the responsivity could be

improved by choice of load resistor in the DCPC, increased responsivity of the Schottky diode in the RMPC, or by increasing the bias (as seen in Figure 5.9), this cannot be done without limit. At higher biases, the material will eventually exhibit nonlinear response due to voltage-dependent mobilities [94] or dielectric breakdown [95]. However, perhaps most significantly, an increase in the drive voltage of a detector will also change the detector noise. Though thus far only detector responsivity has been discussed, the noise associated with a detector element and architecture is oftentimes the ultimate determinant of suitability for a given application. Because the responsivity can be set by a variety of factors for both architectures, in this chapter we are more interested in comparing noise characteristics; thus, for suitable noise comparison, we operate the detectors in conditions such that they possess similar responsivities.

5.2.2 Spectral Response Setup

Note that the responsivity values in the previous section were obtained at a single wavelength using a blackbody source and a 3.6 μm bandpass filter. To obtain the entire spectral response, we use a Fourier-transform infrared (FTIR) spectrometer located on an optical table next to our probe station. As seen in Figure 5.9, light from the output port of the FTIR is chopped and redirected onto the DCPC or RMPC housed within the probe station. To improve the SNR, amplitude modulation step scan (described in Chapter 2 Section 2.3.2) is used; the output from the DCPC or RMPC is sent to a LIA referencing the chopper modulation. Subsequently, the output from the LIA is sent to the digitizer of the FTIR. To calibrate out spectral weighting from the source and optics, the spectra for both DCPC and RMPC detectors were divided by a spectrum obtained (also using step scan)

with a spectrally flat pyroelectric detector. Results from the spectral response will be shown at the end, in Section 5.4.

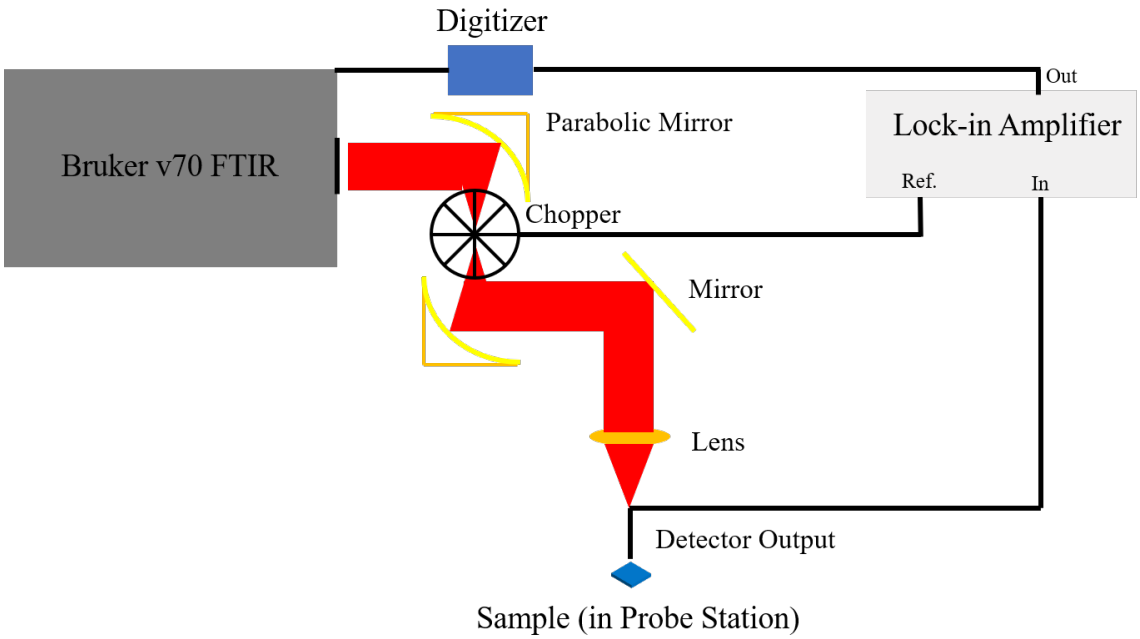

Figure 5.10: Spectral response setup; light from the spectrometer is chopped and redirected into the probe station. The output from the detector is sent to a lock-in amplifier (LIA) referencing the chopper modulation. The output is then sent back to the FTIR for digitization

5.3 Noise

Because noise is inherent to all components within a system, this section is split such that each consequent subsection considers more of the full system. To start, a brief theory of common, fundamental noise sources in standard, DC photoconductive semiconductors is given (5.3.1). For the RMPC system, we first analyze how these fundamental source of noise in the semiconductor are modified by a microwave split-ring resonator (SRR) (5.3.2).

Next, we include the noise generated by SRR in addition to the semiconductor pixel loaded within. We then consider the effects an RF Schottky diode power detector has on the noise (5.3.3). Finally, a full system noise measurement is performed (5.3.4).

5.3.1 Theory and the Johnson Limit

The total voltage noise spectral density in a photoconductor architecture can be expressed as:

$$v_{noise}^2 = v^2 \frac{A}{f} + v^2 \sum_i^n \frac{B_i}{1 + (2\pi f)^2 \tau_i^2} + 4kTR + S_{env}^2 + S_{src}^2 \tag{5.9}$$

In this expression (Equation 5.9), the total noise within the bandwidth includes five terms: inverse frequency (1/f) noise [96][97], generation-recombination (G-R) noise [98][99], Johnson/Nyquist thermal noise [100][101], pickup from environmental noise or power grids (S_{env}^2)[102], and finally, noise associated with electronics such as the source or any amplifiers employed (S_{src}^2), respectively. To obtain the total bandwidth-normalized voltage noise (in units of $V/Hz^{1/2}$ for use in a D* calculation), the square root is taken of the sum of the squared noises normalized by the bandwidth considered. To compare the noise between our two detector architectures, only the first three terms will be considered, as they are associated with the device architecture employed, and thus independent of the environment or equipment used. A qualitative plot of the first three noise terms is given in Figure 5.11(a).

The A and B coefficients refer to the strengths of the 1/f noise and G-R noise, respectively, and can be determined experimentally by fitting a noise spectrum [103]. However, for simplicity, approximations are typically made to more easily calculate the total noise: firstly, the 1/f noise is often neglected as detectors are operated at a sufficiently high frequency

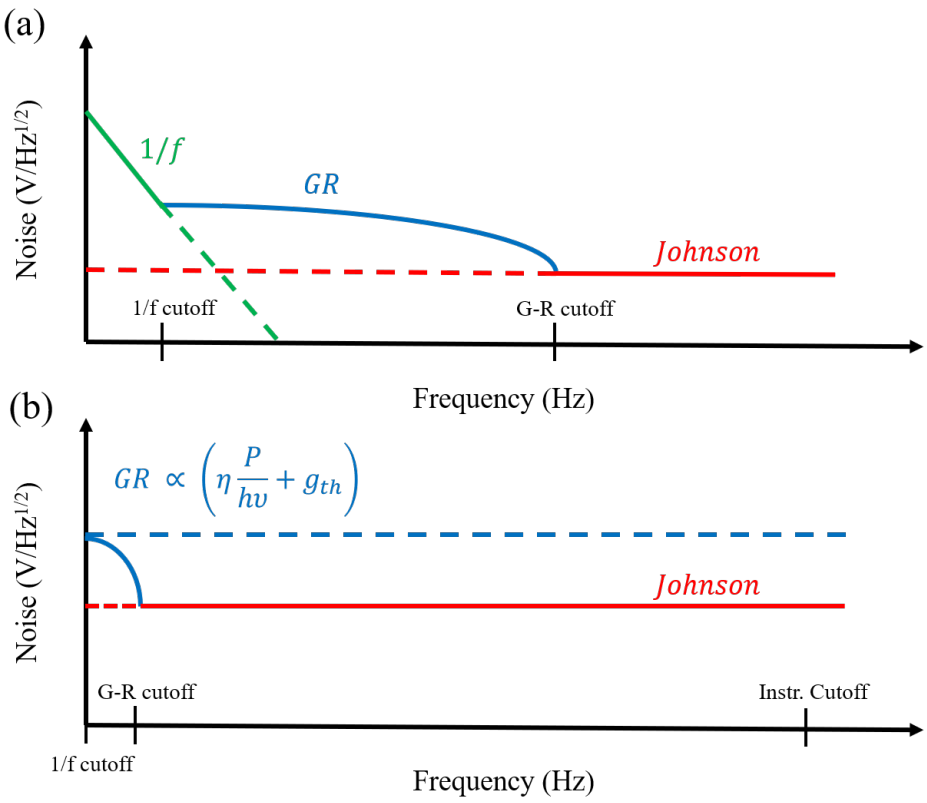

Figure 5.11: Noise sources intrinsic to photoconductors; (a) shows 1/f noise (green), generation-recombination (GR) noise (blue), and Johnson noise (red); (b) scenario in which the instrument's bandwidth exceeds the detector bandwidth, resulting in a predominantly Johnson-limited case

and modern-day sample preparation techniques help minimize 1/f noise from contacts and surfaces [104]. The two remaining sources of noise are the G-R noise and the Johnson noise. G-R noise arises from fluctuations in the semiconductor generation/recombination statistics, and thus the number of free carriers. In Equation 5.9, the summation in the G-R noise term is over the n ground to excited state transitions in the photoconductor, where τ_i refers to the lifetime of the i^{th} transition, and the net sum of the fluctuations from each transition gives the total G-R noise. Johnson noise, on the other hand, is a result of the

thermal 'agitation' of free carriers and results in a nonzero rms voltage when measuring over any resistive or power dissipative element. For the Johnson noise term, k is the Boltzmann constant ($1.3810^{-23} m^2 kg s^{-2} K^{-1}$), T is the absolute temperature (K), and R is the resistance (Ω). A common metric for photoconductors, known as the Johnson-limited D*, uses only the Johnson noise in the calculation of the D*, assuming that the Johnson noise dominates the G-R noise. To determine qualitatively the conditions in which such a situation applies, we can use an approximate expression for the G-R noise in a DC photoconductor assuming a single transition [36]. The total voltage noise spectral density then becomes:

$$v_{noise}^2 = 4qG^2R^2(\eta\frac{P}{h\nu} + g_{th}) + 4kTR \tag{5.10}$$

with g_{th} the thermal generation rate of carriers, q the charge constant, η the quantum efficiency, P the power of the incident radiation, $h\nu$ the energy of the incident photon, and G the photoconductive gain. To justify the use of the Johnson limit, the detector must operate in conditions such that 4kTR has an appreciable contribution to the total noise. Note that to obtain the first term in Equation 5.10 from the general expression given in Equation 5.9, we assume that the detector is operated well within its bandwidth such that $f << 1/\tau$. More comprehensive derivations and expressions for G-R noise are given in [98][99], but we use Equation 5.10 to intuitively determine situations in which the Johnson noise term becomes significant (or dominant).

From Equation 5.10, it becomes apparent that under low irradiances (which is often the case for IR detection), small values of photoconductive gain (and hence lower bias voltages to minimize power consumption), and/or low thermal generation rates (when the

bandgap is sufficiently greater than kT and when the active area is small, such as in a micro-scale pixel), the Johnson noise can potentially become a significant component to the overall noise. In the case of the DCPC, for a given geometry, material resistivity, and temperature, a minimum, fundamental Johnson white noise is always present across all frequencies and operating conditions, suggesting that the Johnson limit is the best-case scenario for noise considerations; furthermore, in practice, when the bandwidth of any instrument (such as an oscilloscope) used with the detector significantly exceeds the detector bandwidth (and hence the G-R noise cutoff) as seen in Figure 5.11(b), the total integrated noise measured can be predominantly Johnson in origin.

Thus far, we have described fundamental noise common to DC photoconductors. However, as will be discussed next in Subsection 5.3.2, when the photoconductive semiconductor pixel is coupled to a microwave SRR, we have a much more interesting case!

5.3.2 Time Domain Modeling of Noise Sources Within Resonators

To qualitatively evaluate and compare how a generic microwave resonator modifies different sources of noise coming from the reactively-coupled pixel, we model the simple circuits in Figure 5.12 using LTspice, an open-source circuit simulator. The circuit is solved in the time domain, and a fast Fourier transform of the solution allows us to see how the noise is modified in the frequency domain. First, the Johnson thermal noise is considered, modeled as an independent Thevenin incoherent white noise voltage source placed in series with the pixel resistance, shown in Figure 5.12(a). It's seen in Figure 5.12(b) that even though a white noise source is supplied (black line), the resonator effectively functions as a filter, shaping and suppressing the white noise and only allowing signal around the resonant

frequency to efficiently transfer to the output.

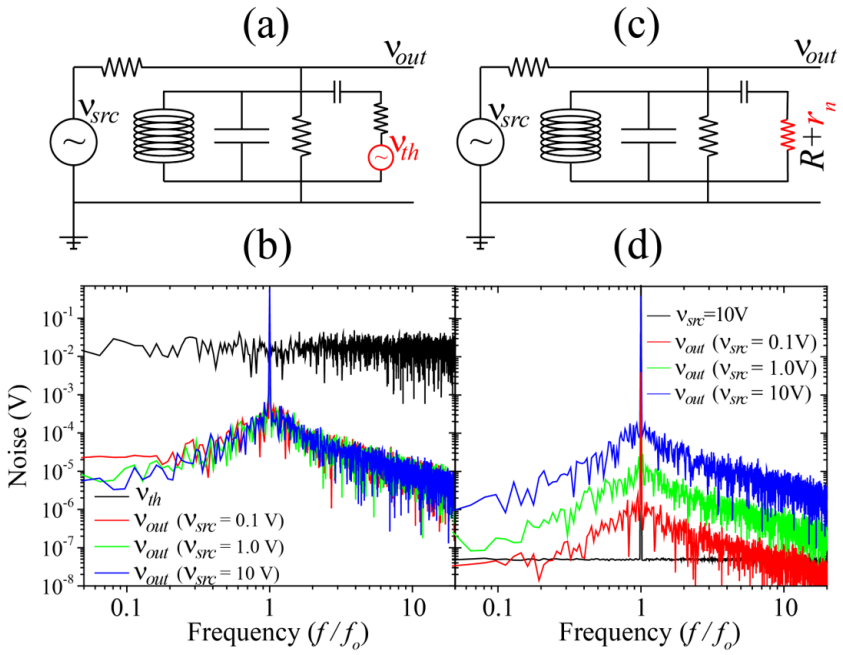

Figure 5.12: (a) Circuit schematic for Johnson noise (modeled as a Thevenin white noise source placed in series with the detector). (b) Output voltage spectra for source voltage amplitudes of 0.1 V (red), 1 V (green) and 10V (blue) given a fixed thermal noise spectrum (black). (c) Circuit schematic for G-R noise [modeled as a white noise function (r_n) added to pixel resistance (R)]. (d) Voltage output spectra plotted for fixed amplitude r_n and source amplitudes of 0.1 V (red), 1 V (green) and 10V (blue), as well as the voltage spectrum from the source itself. In both models the circuits are driven on resonance, with the spectra normalized to the resonant frequency, f_0

A similar observation is made when considering noise resulting from the fluctuation of total free carriers (such as G-R noise), which is modeled as a fluctuation in the resistance by adding white noise to the resistance value, as shown in Figure 5.12(c). However, the primary distinction between the two different types of noise is with regard to their dependence on the driving source voltage. The G-R noise, for instance, depends on the voltage that drops over its source (the pixel resistance, in this case), resulting in a source

amplitude dependent spectrum, as we see in Figure 5.12(d). Hence, intuitively, anything done to decrease the G-R noise contribution (such as decreasing the driving voltage), will also decrease the responsivity since both scale with the pixel resistance. This ultimately suggests that for a given material and active area, the resonator architecture provides no real advantage over the DCPC in terms of noise related to fluctuations in the detector resistance, such as G-R noise. The Johnson thermal noise, on the other hand, can be modeled as an independent voltage source that remains unmodified by the amplitude of the driving source, as seen in Figure 5.12(b). Because of this, the resonator inherently suppresses and filters some of the Johnson noise irrespective of the driving source. Thus, the RMPC naturally benefits from lower Johnson thermal noise from the pixel, although the exact amount of reduction depends on the characteristics of the resonator as well as the bandwidth considered around resonance, as the Johnson noise is no longer spectrally flat once it is effectively filtered by the resonator. However, it is worth noting that thus far, we have only considered modifications to the noise generated by the pixel. In the next subsection (Subsection 5.3.3), the effects of the SRR as well as the Schottky diode power detector will be considered.

5.3.3 Johnson Noise of the Coupled Pixel-Resonator System

Even though the SRR can suppress Johnson noise from the semiconductor pixel, the resonant circuit itself can contribute to the Johnson noise as anything which can dissipate power exhibits Johnson noise. This suggests that a true reduction in noise is only achieved when the noise of the resonant circuit is less than the Johnson noise of the pixel in the DCPC. Because the resonant circuit has a complex impedance, we modify the Johnson

noise spectral density equation appropriately as:

$$v_J^2 = 4kT \cdot Re\{Z_{in}\} \tag{5.11}$$

where we have replaced the resistance, R, in Equation 5.10 with the real part of the input impedance, Z_{in}, for the entire circuit. Furthermore, since Z_{in} is a function of frequency, the total Johnson noise for the RMPC depends on the frequency band ($\Delta f = f_2 - f_1$) considered:

$$v_J^2(\Delta f) = \frac{\int_{f_1}^{f_2} v_J^2(f)df}{f_2 - f_1} = 4kT \cdot \frac{\int_{f_1}^{f_2} Re\{Z_{in}\}df}{f_2 - f_1} \tag{5.12}$$

Clearly from Equations 5.11 and 5.12, to compute the Johnson noise, the input impedance, Z_{in}, must be known as a function of frequency. Because the RMPC circuit is both reciprocal and symmetric ($S_{21} = S_{12}$ and $S_{11} = S_{22}$), a T-model can be used to describe the two-port network [8], as shown in the blue dashed box of Figure 5.13.

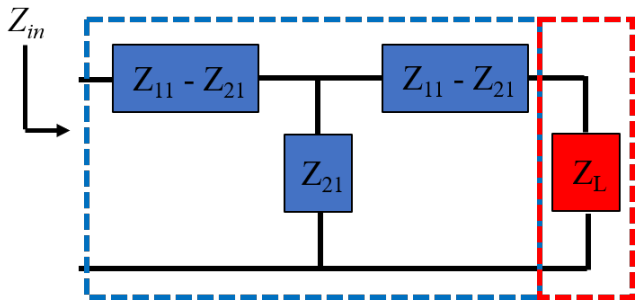

Figure 5.13: Effective input impedance of the circuit; blue dashed lines represent the T-model used to model a symmetric, reciprocal two-port network, and the red dashed lines refer to the terminating load, Z_L (which we assume to be 50 Ω representative of the Schottky diode impedance). With the right side terminated, the effective input impedance, Z_{in}, can be computed

From Figure 5.13, once the T-model for the two-port network (blue dashed lines) is terminated with a load (red dashed lines), an effective input impedance can clearly be computed as:

$$Z_{in} = [(Z_{11} - Z_{21} + Z_L)||Z_{21}] + (Z_{11} - Z_{21}) = Z_{11} - \frac{Z_{21}^2}{Z_{11} + Z_L} \tag{5.13}$$

where Z_{11} and Z_{21} are the Z-parameters described in Chapter 2 Section 2.2.1, which are computed from S-parameters measured with a vector network analyzer (VNA) using Equations 2.22 and 2.23, respectively. Figure 5.14 shows the total Johnson noise generated by the coupled pixel-SRR system using Equation 5.13.

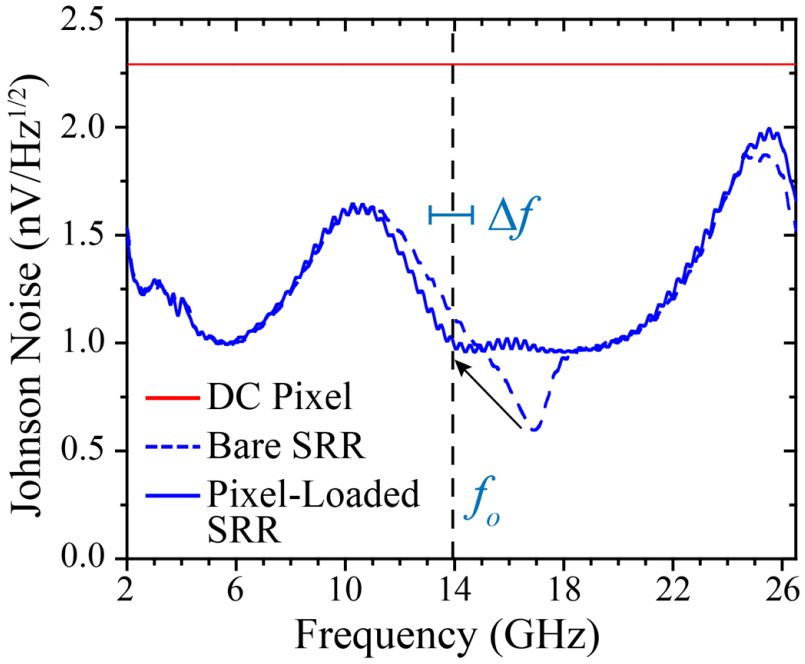

Figure 5.14: Johnson noise of bare SRR (black curve) and pixel-loaded SRR (blue curve) computed using Equation 5.13 and DC pixel (red dashed lines) using 4kTR, where R = 300 Ω from Figure 5.4(a-iv)

The Johnson noise in Figure 5.14 accounts for the 50 Ω input impedance of the Schottky diode as it terminates the T-model in Figure 5.13; however, the implications of using a Schottky diode power detector have yet to be considered. In the square-law region of the Schottky power detector, the actual output voltage of the power detector is proportional to the input power. Thus, the total output voltage from the Schottky diode can be intuitively determined as follows:

$$v_{sch} \sim P_{in} = X(v_{sig} + < v_{nJ} >)^2 \tag{5.14}$$

where v_{sch} is defined as the output voltage of the Schottky diode, v_{sig} the signal voltage, $< v_{nJ} >$ the rms Johnson noise voltage within a bandwidth, Δf, and X is a proportionality constant. The frequency range over which the Johnson noise is integrated over for the RMPC architecture depends upon the bandwidth of the output of Port 2. However, because both the optical modulation and noise read out with the resonant carrier, a filter placed on resonance, f_0, with a bandwidth Δf, can be considered. If the bandwidth is small compared to the resonant carrier:

$$< v_{nJ}^2 > \approx v_J^2(f_0)\Delta f \tag{5.15}$$

For our RMPC, the resonant frequency is approximately 13.7 GHz, which, referring to Figure 5.14, $v_J(13.7) \approx 1nV/Hz^{1/2}$. Note that if instead, Δf is not significantly less than the carrier frequency, the noise spectral density in Figure 5.14 must be integrated over the bandwidth to determine $< v_{nJ} >$. Referring to Equation 5.14, because the signal voltage is much larger than the noise voltage, the output noise will be dominated by the cross-term

between the signal and rms Johnson noise rather than the square of the rms Johnson noise [105][106]. This suggests that although the Johnson noise generated by the input impedance of the terminated T-model is independent of bias, once the noise multiplies with the signal in the Schottky diode, a bias dependent scaling factor, $2X \cdot v_{sig}$, will multiply with the Johnson noise, $< v_{nJ} >$. This scaling factor is related to the responsivity of the Schottky diode power detector, R_{sch}, which determines the output voltage, v_{sch} per input power, P_{in}; thus, the X value can be measured by comparing the output voltage received for a known input RF voltage. At moderately low received signal powers, the Schottky diode will have a constant responsivity, which will begin saturating as the bias is increased. Hence, the scaling factor, X, must be measured as a function of received signal. Once known, the total integrated rms Johnson noise seen at the output of the Schottky (which we denote v_{totJ}, $2X \cdot v_{sig} \cdot \sqrt{v_J^2(f_0)\Delta f}$, can be obtained.

However, as mentioned in Subsection 5.1.4, for D* calculations, the total rms noise is normalized by the bandwidth considered to provide insight into the detector's inherent noise independent of bandwidth filtering components used. Thus, the bandwidth normalized Johnson noise will simply be $v_J(13.7) \approx 1.0nV/Hz^{1/2}$ multiplied with the scaling factor, $2X \cdot v_{sig}$. In Figure 5.15, we can compare this computed value (blue dashed curve) to the calculated noise of the plain pixel, $4kTR$ (red dashed curve), and note nearly a factor of three more noise from the DC pixel. Finally, combining the bias dependent responsivities from Figure 5.9 with the bias dependent Johnson noise (dashed lines in Figure 5.15), the Johnson limited D* at $\lambda = 3.6\mu m$ can be obtained as a function of bias, as seen in the solid lines of Figure 5.15. At the low bias of 100 mV, while the responsivities between the DCPC and RMPC architectures are nearly identical, the D* of the DCPC ($\approx 1 \times 10^8$) is nearly a

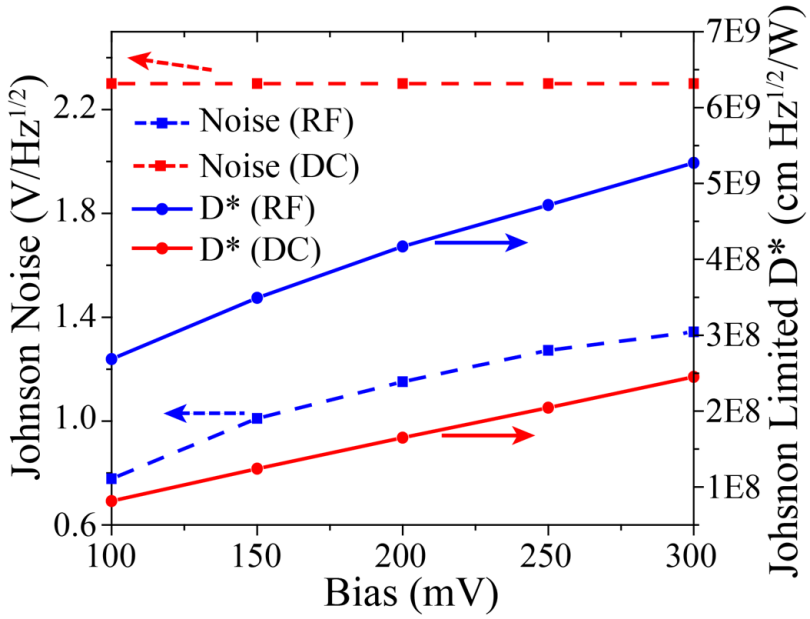

Figure 5.15: Bias dependent Johnson noise (dashed lines) and D* at $\lambda \approx 3.6\mu m$ (solid lines) for both the RMPC (blue) and DCPC (red)

factor of three less than that of the RMPC due to the larger noise associated with the DCPC architecture.

5.3.4 Noise Measurement Setup

The noise in Subsection 5.3.3 considers calculated Johnson noise from measured impedance values to determine the noise inherent to the architecture. However, to consider the system as a whole, noise measurements on both detection architectures were performed to determine limiting factors in practice. The setup used to make the measurements is shown in Figure 5.16(a). A Zurich UHF LIA equipped with a noise sweeper allows for input noise measurements up to 600 MHz. In order to ensure the measured noise from the DCPC and RMPC detector architectures is greater than the noise floor of the noise sweeper,

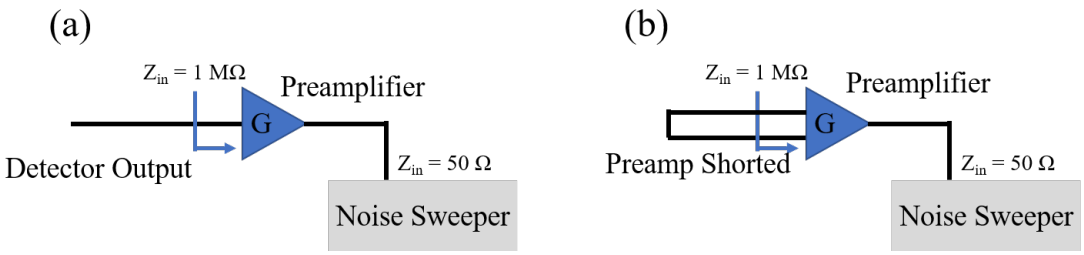

Figure 5.16: Schematic of the noise measurement setup; (a) output of the detector enters a low noise preamplifier (LNP) which is then sent to the noise sweeper tool. To subtract the noise from the LNP, (b) a noise spectrum is taken with the input of the LNP shorted

the output from each respective detector is first sent to a Femto HVA-200M-40-F low noise preamplifier (LNP) with a known voltage gain, G. The LNP has a high input impedance to ensure that no loading of the detector architecture occurs on the input side. To obtain the total noise from the device only, v_{ndev}, we take the squared noise spectra obtained from all components using the configuration in Figure 5.16(a), v_{nall}, and subtract the squared noise obtained from the amplifier only, which is measured by shorting the input, as seen in Figure 5.16(b), and is expressed as v_{nshort}. After a square root is taken, this value represents the total *amplified* noise from the device only; thus, the amplification or gain of the LNP must be divided by. The measured noise of the device only can therefore be expressed as:

$$v_{ndev}(f) = \frac{\sqrt{[v_{nall}(f)]^2 - [v_{nshort}(f)]^2}}{G} \tag{5.16}$$

The results from the noise measurements are shown in Figure 5.17. We find that similar noise spectra are obtained between the RMPC and the source straight into the Schottky (without the SRR or pixel) diode power detector. This suggests that in practice, the measured noise does not come from the device, but rather from the source or environment

in which we measure in. A similar observation is made for the DCPC; we note a decrease in measured noise when we drive the system with an off-the-grid battery. Because of a source or environment-dominated noise response, the Johnson limited noise described in Figure 5.15 will be used for a D* calculation as it is more representative of the detector architectures independent of equipment used or environment measured in.

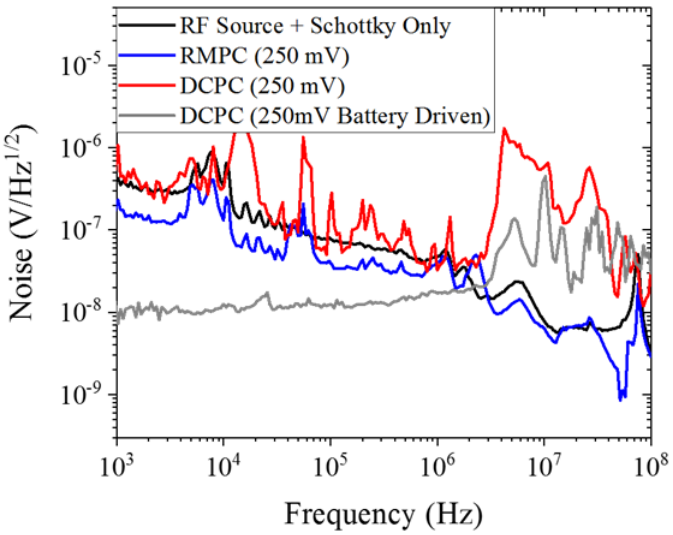

Figure 5.17: Noise measurements with approximately 250 mV bias performed on: the RMPC system (blue curve), RF source and Schottky diode only (black curve), DCPC system (red curve), and DCPC system driven with a battery (gray cure)

5.4 Discussion of Architecture Performance

Using the Johnson noise given in the left axis values of Figure 5.15, Equations 5.2 and 5.1 can be applied to compute the D* at $\lambda = 3.6\mu m$ as a function of bias, which is given on the right axis of Figure 5.15. By taking a spectral response (described in Subsection

5.2.2) and scaling the response to the D* computed at $\lambda = 3.6\mu m$, the spectral D* can be plotted, as seen in Figure 5.18.

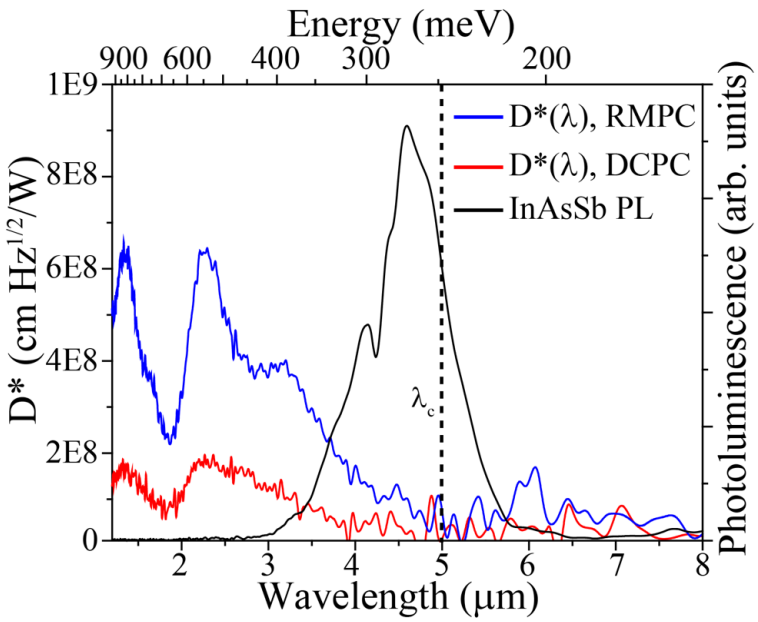

Figure 5.18: Room temperature Johnson-limited spectral D* for both DCPC (red curve) and RMPC (blue curve) detector architectures at a 100 mV bias; the room temperature photoluminescence is also plotted (black curve) for reference

The D* values for both RMPC and DCPC architectures are between 10^8 and 10^9, which is comparable to room temperature mid-wave D* values in the literature [74][107][108]. Nonetheless, there remain opportunities for further improvement of the detector performance. The shape of the D* spectra in Figure 5.18, with stronger response at higher energies despite the fact that fewer EHPs are generated per unit power, suggests that the pixel material is not absorbing all of the incident mid-wave IR radiation. Thus, thicker pixels or material with stronger absorption could generate more EHPs and further increase the D* value. In addition, materials with stronger absorption coefficients or longer lifetimes

could improve the photoconductive detector response. However, doing so would improve both DC- and RM-PC architectures. In addition to material optimization, the RMPC could be improved even further by utilizing shorter matched microstrip lines, thicker metal, and higher quality factor resonators. Furthermore, from Figure 5.14, it's clear that loss and loading from the pixel significantly increases the noise generated on resonance. If more resistive materials, such as the lead salts, were coupled into the RMPC, the overall Johnson noise generated by the loaded SRR could be reduced. Notably, the use of more resistive materials would increase the Johnson noise ($4kTR$) of the DC system.

In conclusion, we provide a proof-of-principle for a contact-free mid-IR detection architecture. We demonstrate comparable responsivities with a standard DC photoconductor made with the same active material. Noise simulations suggest that a resonator can shape and suppress Johnson noise generated by a semiconductor material placed within. Even when considering Johnson noise generated by the loaded SRR circuit as well as the effects of using a Schottky diode power detector, the total Johnson noise is still less than that of a DCPC. Overall, the Johnson-limited D* is more than three times greater for the RMPC when compared with the DCPC, and we highlight future scenarios in which the improvement could be even more significant.

Chapter 6

Conclusion

6.1 Future Work

In this section, future work is suggested based on conclusions drawn from the previous chapters. As such, the work presented in this section is currently in progress at the time of writing this dissertation.

6.1.1 Loaded PCB Resonators

In Chapter 4, a contact-free lifetime characterization technique was presented for micro-scale materials. The SRRs used in this section were Ku band resonators with side lengths less than 1 mm. Thus, the SRR capacitive split-gap was sufficiently small (micron-scale), allowing for transfer of micro-scale materials. However, to apply this technique to mm-scale cleavable pieces of semiconductor material or large-scale patterned nanostructures, larger resonators would be required such that the split-gap is on the order of < millimeters instead of tens of microns. Although for large-scale areas, the time-resolved microwave reflectance (TMR) technique described in Chapter 4 could also be used, a large-scale TRMRR technique is still potentially simpler and less expensive than TMR as it would not require a waveguide or circulator.

Furthermore, as seen in Figure 6.1, the PCB resonators would alleviate requirements

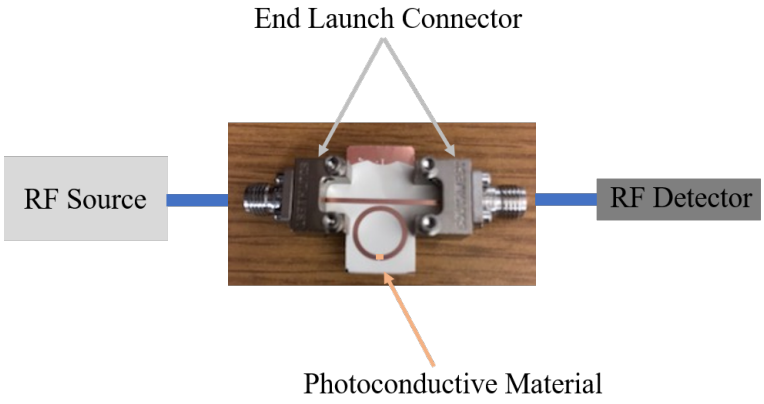

Figure 6.1: Proposed PCB resonator platform used for contact-free characterization and detection using larger-area patterns of active material

for probes as commercial end launch connectors could directly connect to the microstrip. Thus, without probe pitch considerations, using Equations 1.11 or 1.13, the width of the microstrip can be designed such that the characteristic impedance is better matched at 50 Ω. PCB board technology is also commercially mature; hence, they can be purchased with half-ounce copper (approximately 17 μm thick) already plated on both sides. With the additional design flexibility, the D* of our RMPC detectors could be further improved with optimizations made to the circuit.

6.1.2 Photodoped ENZ Ultra-Thin Microstrip Waveguides

Several well-known techniques for characterizing material properties (such as permittivity or loss tangent) across the microwave spectrum exist. Three commonly used methods are: dielectric probing, loaded transmission lines, and loaded resonators. Dielectric probing is a broadband technique in which the material under test (MUT) is directly in contact with a probe of known characteristics attached to a vector network analyzer

(VNA). While this technique is useful for a variety of material types (including liquids), the dielectric probes can be significantly expensive (occasionally even more so than the VNA itself) and also requires excellent physical contact with the MUT. Alternatively, a material could terminate a transmission line or load a waveguide. By comparing loaded to unloaded S-parameters, material constants could be extracted. While this technique is broadband and waveguides are nominally cheaper than the dielectric probes, the method would not be well-suited for small, micro-scale materials. It was demonstrated in Chapter 4.9 that a resonator could concentrate the field to improve interaction with micro-scale materials. However, the use of a resonator would not work for broadband microwave material parameter characterization as the resonator is only active at discrete, resonant frequencies.

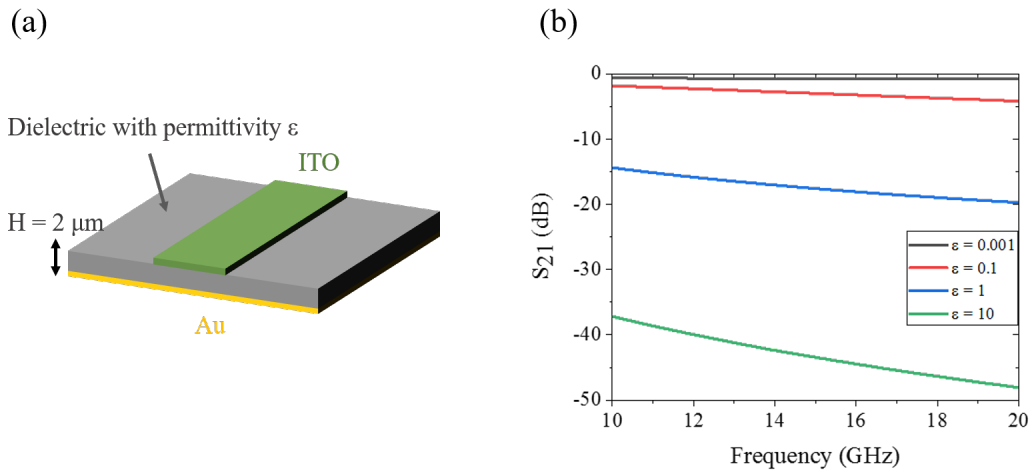

Figure 6.2: (a) Diagram of simulated microstrip waveguide with an ultra-thin (2 μm thick) dielectric layer; (b) simulated S_{21} parameter plotted with different permittivities

In order to accurately probe the microwave properties of micro-scale materials, we would ideally want a broadband microwave waveguide/transmission line that can also confine fields to micro-scale volumes. Referring to the microstrip impedance Equations

1.11 and 1.13, if the thickness of the insulating layer of the microstrip is significantly decreased in an attempt to strongly confine fields, to retain a matched 50 Ω impedance, the permittivity must also be decreased. In the extreme case, for an ultra-thin insulating layer, the permittivity must also go to zero. To demonstrate this, using HFSS, we simulated the S_{21} (transmission) of a simple microstrip with an ultra-thin (2 μm) insulating layer and gradually reduced the permittivity, as seen in Figure 6.2(b). As expected from the microstrip impedance equations, we found that for an ultra-thin microstrip, the transmission is only appreciably large when the permittivity is near zero, allowing for a matched impedance.

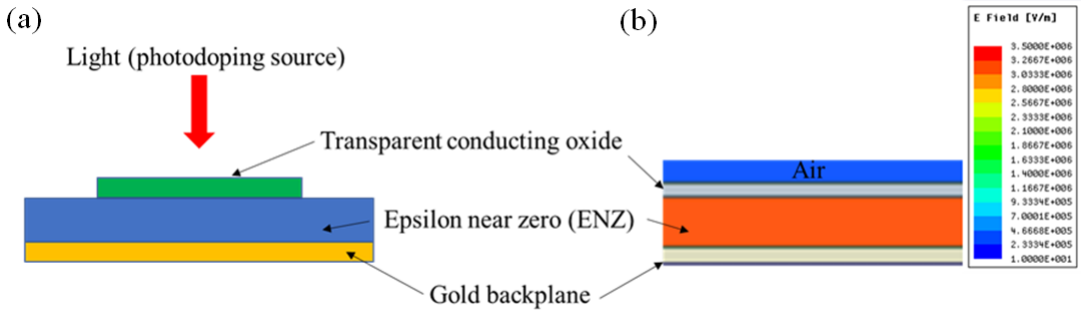

Figure 6.3: (a) Cross-sectional diagram of the layers in the simulated structure; (b) cross-sectionnal view of the simulated electric field magnitude

Furthermore, to demonstrate field confinement in the thin ENZ layer, we also simulate the electric field magnitude of the microstrip cross-section, as seen in Figure 6.3. Although we see strong field confinement in the ENZ layer, it must be noted that the simulation results in both Figure 6.2 and Figure 6.3 are best-case scenarios; at the time of writing this dissertation, these simulations only consider the ENZ layer as a dielectric with a permittivity and do not currently include loss tangents. Furthermore, the value we use for the conductivity of the ITO is industry-grade, which may not be representative of what we

are capable of depositing. Thus, in actual devices, we expect both the field confinement and S_{21} parameter to be lower than what is simulated; to determine by exactly how much, we are currently working on updating the simulation by computing and adding the dielectric loss tangent as a function of frequency as well as extracting a conductivity value for the ITO films we are able to deposit.

To implement the proposed ENZ structure, we are fabricating a photodoped epsilon-near-zero (ENZ) ultra-thin (2 μm thick, significantly below free-space microwave wavelengths) microstrip waveguide, shown schematically in Figure 6.2(a). To achieve ENZ in the insulating layer, an optical excitation pumps through an optically transparent (but electrically conductive) tin-doped indium oxide (ITO) layer, generating free carriers in the insulator underneath. If the laser power is tuned such that the resulting permittivity is near zero at RF frequencies, the microstrip could be impedance matched to 50 Ω and guide a wave despite being ultra-thin. Furthermore, considering a Drude permittivity model [67], the real part of the permittivity, ϵ, can be expressed as:

$$Re(\epsilon) = \epsilon_\infty \left(1 - \frac{\omega_p^2}{\omega^2 + \gamma^2}\right) \tag{6.1}$$

where ω_p is the plasma wavelength, ω is the angular frequency of the electromagnetic wave exciting the material, and γ is the scattering rate for free carriers in the material. If the scattering rate is much greater than the frequency, we have an interesting situation in which the permittivity is relatively constant over a frequency bandwidth. Thus, if the laser power is tuned such that the plasma frequency created via photodoping results in a broadband ENZ (note that while the actual zero crossing only occurs at one frequency, a

permittivity *near* zero would be broadband) at GHz frequencies, a broadband ultra-thin microstrip could be produced. Such a structure could potentially allow for broadband microwave characterization of micro-scale materials placed on the edge of the waveguide, effectively terminating the waveguide as a load.

Currently, we are in the process of fabricating the device shown in Figure 6.2. A schematic of the fabrication steps is given in Figure 6.4. Two microns of undoped gallium arsenide (GaAs) on top of a 200 nm aluminum gallium arsenide ($Al_{0.55}Ga_{0.45}As$) etch stop layer is grown by my labmate Leland Nordin via molecular beam epitaxy on a three-inch GaAs wafer, which is then cleaved into 1 cm $\times$ 1 cm pieces. Using an electron beam evaporator, 10 nm of titanium followed by 250 nm of gold are evaporated on the front side of the GaAs sample as well as a silicon handle piece slightly larger (approximately 1.3 cm $\times$ 1.3 cm) than the cleaved GaAs piece. This gold layer will serve as both the bonding layer between the GaAs sample and silicon handle as well as the ground plane of the ultra-thin microstrip. The GaAs sample is wafer bonded to the silicon handle wafer (via gold-gold bonding) at 400 degrees Celsius using 300 Newtons of force for 20 minutes. The GaAs substrate is then lapped down to approximately 100 μm using 600 grit lapping paper. The remainder of the substrate is etched using a 5:1 citric acid:hydrogen peroxide solution. Once the GaAs substrate is removed and the AlGaAs etch stop layer is reached, the surface becomes shiny, and rainbow-colored fringes appear due to oxidation of the layer.

At the time of writing this dissertation, the above mentioned steps (steps 1 - 5 as described in Figure 6.4) have been completed. From here, the AlGaAs etch stop will be removed using a quick hydrofluoric acid (HF) dip, exposing the grown undoped GaAs (the layer that will be photodoped). However, because these devices will be probed using

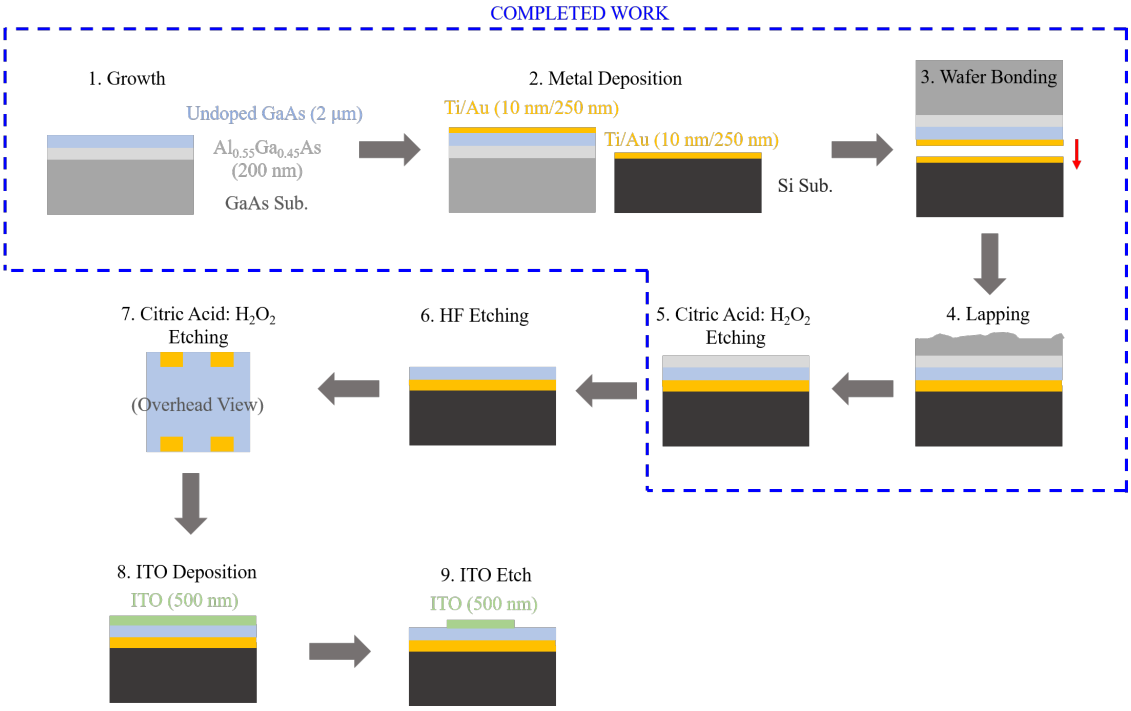

Figure 6.4: Fabrication steps for structure given in Figure 6.2(a). Steps within the blue dashed lines have been completed thus far

ground-signal-ground (GSG) probes as done in Chapters 3, 4, and 5, a small section of the undoped GaAs must be etched to expose part of the deposited Au ground plane for the ground probes, as seen in step 7 in Figure 6.4. Finally, the ITO is deposited and etched to form the microstrip.

6.2 Summary

The aim of this dissertation was to demonstrate and apply the utility of microwave resonant structures toward mid-infrared optoelectronic materials characterization and light detection. In Chapter 3, the microwave mapping by optically induced conductance

(MMOIC) technique was introduced as a method for characterizing relative field distributions in Ku-band sub-millimeter scale split-ring resonators (SRRs) capacitively coupled to a microstrip busline. Field profiles were mapped using conductance induced by a focused laser, allowing for mapping with a resolution orders of magnitude less than the free-space RF wavelength. It was demonstrated that the strongest fields were found in the capacitive split-gap of the SRR when driven on resonance.

Using the field distribution knowledge gained in Chapter 3, a micron-scale indium arsenide antimonide (InAsSb) pixel was loaded into the split-gap of the SRR. By taking advantage of the strong, confined fields, we develop and demonstrate a proof-of-principle of the micro-scale time-resolved microwave resonator response (μ-TRMRR) technique, a contact-free method capable of measuring carrier lifetimes in micro-scale materials. Results from the proposed μ-TRMRR technique were compared with standard time-resolved photoluminescence (TRPL). It was shown that the μ-TRMRR can obtain a comparable response with TRPL using greater than 10^5 less energy per laser pulse. Furthermore, the technique was applied to monolayer WS_2, demonstrating an extension to micro-scale 2D materials.

In Chapter 5, the coupled pixel-SRR was evaluated as a candidate for infrared detection. The resonant microwave photoconductor (RMPC), despite being a contact-free detector architecture, could match the responsivity of a statndard direct current photoconductor (DCPC). Additionally, a noise analysis of the RMPC detectors was performed, and it was found that while the resonator did not provide an advantage in terms of generation-recombination (G-R noise), the SRR was still able to suppress and filter Johnson thermal noise generated by the pixel. Even when considering Johnson noise generated by the loaded

SRR, the overall Johnson noise was nearly half that of the DC pixel. Furthermore, after considering the effects of the Schottky diode, a Johnson limited D* at $\lambda = 3.6\mu m$ for the RMPC was computed at low bias to be 3×10^8, which is approximately a factor of three greater than that of the DCPC.

In conclusion, the results generated by this dissertation seek to motivate and encourage further work in the exciting field of RF-photonics, especially in the field of mid-infrared detection and materials characterization.

Appendices

Appendix A

An Experimentalist's Handbook

In this Appendix, further setup details and troubleshooting assistance is provided for some of the experimental techniques outlined in the dissertation.

A.1 Photoluminescence

Laser details: For the photoluminescence (PL) setup used in this dissertation (described in Figure 2.15), a 980 nm laser outputting approximately 70 mW of power is used. The laser is a Thorlabs L980P100 laser diode mounted in a TCLDM9 mount.

Optical setup: The focusing lens used is a half inch diameter calcium fluoride lens. The PL collecting lens is a two inch diameter, three inch focal length germanium lens. Zinc selenide windows on the cryo (which houses the samples) are used. The Bruker V80 FTIR spectrometer uses a KBr spectrometer for these measurements, and a liquid nitrogen cooled MCT detects the sample PL.

Some alignment tips: To align the PL setup, first place a well-known strongly emitting calibration sample in the cryo. If the laser is a NIR laser, place an IR card inside the cryo above the sample. First, focus the laser onto the IR card such that the beam is clearly visible. With a straight edge, check to ensure that the visible beam is within the center of the FTIR spectrometer's input window. Using a ruler, coarsely adjust the height

of all the optics to match the height of the center of the input window. Next, move the laser beam onto the calibration sample. The germanium lens will be the most coarse/sensitive component in the alignment; thus, move the germanium lens until the signal is maximized. Clamp the germanium lens and then very carefully adjust the height of the lens to continue maximizing the signal. Move the lens again. Clamp and adjust the height again. Iterate until tired, and then iterate twice more to account for laziness.

Troubleshooting:

1. No signal (at all): If the bright calibration sample is housed in the chamber and no signal is obtained, it is usually not an alignment issue; double check the Optics tab and ensure that the source input is listed as the backside (or whichever port used) and detector is set as DCIN (if using step scan). Run a test scan (which can be cancelled as soon as the progress bar reaches 1%) to ensure the settings are applied. Ensure the MCT is cooled. Double check the LIA connections; the AC out from the FTIR should go into the input of the LIA and the output of the LIA should go to the DC in of the FTIR. Check that nothing is placed within or blocking the sample compartment.

2. Very weak signal: While this could be related to poor alignment, double check the sample compartment and make sure no accessories or filters are placed within the sample compartment.

3. A signal is present on the LIA but the spectrum is all noise: Ensure that the output from the LIA goes to the DC input of the FTIR. If the problem persists, restart the FTIR (both hardware and software).

4. Laser diode shows open circuit: This usually occurs when the laser diode is either not

installed in the mount properly or the AG/CG grounding pins located on both the driver and on top of the mount are set incorrectly. Refer to the manual for the particular laser diode for installation/setup instructions.

A.2 Time-Resolved Photoluminescence

Laser details: There are two lasers that are used in the lab for TRPL (shown schematically in Figure 2.16). The first is a 1064 nm, 1 ns pulse width, 6.8 μJ energy per pulse, 10 kHz repetition rate laser. Alternatively, we have a 532 nm, 1 ns pulse width, 1 μJ energy per pulse, 20 kHz repetition rate laser.

Optical setup: The setup is shown in Figure 2.16. The window on the cryo is a ZnSe window. A two inch diameter, six inch focal length parabolic mirror is used to collect and collimate the light, and a two inch diameter, three inch focal length germanium lens focuses the light onto the MCT. In the future, if the setup it ever taken down, I would recommend using a shorter focal length parabolic to collect more light. The high speed MCT detector used has a 250 μm $\times$ 250 μm area and a cutoff wavelength < 11 μm. The rise time of the MCT is approximately 4 ns, and the bandwidth is 80 MHz. The output of the detector is sent to a LeCroy Waverunner 600 MHz bandwidth oscilloscope. Typically, the maximum sampling rate is used; furthermore, an enhanced resolution functional filter (eres) can be used to to improve the signal to noise ratio (SNR). Typically, 2 bits is the maximum number of eres bits that can be used before the time resolution is affected for this particular system. That being said, I would recommend the eres only be used by experienced users. The oscilloscope impedance is set to 50 Ω to match the cable impedance and avoid reflections.

Alignment tips: This alignment can be rather difficult and should be done in multiple

steps if working from scratch. I would recommend taking a strongly emitting sample (with a known lifetime, such as the bulk InAsSb sample) and placing it in the cryo next to an IR card. The first step is to align the parabolic mirror (collection optic) and germanium lens (focusing optic) to each other. Instead of the high-speed MCT, initially, use a more sensitive, larger active area MCT (such as our Judson MCT detector or the InSb detector) to more easily find a signal. Pump the sample with a 980 nm electrically modulated laser (similar to the one in the PL setup) so an LIA can be used (the LIA does not work well with the ns pulsed lasers). To align the parabolic mirror and germanium lens to the highly sensitive detector, start by roughly matching the heights of both optics. Adjust the position of both optics until the signal on the LIA is maximized. Next, iteratively adjust the height of the germanium lens and sensitive, large-area MCT (or InSb) detector until a global maximum is reached. Once this is complete, remove the highly sensitive detector and replace with the high-speed MCT. Since the germanium lens and parabolic mirror are already aligned to each other, simply move the high speed MCT (and adjust its height via a compact lab jack) to maximize the signal. Finally, align the ns pulsed laser beam with the 980 nm laser beam using the IR card inside the chamber. Move the cryo such that the pulsed laser is incident on the calibration sample. Connect the output of the detector to the LeCroy oscilloscope. Set the input impedance of the scope to be 50 Ω. If the alignment was done properly, a transient decay curve should appear! If not, I would recommend moving only the pulsed laser (very carefully and slowly) or adjusting its height as oftentimes, the pulsed 1064 nm laser is not perfectly collinear with the 980 nm laser. In my experience, for the setup to be considered reasonably "aligned", for the bulk InAsSb calibration sample we typically use, the initial amplitude of the decay curve should exceed 10 mV when an ND2 filter is used to

reduce the laser power.

Troubleshooting:

1. No signal at all on the oscilloscope: Unfortunately, this system is extremely sensitive to alignment as the active area of the high-speed MCT is relatively small. Thus, oftentimes, a lack of signal is a result of poor alignment or bumped optics. However, prior to concluding this, first make sure the oscilloscope is triggered, and the laser is on and firing.

2. Laser is not firing: First, do all the obvious checks (laser plugged in, laser on, laser aperture open, etc). If using the software-controlled 1064 nm laser, check to make sure the laser is turned on in software. Occasionally, the software will display that the laser is on even when it is not; if this occurs, restart the software.

3. The 1064 nm laser seems to be "double firing": I have only intermittently experienced this issue a few times. Sometimes, turning the laser off and on (both software and hardware) will fix this issue. Otherwise, try reducing the current in the software from 3.0A to 2.7A.

4. Whenever the 532 nm laser is used, there seems to be a large noise signal within the first couple hundred nanoseconds on the scope: I do not recommend using the laser's internal photodiode as the trigger. This is because the trigger signal is rather large (typically on the order of volts), which can result in cross-talk between channels in the oscilloscope. Even though only a very small percentage seems to couple into the other channel, if the trigger signal is on the order of volts, cross-talk on the order of mV can be significant, especially when measuring weak signals. To fix this issue, I recommend splitting part of the laser beam and sending it to an InGaAs detector for use as the trigger signal instead of the laser's internal photodiode. Try to attenuate the signal (through the use of neutral density filters)

such that the signal from the InGaAs is as small as possible but can still function as a trigger.

A.3 Responsivity Measurements

Neutral Density Filter Calibration: The responsivity measurements are described in detail in Section 5.2. However, in Equation, 5.5, the tranmission of a neutral density (ND) filter is considered. Although the online specification for the ND filter can be used, in case the ND filter incurs damage or a fingerprint, it may be worthwhile to recalibrate it. Although doing so is just a straightforward transmission measurement in the FTIR, for most accurate results, use the smallest internal aperture that still yields a spectrum above the noise floor to prevent operating the internal MCT detector in a nonlinear regime. As a general rule of thumb for the Bruker FTIR systems in our lab, I find that when using rapid scan, the detector enters a nonlinear regime when the counts exceed 6000.

Appendix B

Fabrication Recipe Notes

In this Appendix, specific details on the fabrication processes will be described. Note that all fabrication in this dissertation (unless performed by collaborators or mentioned otherwise) was done in the Microelectronics Research Center at the University of Texas at Austin.

B.1 SRRs on Semi-Insulating Gallium Arsenide (SI GaAs)

1. First, clean the SI GaAs sample using acetone and isopropanol alcohol (IPA). Blow dry using nitrogen.

2. Deposit 10 nm of titanium (for adhesion) and 500 nm of gold to serve as the back ground plane.

3. Repeat step 1.

4. Remove the AZ-5214IR photoresist (PR) from the fridge. Spin the PR at 4000 rpm for 60 seconds.

5. Bake the sample on a hot plate set at 110 degrees Celsius for 60 seconds.

6. Expose pattern onto the sample. Using channel 1 on the MJB4, the sample is typically exposed for 12 seconds.

7. Develop for 45 seconds.

8. Use either an asher or RIE to oxygen descum the sample.

9. Deposit 10 nm of titanium and 500 nm on the patterned side of the sample.

10. Place sample in acetone for one hour at room temperature. The liftoff is generally very fast, although a cue tip can be used to gently aid the process.

B.2 SRRs on 99.6 % Aluminum Oxide

Fabrication of the SRRs on aluminum oxide used in Chapters 3 and 5 is nearly identity to the fabrication of the SI GaAs SRRs in Section B.1. However, the exposure and developing times were 8 seconds and 25 seconds, respectively.

B.3 PCB Resonators

The following was done to fabricate the PCB resonator in Figure 6.1:

1. Typically, the PCB we order is the Kappa 432 laminate with 1/2 ounce copper (approximately 17 μm in thickness) plated on both sides.

2. First, clean the SI GaAs sample using acetone and isopropanol alcohol (IPA). Blow dry using nitrogen.

3. Remove the AZ-5214IR photoresist (PR) from the fridge. Spin the PR at 4000 rpm for 60 seconds. This PR will serve as an etch mask/protection for the ground plane.

4. Flip the sample and repeat Step 3.

5. Bake the sample on a hot plate set at 110 degrees Celsius for 60 seconds.

6. Expose pattern onto the sample. A 15 second exposure time was used when the MJB4 power is set to channel 1.

7. Develop for 45 seconds.

8. Mix an etch bath of hydrocholic acid (HCl) and hydrogen peroxide (H_2O_2). The solution used consists of 200 mL of deionized water, 100 mL of HCl (37%), and 40 mL of H_2O_2 (30 %).

9. Dip the patterned samples into the etch bath. The 17 μm thick copper should etch within a few minutes. Typically, the solution will turn bright green during the etch.

B.4 Epsilon-Near-Zero (ENZ) Ultra-Thin Microstrips

Here, the partial fabrication of the ENZ ultra-thin microstrips introduced in Chapter 6 is covered. Note that since this is ongoing work at the time of writing this dissertation, fabrication steps not yet completed are not mentioned here.

1. Ask an MBE grower really nicely to grow the sample. If they are apprehensive about growing the structure, tell them it is very easy, and that the idea is definitely going to work. The ENZ sample here was grown by Leland Nordin.

2. Cleave the sample into small, 1 cm $\times$ 1 cm pieces. Obtain (or dice) a slightly larger piece of silicon (1.3 cm $\times$ 1.3 cm).

3. Deposit 10 nm of titanium (adhesion) and 250 nm of gold on the sample piece (ensure that the deposition occurs on the front side, or on the epitaxially grown layer) and a silicon handle piece.

4. Using the AML wafer bonder in the cleanroom, bond the sample to the handle

wafer (Au-Au bonding). Make sure the gold surfaces of both the sample and handle piece are cleaned prior to bonding. The pieces are bonded at 400 degrees Celsius. The pieces are pressed together for 20 minutes using approximately 300 Newtons of force.

5. Lap the GaAs substrate using 600 grit lapping paper. Personally, I recommend lapping by hand as the lapping machine tends to result in significant "coning", where the center of the sample is thicker than the edges.

6. Mix anhydrous citric acid powder with water (1:1 ratio). Use a magnetic stir bar to thoroughly mix for at least 15 minutes. Add H_2O_2 such that the ratio of citric acid to H_2O_2 is 5:1.

7. Add the sample to the etch bath. Once the GaAs substrate is removed and the aluminum containing etch stop layer is reached, the surface of the sample will become shiny and rainbow interference patterns will be observed.

Appendix C

List of Publications and Conference Talks

The following are a list of my authored and co-authored publications at the time of submitting this dissertation.

C.1 Journal Publications

1. "Room temperature mid-infrared detection via resonant microwave circuits", **S. Dev**, Y. Wang, Y. Wang, M. Allen, J. Allen, E. Tutuc, and D. Wasserman, *under review*.

2. "Design and growth of multi-functional InAsP metamorphic buffers for mid-infrared quantum well lasers on InP", D. Jung, L. Yu, **S. Dev**, D. Wasserman, and M. L. Lee, *Journal of Applied Physics Special Issue on Strain Engineering in Functional Materials*, 125, 8, (2019).

3. "Measurement of carrier lifetime in micron-scaled materials using resonant microwave circuits", **S. Dev**, Y. Wang, K. Kim, M. Zamiri, C. Kadlec, M. Goldflam, E. Shaner, J. Kim, S. Hawkins, J. Allen, M. Allen, S. Krishna, E. Tutuc, and D. Wasserman, *Nature Communications*, 10, 1625, (2019).

4. "Optical Mapping of RF Field Profiles in Resonant Microwave Circuits", **S. Dev**, R. Liu, J. W. Allen, M. S. Allen, B. R. Wenner, and D. Wasserman, *IEEE Photon. Technol. Lett.*, 30, 331 (2018).

5. "Engineering carrier lifetimes in type-II In(Ga)Sb/InAs mid-IR emitters", L. Yu, Y. Zhong, **S. Dev**, and D. Wasserman, *Journal of Vacuum Science and Technology B*, 35, 02B101 (2017).

6. "Enhanced responsivity resonant RF photodetectors", R. Liu, **S. Dev**, Y. Zhong, R. Lu, W. Streyer, J. W. Allen, M. S. Allen, B.R. Wenner, S. Gong, and D. Wasserman, *Optics Express*, 24(23), 26044-26054 (2016).

7. "Room-temperature mid-infrared quantum well lasers on multi-functional metamorphic buffers", D. Jung, L. Yu, **S. Dev**, D. Wasserman, and M.L. Lee, *Applied Physics Letters*, 109, 211101 (2016).

C.2 Conference Presentations and Publications

1. "Mid-infrared detection using a microwave resonator photoconductive architecture", **S. Dev**, Y. Wang, Y. Wang, M. Allen, J. Allen, E. Tutuc, and D. Wasserman, *IEEE RAPID Optical Emitters and Detectors* (August, 2019).

2. "RF read-out of minority carrier lifetime in micro-scaled infrared materials", **S. Dev**, Y. Wang, K. Kim, M. Zamiri, C. Kadlec, M. Goldflam, E. Shaner, J. Kim, S. Hawkins, J. Allen, M. Allen, S. Krishna, E. Tutuc, and D. Wasserman, *CLEO* (May, 2019).

3. "Electrical readout of carrier dynamics in micro-scale infrared materials", **S. Dev**, Y. Wang, K. Kim, M. Zamiri, E. Shaner, J. Kim, S. Hawkins, J. Allen, M. Allen, S. Krishna, E. Tutuc, and D. Wasserman, *RAPID Optical Emitters and Detectors* (August, 2018).

4. "Extending the Operating Wavelength of Type-I InAs Quantum Well Lasers on

InP", M. L. Lee, D. Jung, L. Yu, **S. Dev**, and D. Wasserman, *Novel Optical Materials and Applications*, NoW3C. 4 (July, 2017).

5. "New sources and sensors for mid-to far-IR optical sensing", L. Yu, D. Jung, **S. Dev**, N. Yoon, L. Nordin, A. Hoffman, M. L. Lee, and D. Wasserman, *CLEO* (May, 2017).

6. "Resonant RF Photodetectors for Microwave and Infrared Applications", J. Allen, M. Allen, B. Wenner, R. Liu, **S. Dev**, and D. Wasserman, *APS March Meeting Abstracts* (March, 2017).

7. "Gallium-doped zinc oxide plasmonic nanostructures for mid-IR applications", **S. U. Dev**, D. C. Look, K. D. Leedy, L. Yu, D. E. Walker Jr., B. R. Wenner, J. W. Allen, M. S. Allen, and D. Wasserman, *SPIE Optics and Photonics* (August, 2016).

8. "Mid-IR Lasers and LEDs Using Type I and II Materials", L. Yu, D. Jung, R. Liu, **S. Dev**, Y. Zhong, M. Lee, and D. Wasserman, *CLEO* (June, 2016).

Bibliography

[1] I. Coddington, N. Newbury, and W. Swann, "Dual-comb spectroscopy," *Optica*, vol. 3, no. 4, pp. 414–426, 2016.

[2] J. Hodgkinson and R. P. Tatam, "Optical gas sensing: a review," *Measurement Science and Technology*, vol. 24, no. 1, p. 012004, 2012.

[3] F. Ciampa, P. Mahmoodi, F. Pinto, and M. Meo, "Recent advances in active infrared thermography for non-destructive testing of aerospace components," *Sensors*, vol. 18, no. 2, p. 609, 2018.

[4] N. K. Dhar, R. Dat, and A. K. Sood, "Advances in infrared detector array technology," *Optoelectronics-Advanced Materials and Devices*, vol. 7, pp. 149–188, 2013.

[5] V. W. Chan, "Free-space optical communications," *Journal of Lightwave technology*, vol. 24, no. 12, pp. 4750–4762, 2006.

[6] A. Rogalski, *Infrared detectors*. CRC press, 2010.

[7] S. Maimon and G. Wicks, "n b n detector, an infrared detector with reduced dark current and higher operating temperature," *Applied Physics Letters*, vol. 89, no. 15, p. 151109, 2006.

[8] D. M. Pozar, *Microwave Engineering*. John Wiley & Sons, 2008.

[9] A. Vladimirescu, *The SPICE book*. Wiley New York, 1994.

[10] T. Wei, X.-D. Xiang, W. Wallace-Freedman, and P. Schultz, "Scanning tip microwave near-field microscope," *Applied Physics Letters*, vol. 68, no. 24, pp. 3506–3508, 1996.

[11] K. Yang, G. David, J.-G. Yook, I. Papapolymerou, L. P. Katehi, and J. F. Whitaker, "Electrooptic mapping and finite-element modeling of the near-field pattern of a microstrip patch antenna," *IEEE Transactions on Microwave Theory and Techniques*, vol. 48, no. 2, pp. 288–294, 2000.

[12] S. Dev, R. Liu, J. W. Allen, M. S. Allen, B. R. Wenner, and D. Wasserman, "Optical mapping of rf field profiles in resonant microwave circuits," *IEEE Photonics Technology Letters*, vol. 30, no. 4, pp. 331–334, 2017.

[13] D. Palaferri, Y. Todorov, A. Bigioli, A. Mottaghizadeh, D. Gacemi, A. Calabrese, A. Vasanelli, L. Li, A. G. Davies, E. H. Linfield *et al.*, "Room-temperature nine-μm-wavelength photodetectors and ghz-frequency heterodyne receivers," *Nature*, vol. 556, no. 7699, p. 85, 2018.

[14] H. Sommers and W. Teutsch, "Demodulation of low-level broad-band optical signals with semiconductors: Part iiâĂŤanalysis of the photoconductive detector," *Proceedings of the IEEE*, vol. 52, no. 2, pp. 144–153, 1964.

[15] R. Boyd, *Nonlinear Optics*. Elsevier, 2003.

[16] G. P. Agrawal, *Fiber Optic Communication Systems*. John Wiley & Sons, 2012.

[17] P. Del'Haye, A. Schliesser, O. Arcizet, T. Wilken, R. Holzwarth, and T. J. Kippenberg, "Optical frequency comb generation from a monolithic microresonator," *Nature*, vol. 450, no. 7173, p. 1214, 2007.

[18] B. Stern, X. Ji, Y. Okawachi, A. L. Gaeta, and M. Lipson, "Battery-operated integrated frequency comb generator," *Nature*, vol. 562, no. 7727, p. 401, 2018.

[19] Z. Zhang, T. Gardiner, and D. T. Reid, "Mid-infrared dual-comb spectroscopy with an optical parametric oscillator," *Optics letters*, vol. 38, no. 16, pp. 3148–3150, 2013.

[20] A. Schliesser, N. Picqué, and T. W. Hänsch, "Mid-infrared frequency combs," *Nature photonics*, vol. 6, no. 7, p. 440, 2012.

[21] B. Bernhardt, E. Sorokin, P. Jacquet, R. Thon, T. Becker, I. T. Sorokina, N. Picqué, and T. W. Hänsch, "Mid-infrared dual-comb spectroscopy with 2.4 μm cr 2+: Znse femtosecond lasers," *Applied Physics B*, vol. 100, no. 1, pp. 3–8, 2010.

[22] M. Yu, Y. Okawachi, A. G. Griffith, N. Picqué, M. Lipson, and A. L. Gaeta, "Silicon-chip-based mid-infrared dual-comb spectroscopy," *Nature communications*, vol. 9, no. 1, p. 1869, 2018.

[23] P. Laj, J. Klausen, M. Bilde, C. Plass-Duelmer, G. Pappalardo, C. Clerbaux, U. Baltensperger, J. Hjorth, D. Simpson, S. Reimann *et al.*, "Measuring atmospheric composition change," *Atmospheric environment*, vol. 43, no. 33, pp. 5351–5414, 2009.

[24] D. Smith and P. Španěl, "The challenge of breath analysis for clinical diagnosis and therapeutic monitoring," *Analyst*, vol. 132, no. 5, pp. 390–396, 2007.

[25] M. G. Allen, "Diode laser absorption sensors for gas-dynamic and combustion flows," *Measurement Science and technology*, vol. 9, no. 4, p. 545, 1998.

[26] J. Faist, F. Capasso, D. L. Sivco, C. Sirtori, A. L. Hutchinson, and A. Y. Cho, "Quantum cascade laser," *Science*, vol. 264, no. 5158, pp. 553–556, 1994.

[27] M. Sieger, G. Kos, M. Sulyok, M. Godejohann, R. Krska, and B. Mizaikoff, "Portable infrared laser spectroscopy for on-site mycotoxin analysis," *Scientific reports*, vol. 7, p. 44028, 2017.

[28] A. M. Waxman, A. N. Gove, D. A. Fay, J. P. Racamato, J. E. Carrick, M. C. Seibert, and E. D. Savoye, "Color night vision: opponent processing in the fusion of visible and ir imagery," *Neural Networks*, vol. 10, no. 1, pp. 1–6, 1997.

[29] O. Tsimhoni, J. Bärgman, and M. J. Flannagan, "Pedestrian detection with near and far infrared night vision enhancement," *Leukos*, vol. 4, no. 2, pp. 113–128, 2007.

[30] A. M. Waxman, D. A. Fay, A. N. Gove, M. Seibert, J. P. Racamato, J. E. Carrick, and E. D. Savoye, "Color night vision: fusion of intensified visible and thermal ir imagery," in *Synthetic Vision for Vehicle Guidance and Control*, vol. 2463. International Society for Optics and Photonics, 1995, pp. 58–68.

[31] H. Wiggenhauser, "Active ir-applications in civil engineering," *Infrared Physics & Technology*, vol. 43, no. 3-5, pp. 233–238, 2002.

[32] S. Huth, O. Breitenstein, A. Huber, D. Dantz, U. Lambert, and F. Altmann, "Lock-in ir-thermography-a novel tool for material and device characterization," in *Diffusion And Defect Data Part B Solid State Phenomena*. Citeseer, 2002, pp. 741–746.

[33] M. Omar, M. Hassan, K. Saito, and R. Alloo, "Ir self-referencing thermography for detection of in-depth defects," *Infrared physics & technology*, vol. 46, no. 4, pp. 283–289, 2005.

[34] R. Martini, C. Bethea, F. Capasso, C. Gmachl, R. Paiella, E. Whittaker, H. Hwang, D. Sivco, J. Baillargeon, and A. Cho, "Free-space optical transmission of multimedia satellite data streams using mid-infrared quantum cascade lasers," *Electronics Letters*, vol. 38, no. 4, pp. 181–183, 2002.

[35] V. W. Chan, "Optical satellite networks," *Journal of Lightwave Technology*, vol. 21, no. 11, p. 2811, 2003.

[36] E. L. Dereniak and G. D. Boreman, *Infrared detectors and systems*. Wiley New York, 1996, vol. 306.

[37] P. Richards, "Bolometers for infrared and millimeter waves," *Journal of Applied Physics*, vol. 76, no. 1, pp. 1–24, 1994.

[38] F. Niklaus, C. Vieider, and H. Jakobsen, "Mems-based uncooled infrared bolometer arrays: a review," in *MEMS/MOEMS technologies and applications III*, vol. 6836. International Society for Optics and Photonics, 2008, p. 68360D.

[39] S. Liu and D. Long, "Pyroelectric detectors and materials," *Proceedings of the IEEE*, vol. 66, no. 1, pp. 14–26, 1978.

[40] A. Graf, M. Arndt, M. Sauer, and G. Gerlach, "Review of micromachined thermopiles for infrared detection," *Measurement Science and Technology*, vol. 18, no. 7, p. R59, 2007.

[41] M. Reine, A. Sood, and T. Tredwell, "Photovoltaic infrared detectors," in *Semiconductors and semimetals*. Elsevier, 1981, vol. 18, pp. 201–311.

[42] A. Rogalski, "Heterostructure infrared photovoltaic detectors," *Infrared Physics & Technology*, vol. 41, no. 4, pp. 213–238, 2000.

[43] B. G. Streetman and S. Banerjee, *Solid state electronic devices*. Prentice-Hall of India, 2001.

[44] I. Kimukin, N. Biyikli, and E. Ozbay, "Insb high-speed photodetectors grown on gaas substrate," *Journal of applied physics*, vol. 94, no. 8, pp. 5414–5416, 2003.

[45] A. M. Itsuno, J. D. Phillips, and S. Velicu, "Mid-wave infrared hgcdte nbn photodetector," *Applied physics letters*, vol. 100, no. 16, p. 161102, 2012.

[46] H. Kim, O. Cellek, Z.-Y. Lin, Z.-Y. He, X.-H. Zhao, S. Liu, H. Li, and Y.-H. Zhang, "Long-wave infrared nbn photodetectors based on inas/inassb type-ii superlattices," *Applied Physics Letters*, vol. 101, no. 16, p. 161114, 2012.

[47] B. C. Wadell, *Transmission Line Design Handbook*. Artech House, 1991.

[48] H. U. Manual, "Ansoft corp," *Pittsburgh, PA, USA*, 2005.

[49] J.-M. Jin, *The finite element method in electromagnetics*. John Wiley & Sons, 2015.

[50] J. N. Reddy, "An introduction to the finite element method," *New York*, 1993.

[51] O. C. Zienkiewicz, R. L. Taylor, P. Nithiarasu, and J. Zhu, *The finite element method*. McGraw-hill London, 1977, vol. 3.

[52] G. Strang and G. J. Fix, *An analysis of the finite element method*. Prentice-hall Englewood Cliffs, NJ, 1973, vol. 212.

[53] C. Berthomieu and R. Hienerwadel, "Fourier transform infrared (ftir) spectroscopy," *Photosynthesis research*, vol. 101, no. 2-3, pp. 157–170, 2009.

[54] W. Herres and J. Gronholz, "Understanding ft-ir data processing," *Part*, vol. 1, pp. 352–356, 1984.

[55] M. Fee, S. Chu, and T. Hänsch, "Scanning electromagnetic transmission line microscope with sub-wavelength resolution," *Optics Communications*, vol. 69, no. 3-4, pp. 219–224, 1989.

[56] E. Ash and G. Nicholls, "Super-resolution aperture scanning microscope," *Nature*, vol. 237, no. 5357, p. 510, 1972.

[57] C. Bryant and J. Gunn, "Noncontact technique for the local measurement of semiconductor resistivity," *Review of Scientific Instruments*, vol. 36, no. 11, pp. 1614–1617, 1965.

[58] S. Dutta, C. Vlahacos, D. Steinhauer, A. S. Thanawalla, B. Feenstra, F. Wellstood, S. M. Anlage, and H. S. Newman, "Imaging microwave electric fields using a near-field scanning microwave microscope," *Applied physics letters*, vol. 74, no. 1, pp. 156–158, 1999.

[59] V. V. Talanov, C. D. Barga, L. Wickey, I. Kalichava, E. Gonzales, E. A. Shaner, A. V. Gin, and N. G. Kalugin, "Few-layer graphene characterization by near-field scanning microwave microscopy," *ACS nano*, vol. 4, no. 7, pp. 3831–3838, 2010.

[60] F. Martın, J. Bonache, F. a. Falcone, M. Sorolla, and R. Marqués, "Split ring resonator-based left-handed coplanar waveguide," *Applied Physics Letters*, vol. 83, no. 22, pp. 4652–4654, 2003.

[61] C.-C. Yu and K. Chang, "Transmission-line analysis of a capacitively coupled microstrip-ring resonator," *IEEE Transactions on Microwave Theory and Techniques*, vol. 45, no. 11, pp. 2018–2024, 1997.

[62] P. K. Day, H. G. LeDuc, B. A. Mazin, A. Vayonakis, and J. Zmuidzinas, "A broadband superconducting detector suitable for use in large arrays," *Nature*, vol. 425, no. 6960, p. 817, 2003.

[63] R. Liu, S. Dev, Y. Zhong, R. Lu, W. Streyer, J. Allen, M. Allen, B. Wenner, S. Gong, and D. Wasserman, "Enhanced responsivity resonant rf photodetectors," *Optics express*, vol. 24, no. 23, pp. 26 044–26 054, 2016.

[64] Y. Wang, "Photoconductivity of fullerene-doped polymers," *Nature*, vol. 356, no. 6370, p. 585, 1992.

[65] J. Bechtel and W. L. Smith, "Two-photon absorption in semiconductors with picosecond laser pulses," *Physical Review B*, vol. 13, no. 8, p. 3515, 1976.

[66] S. Dev, Y. Wang, K. Kim, M. Zamiri, C. Kadlec, M. Goldflam, S. Hawkins, E. Shaner, J. Kim, S. Krishna *et al.*, "Measurement of carrier lifetime in micron-scaled materials using resonant microwave circuits," *Nature communications*, vol. 10, no. 1, p. 1625, 2019.

[67] S. L. Chuang, *Physics of photonic devices*. John Wiley & Sons, 2012, vol. 80.

[68] D. T. Stevenson and R. J. Keyes, "Measurement of carrier lifetimes in germanium and silicon," *Journal of Applied Physics*, vol. 26, no. 2, pp. 190–195, 1955.

[69] D. Navon, R. Bray, and H. Fan, "Lifetime of injected carriers in germanium," *Proceedings of the IRE*, vol. 40, no. 11, pp. 1342–1347, 1952.

[70] B. C. Connelly, G. D. Metcalfe, H. Shen, and M. Wraback, "Direct minority carrier lifetime measurements and recombination mechanisms in long-wave infrared type ii superlattices using time-resolved photoluminescence," *Applied physics letters*, vol. 97, no. 25, p. 251117, 2010.

[71] A. Ramsa, H. Jacobs, and F. Brand, "Microwave techniques in measurement of lifetime in germanium," *Journal of Applied Physics*, vol. 30, no. 7, pp. 1054–1060, 1959.

[72] S. Deb and B. Nag, "Measurement of lifetime of carriers in semiconductors through microwave reflection," *Journal of Applied physics*, vol. 33, no. 4, pp. 1604–1604, 1962.

[73] V. Nicolosi, M. Chhowalla, M. G. Kanatzidis, M. S. Strano, and J. N. Coleman, "Liquid exfoliation of layered materials," *Science*, vol. 340, no. 6139, p. 1226419, 2013.

[74] H. Shao, W. Li, A. Torfi, D. Moscicka, and W. Wang, "Room-temperature inassb photovoltaic detectors for mid-infrared applications," *IEEE photonics technology letters*, vol. 18, no. 16, pp. 1756–1758, 2006.

[75] Y. Sharabani, Y. Paltiel, A. Sher, A. Raizman, and A. Zussman, "In as sb/ ga sb heterostructure based mid-wavelength-infrared detector for high temperature operation," *Applied physics letters*, vol. 90, no. 23, p. 232106, 2007.

[76] I. Shafir, M. Katz, A. Sher, A. Raizman, A. Zussman, and M. Nathan, "Suppression of leakage currents in inassb mwir photodiodes by chemical treatment and illumination," *Semiconductor Science and Technology*, vol. 25, no. 4, p. 045004, 2010.

[77] B. Olson, E. Shaner, J. Kim, J. Klem, S. Hawkins, L. Murray, J. Prineas, M. Flatté, and T. Boggess, "Time-resolved optical measurements of minority carrier recombination in a mid-wave infrared inassb alloy and inas/inassb superlattice," *Applied Physics Letters*, vol. 101, no. 9, p. 092109, 2012.

[78] D. Schroder, T. Braggins, and H. Hobgood, "The doping concentrations of indium-doped silicon measured by hall, c-v, and junction-breakdown techniques," *Journal of Applied Physics*, vol. 49, no. 10, pp. 5256–5259, 1978.

[79] M. Zamiri, B. Klein, T. Schuler-Sandy, S. Myers, V. Dahiya, F. Cavallo, and S. Krishna, "Indium-bump-free antimonide superlattice membrane detectors on silicon substrates," *Applied Physics Letters*, vol. 108, no. 9, p. 091110, 2016.

[80] B. Olson, C. Grein, J. Kim, E. Kadlec, J. Klem, S. Hawkins, and E. Shaner, "Auger recombination in long-wave infrared inas/inassb type-ii superlattices," *Applied Physics Letters*, vol. 107, no. 26, p. 261104, 2015.

[81] D. Jung, S. Bank, M. L. Lee, and D. Wasserman, "Next-generation mid-infrared sources," *Journal of Optics*, vol. 19, no. 12, p. 123001, 2017.

[82] J. Jimenez, P. Hernandez, J. De Saja, and J. Bonnafe, "Optically induced long-lifetime photoconductivity in semi-insulating bulk gaas," *Physical Review B*, vol. 35, no. 8, p. 3832, 1987.

[83] K. Kim, M. Yankowitz, B. Fallahazad, S. Kang, H. C. Movva, S. Huang, S. Larentis, C. M. Corbet, T. Taniguchi, K. Watanabe *et al.*, "van der waals heterostructures with high accuracy rotational alignment," *Nano letters*, vol. 16, no. 3, pp. 1989–1995, 2016.

[84] B. V. Olson, E. A. Kadlec, J. K. Kim, J. F. Klem, S. D. Hawkins, E. A. Shaner, and M. E. Flatte, "Intensity-and temperature-dependent carrier recombination in inas/in as 1- x s b x type-ii superlattices," *Physical Review Applied*, vol. 3, no. 4, p. 044010, 2015.

[85] B. Olson, E. Shaner, J. Kim, J. Klem, S. Hawkins, M. Flatté, and T. Boggess, "Identification of dominant recombination mechanisms in narrow-bandgap inas/inassb type-ii superlattices and inassb alloys," *Applied Physics Letters*, vol. 103, no. 5, p. 052106, 2013.

[86] L. Höglund, D. Ting, A. Khoshakhlagh, A. Soibel, C. Hill, A. Fisher, S. Keo, and S. Gunapala, "Influence of radiative and non-radiative recombination on the minority carrier lifetime in midwave infrared inas/inassb superlattices," *Applied Physics Letters*, vol. 103, no. 22, p. 221908, 2013.

[87] M. Zarifi, A. Mohammadpour, S. Farsinezhad, B. Wiltshire, M. Nosrati, A. Askar, M. Daneshmand, and K. Shankar, "Time-resolved microwave photoconductivity

(trmc) using planar microwave resonators: Application to the study of long-lived charge pairs in photoexcited titania nanotube arrays," *The Journal of Physical Chemistry C*, vol. 119, no. 25, pp. 14 358–14 365, 2015.

[88] J. Krupka, "Frequency domain complex permittivity measurements at microwave frequencies," *Measurement Science and Technology*, vol. 17, no. 6, p. R55, 2006.

[89] S. Trabelsi, A. Kraszewski, and S. Nelson, "Determining physical properties of grain by microwave permittivity measurements," *Transactions of the ASAE*, vol. 42, no. 2, p. 531, 1999.

[90] S. Nelson, W. Forbus, K. Lawrence *et al.*, "Assessment of microwave permittivity for sensing peach maturity," *Transactions of the ASAE*, vol. 38, no. 2, pp. 579–585, 1995.

[91] A. A. Abduljabar, D. J. Rowe, A. Porch, and D. A. Barrow, "Novel microwave microfluidic sensor using a microstrip split-ring resonator," *IEEE Transactions on Microwave Theory and Techniques*, vol. 62, no. 3, pp. 679–688, 2014.

[92] H. Choi, J. Naylon, S. Luzio, J. Beutler, J. Birchall, C. Martin, and A. Porch, "Design and in vitro interference test of microwave noninvasive blood glucose monitoring sensor," *IEEE transactions on microwave theory and techniques*, vol. 63, no. 10, pp. 3016–3025, 2015.

[93] Y. Dan, X. Zhao, K. Chen, and A. Mesli, "A photoconductor intrinsically has no gain," *ACS Photonics*, vol. 5, no. 10, pp. 4111–4116, 2018.

[94] W. Fawcett and J. Ruch, "Negative differential mobility in indium antimonide," *Applied Physics Letters*, vol. 15, no. 11, pp. 368–370, 1969.

[95] J. Nelson, "Breakdown strength of solids," in *Engineering Dielectrics Volume IIA Electrical Properties of Solid Insulating Materials: Molecular Structure and Electrical Behavior*. ASTM International, 1983.

[96] F. Hooge, "1/f noise sources," *IEEE Transactions on electron devices*, vol. 41, no. 11, pp. 1926–1935, 1994.

[97] F. Hooge, T. Kleinpenning, and L. Vandamme, "Experimental studies on 1/f noise," *Reports on progress in Physics*, vol. 44, no. 5, p. 479, 1981.

[98] K. Van Vliet, "Noise in semiconductors and photoconductors," *Proceedings of the IRE*, vol. 46, no. 6, pp. 1004–1018, 1958.

[99] A. van der Ziel, *Fluctuation Phenomena in Semiconductors*. London Butterworths Scientific Publications, 1959.

[100] J. B. Johnson, "Thermal agitation of electricity in conductors," *Physical review*, vol. 32, no. 1, p. 97, 1928.

[101] H. Nyquist, "Thermal agitation of electric charge in conductors," *Physical review*, vol. 32, no. 1, p. 110, 1928.

[102] M. Zimmermann and K. Dostert, "Analysis and modeling of impulsive noise in broadband powerline communications," *IEEE transactions on Electromagnetic compatibility*, vol. 44, no. 1, pp. 249–258, 2002.

[103] F. Pascal, S. Jarrix, C. Delseny, G. Lecoy, and T. Kleinpenning, "Generation-recombination noise analysis in heavily doped p-type gaas transmission line models," *Journal of applied physics*, vol. 79, no. 6, pp. 3046–3052, 1996.

[104] L. K. Vandamme, "Bulk and surface 1/f noise," *IEEE Transactions on Electron Devices*, vol. 36, no. 5, pp. 987–992, 1989.

[105] J. C. Pearson, K. Cooper, and B. J. Drouin, "Spectroscopic detection, fundamental limits and system considerations," in *2008 33rd International Conference on Infrared, Millimeter and Terahertz Waves*. IEEE, 2008, pp. 1–2.

[106] C. Townes and S. Geschwind, "Limiting sensitivity of a microwave spectrometer," *Journal of Applied Physics*, vol. 19, no. 8, pp. 795–796, 1948.

[107] Y. Wei, A. Hood, H. Yau, A. Gin, M. Razeghi, M. Z. Tidrow, and V. Nathan, "Uncooled operation of type-ii inas/ gasb superlattice photodiodes in the midwavelength infrared range," *Applied Physics Letters*, vol. 86, no. 23, p. 233106, 2005.

[108] G. Bishop, E. Plis, J. Rodriguez, Y. Sharma, H. Kim, L. Dawson, and S. Krishna, "nbn detectors based on in as/ ga sb type-ii strain layer superlattice," *Journal of Vacuum Science & Technology B: Microelectronics and Nanometer Structures Processing, Measurement, and Phenomena*, vol. 26, no. 3, pp. 1145–1148, 2008.